Exp 623

DOE/ER/40085-8

OBSERVATION OF THE CABIBBO-SUPPRESSED DECAY $D^{\pm} \rightarrow \phi\pi^{\pm}$

A THESIS

Submitted by

CHRISTOS H. GEORGIOPOULOS

In partial fulfillment of the requirements

for the degree of

DOCTOR OF PHILOSOPHY

TUFTS UNIVERSITY

MAY, 1985

FERMI
QC10F
.G298

TABLE OF CONTENTS

ABSTRACT

ACKNOWLEDGEMENTS

CHAPTER 1 INTRODUCTION

CHAPTER 2 APPARATUS DESCRIPTION

2.1 The Beam

2.2 The Target

2.3 The Magnet

2.4 MWPC System

2.5 Drift Chambers

2.6 Cherenkov Counters

2.7 The Scintillator Hodoscope

2.8 Cross Section and Sensitivity

2.9 On-Line Analysis

CHAPTER 3 DATA SELECTION

3.1 Physical Description

3.2 Track Recognition Logic

3.3 High Level Logic

3.4 Gating the Processor

3.5 Trigger Formation

3.6 K^+K^- Mass Measurement Using the Processor

3.7 Off-Line Analysis

CHAPTER 4 PARTICLE IDENTIFICATION

4.1 Apparatus Description

4.2 Cherenkov Algorithm

4.3 Distribution of the number of photons in a Cherenkov cone

CHAPTER 5 PRODUCTION AND DECAY OF CHARM

5.1 The Need for Charm.

5.2 The GIM Solution - The Charm Quark

5.3 The Observation of Charm and its Decay

5.4 Expected Properties of Open Charm Decay

5.5 Hadronic Production of Charm

CHAPTER 6 STUDY OF THE $\phi\pi^{\pm}$ FINAL STATE

6.1 Data Selection

6.2 Observation of the Cabibbo-Suppressed decay $D^{\pm} \rightarrow \phi\pi^{\pm}$

6.3 Cross Section Estimates

6.4 Summary

APPENDIX A ANGULAR DISTRIBUTIONS OF BOSON RESONANCES

APPENDIX B MONTE CARLO DEVELOPMENT FOR E-623

FERMILAB LIBRARY

ABSTRACT

We report results from the Fermilab MPS experiment E-623. The experiment was a particle search for high mass resonances from proton-nucleon interactions at 400 GeV/c incident proton momentum. The reaction was $pN \rightarrow K^+K^-K^+K^-X$, where X contains up to 6 charged particles. We used a trigger processor to select events with at least two pairs of oppositely charged kaons with an effective mass near that of the ϕ meson. The design of the experiment was such as to be sensitive in the kinematic region $|x_F| < 0.1$.

We observed the Cabibbo-suppressed decay of the $D^{\pm} \rightarrow \phi\pi^{\pm}$ but not the Cabibbo-allowed decay $F^{\pm} \rightarrow \phi\pi^{\pm}$. The mass and width of the D are 1.8654 ± 0.0087 Gev/c^2 and 0.053 ± 0.018 GeV/c^2 respectively. The width is consistent with our experimental resolution. We set an upper limit on the inclusive hadronic production of the $F^{\pm}$ of 13.0 ± 9.0 μb subject to considerable uncertainty due to extrapolations based on a specific model.

ACKNOWLEDGMENTS

I would like to thank the E-580/623 collaboration for giving me the chance to participate in this experiment, and especially I would like to thank Dr. Dan Green, Dr. Harvey Goldman, Dr. John Ficenec, and Dr. John Marraffino for their help and guidance. I would also like to thank my fellow graduate students Forest Davenport, Sergio Torres, and Jim Woosley, for their hard work through these years. Without them this work would not have been possible.

I would like to express my deepest admiration and respect to my advisor Professor Austin Napier, for making all this happen. Without his great guidance and patience, I would have never finished this work. I would like to thank him for always being there to support me, and for his understanding and encouragement through the difficult times when nothing seemed to work. It has been a great pleasure to know him and I will always be indebted to him.

Finally, I would like to thank my family for their encouragement, understanding, and support through all these years. As a small token of my deepest appreciation, I dedicate this work to them.

CHAPTER 1

INTRODUCTION

In this thesis results are reported from a study of the final state $\phi\pi^{\pm}$ in the reaction :

$$pN \rightarrow K^+K^-K^+K^-X$$

at 400 Gev/c incident proton momentum, where X includes up to 6 charged particles.

The data were taken in May and June of 1982 using the Fermilab Multiparticle Spectrometer (FMPS) setup in the M6W beam line at Fermilab by the E580/623 collaboration.* The study of this reaction was a part of an experiment whose main emphasis was the study of the $\phi\phi$ final state. The experiment used a high-speed trigger processor seeking events with at least two pairs of oppositely charged particles having an effective mass compatible with the ϕ mass. In a period of 24 days we obtained 3.65×10^6 triggers, which after pattern recognition and kinematic fitting were reduced to 120,000 events with at least $2K^+$ and $2K^-$. The main reason for choosing the reaction $pN \rightarrow K^+K^-K^+K^-X$ is that inclusive production of a strange-charm-anticharm-antistrange state

* In this collaboration presently the following institutions participate:

(1) University of Arizona.

(2) Fermilab.

(3) Florida State University.

(4) University of Notre Dame.

(5) Tufts University.

(6) Vanderbilt University.

(7) Virginia Tech.

(e.g. a state contaning a D meson, a F meson, and a K) will produce 4 kaons: one spectator, one from the D and two from the F. The design of the experiment was such as to be sensitive in the kinematic region $|x_F| < 0.1$.

Chapter 2 describes the experimental apparatus. Chapter 3 contains the the on-line and off-line techniques for event selection while Chapter 4 is concerned with particle identification. Chapter 5 deals with the theoretical and experimental production and decay of charm and Chapter 6 with the study of the $\phi\pi^{\pm}$ final state.

CHAPTER 2

DESCRIPTION OF THE APPARATUS

We used the Fermilab Multiparticle Spectrometer (FMPS) which is located in the M6W beam of the Meson area at Fermilab and is shown in Figures 2.1 and 2.2.

It includes the following elements:

(a) Three multiwire proportional chamber stations (BA1,BA2,BB) for measuring the trajectory of the incoming beam (upstream-not shown).

(b) A target consisting of planes of active scintillator followed by a scintillation counter (dE/dx) to measure particle multiplicities and by two proportional wire stations (A and B) for vertex determination.

(c) A superconducting magnet with a P_T kick of 0.697 GeV/c in the x-z plane, inside which a MWPC station and a multicell Cherenkov counter (CA) reside.

(d) After the magnet we have another MWPC station (D) followed by a another Cherenkov counter (CB), two drift chamber stations (DA and DB), a hodoscope of scintillation counters (SCIWALL) and a final MWPC station (F).

(e) A trigger processor utilizing elements from station C,D,DB,CA,CB,and SCIWALL. A detailed description of these follows with special emphasis on the trigger processor (chapter 3) and particle identification (chapter 4).

2.1 The Beam

The FMPS setup is in the M6W beam line of the meson area at Fermilab. The beam delivered is either a proton beam of 400 GeV/c or a π^- beam of 250 GeV/c. We used a 400 GeV/c incident momentum unpolarized proton beam with a momentum resolution of 0.5%. The contamination of the beam is for all

purposes negligible at this momentum. The beam dimensions were 1.0 and 0.5 cm in x and y respectively, with an angle of incidence about 2.5 mrad. We received an effective beam of 8.7×10^{10} protons. We define the effective beam to be the total beam times the live time.

2.2 The Target

The beam impinges on a target, which is an " active " target. It is composed of 20 segments of plastic scintillator (CH_2) wrapped in aluminum foil and paper. The role of the active target was to record changes in charged particle multiplicities, and thus enable us to identify secondary interactions. However, this information is not used in the analysis that follows. The reason is the difficulty in identifying a "step" of two on top of a background of six particles, from one layer to another, as is the case of a $D^{\pm} \rightarrow \phi\pi^{\pm}$. The dimensions of each segment are 3.172 ± 0.003 cm in height and width, and 0.621 ± 0.006 cm in thickness. The total length of the target is 13.619 ± 0.056 cm. The z-position of the target is -1.590 meters from the upstream face, if we take as z = 0. the front (upstream) face of the magnet. The number density of particles in the target is 0.918×10^{25} cm^{-2}. The sensitivity for the experiment was determined to be 800 nb^{-1}. For more information see Section 2.7 .

2.3 The Magnet

We used a ferrite superconducting magnet producing a 16.9 KG centrally homogeneous magnetic field at maximum excitation of 180 amps. This superconducting magnet had a transverse kick in the x-z plane of 0.697 GeV/c. The magnet's x and y aperture is 1.20 and 0.80 meters respectively. The length is 2.54 meters. With this field and chamber set-up the single charged

track momentum resolution is given by,

$$\frac{\sigma_P}{P} = 0.0009(\mathrm{GeV/c})^{-1}\ P\ \sqrt{1 + P^2(35\mathrm{GeV/c})^{-2}}$$

2.4 MWPC System

We used multiwire proportional chambers (MWPC's) both upstream and downstream of the magnet. A multiwire proportional chamber consists of a plane of anode sense wires equally spaced and in parallel, positioned symmetrically between cathode high voltage planes. As charged particles traverse the gas-filled medium they produce electrons which are accelerated by the electric field causing avalanches near the space charge region of the anode sense wire. The pulses resulting from these avalanches are amplified and recorded while position information is obtained from the wire location. Thus space resolution depends solely on wire spacing. The parameters of these chambers are summarized in Table 2.1. The gas mixture used for these chambers, called the "magic gas", consisted of argon gas impregnated with 20% isobutane, 4% methyl, and 0.5% 13B1 freon. The operating voltage for these chambers ranged from 2,000 the 3,100 Volts. The readout system was composed of Fermilab designed shift registers and CAMAC crates.

2.5 Drift Chambers

Specifically for this experiment we constructed a set of two drift plane boxes each containing two x's (staggered by half a cell), one u, and one v planes , to replace the old magnetostrictive spark chambers of the FMPS. Drift chambers usually offer better spatial resolution than MWPC's. Our spatial resolution for these drift chambers was 150 to 200 μm as compared to the MWPC resolution of 1 to 2 mm. A drift cell consisted of a sense wire at ground potential and a field-shaping anode wire to correct the field in the low-field

regions between sense wires. The parameters used for these chambers are summarized in Table 2.2. The gas used for these chambers was an argon-ethane mixture at atmospheric pressure. These chambers were calibrated in the following way. By calibration we mean the conversion of a TDC readout into a distance. Our TDC least count was 1 ns and we operated these chambers in the common stop mode. Thus the relationship between time and distance is just $x = f(t_0-t)$, where t_0 and the form of the function f is determined from the data.

There was sufficient variation among the discriminators/amplifiers in our readout system to make it necessary to examine their performance individually. In Fig 2.3 a typical TDC readout is shown. A direct measurement of t_0 can be extracted from this spectrum as the arrow indicates. All t_0's were determined this way except for 57 cases among the 1472 wires. These exceptions are dead cells, cells at the far end of the planes with very poor statistics, or cells where no edge in the TDC spectrum existed. The minimum and maximum t_0's were 290 and 314 ns. Using a nominal velocity of 50μ/ns this variation corresponds to ± 600μ. Thus the gain from using individual t_0's is substantial. To determine the $f(t_0-t)$ form we note that a TDC spectrum is just the number of hits per unit time, $dN/dt = (dN/dx)(dx/dt)$. For a uniformly illuminated half cell of dimension h, $dN/dx = N/h$. Thus the number of hits with t less than t' is ,

$$N(t') = \int_0^{t'} \frac{dN}{dt}\, dt = \int_0^{t'} \frac{dN}{dx}\, \frac{dx}{dt}\, dt = \frac{N}{h} \int_0^{t'} \frac{dx}{dt}\, dt$$

where x(t) is the $f(t_0-t)$. Thus f is given by the integral drift time spectrum. After accounting for the t_0 variation, these integral spectra were formed using the same data for the t_0 study, but summed over all cells in a sense plane. These were then fit by a cubic polynomial. A quadratic form was found to be a poor repesentation. The normalization N/h was found to be

sensitive to the inclusion of spurious hits (electronic noise, cross talk, etc). Hence the normalization was scaled so as to produce the known wire spacing. The final scaled coefficients for all wire planes are given in Table 2.3 . Based on an efficiency study of the drift chambers with low intensity "straight throughs", a value of t_{max} = 250 ns was chosen. For any hit with t larger than t_{max} the x position used was that of the sense wire. For a TDC count of less than 10ns the x position was chosen to be the field shaping wire.

2.6 Cherenkov Counters

We used two nitrogen-filled Cherenkov counters at atmospheric pressure (CA,CB) to get a pion, kaon/proton separation between 6.0 and 22.0 GeV/c. A detailed description of these counters and how they were used for particle identification follows in Chapter 4.

2.7 The Scintillator Hodoscope.

The scintillation counter hodoscope, SCIWALL, was located downstream of drift station DB and was designed to shadow the central region of CB. It was primarily used by the trigger processor to better separate the pions and kaons in the forward direction, where the charged multiplicity was high. It consisted of 32 elements in 4 rows by 8 columns. The width of each element was 7.62 cm. The height of the two central rows was 20.32 cm each, while the height of the two end rows was 53.34 cm each.

2.8 Cross Section and Sensitivity

We used the Lund Monte Carlo [2.1] to generate "unbiased" inelastic events. We counted the number of events generated as ϕ, ϕK^+K^-, $\phi\phi$ etc. We kept

only events with one or more ϕ's decaying to K^+K^- in our momentum range of 5.7 to 23.0 GeV/c. We used a program called MONTE (see Appendix B) to simulate the FMPS and the trigger processor. Thus we generated "raw data" tapes and we processed these through the stream of programs used for the real data.

The acceptance is defined as,

$$A = \frac{\text{\# of events passing all cuts of a certain type}}{\text{\# of events generated of that type}}$$

The cross section is defined as,

$$\sigma = \frac{N_{obs}\ W}{N_b N_t\ A} \qquad \text{where,}$$

N_{obs} = # of observed events

W = correction factor for anything not included in the acceptance calculation, such as the kaon decay factor (for 4 kaons it is 1.61)

N_b = Effective beam

N_t = (# of target nuclei/unit mass) × (density) × (target length)

A = Acceptance

The inverse sensitivity is defined as

$$\frac{1}{S} = \frac{1}{N_b N_t}$$

$N_b = 8.7 \times 10^{10}$ = Total beam × live time

$$N_t = (6.02 \times 10^{23}/g) \times (12.4\ cm \times 1.032\ g/cm^3 + 0.711\ cm \times 2.70\ g/cm^3 + 0.51cm \times 1.046\ g/cm^3)$$

$$= 0.918 \times 10^{25}\ cm^{-2}\ .$$

Thus, $1/S = 1.252 \times 10^{-36}\ cm^2 = 1.252 \times 10^{-3}$ nb.

and $S = 800$ events/nb.

2.9 On-Line Analysis

Events selected by the trigger were written to tape by a PDP11/45

computer operating under RT-11. The words were taken from an event buffer in CAMAC modules interfacing the computer with the detector. Computer automated measurement and control (CAMAC) is a standardized modular instrumentation and digital system used for data acquisition [2.3]. RT-MULTI, the data acquisition program performed a series of operations on data buffers. It provided for user-written routines to be called during event read-in. Thus, diagnostic data can be accumulated and displayed on demand during data taking. For example, individual event displays, chamber hit distributions, etc., were obtained while acquiring data. Our RT-MULTI was arranged in blocks of 16 buffers, each 3,840 16-bit words long. Each buffer accommodates about 6 events with a maximum of 1,700 words per event. The data format was the following: The first five words of an event record are a header block containing the byte count and the record type (1 meant data, 2 meant between spills). Next were the 132 words of ADC's from the smart target, the dE/dx counter, CA and CB, and the scalers. 14 trigger latch words followed, together with the TDC block containing the drift chamber data. The shift register block came with the MWPC information. All these were written to tapes at 6250 bpi. We obtained 62 2400-ft. tapes containing a total of 3.65 million triggers.

TABLE 2.1

CHAMBER	No. WIRES	WIRE SEPAR. (mm)	ANGLE	Z-POSITION (meters)
BAY1	64	1.954	90.0	-33.2518
BAX1	64	1.954	0.0	-33.2358
BAY2	64	1.954	90.0	-21.1975
BAX2	64	1.954	0.0	-21.1823
BAV3	64	1.954	45.0	-21.0427
BBX3	32	1.954	0.0	-2.1852
BBX	32	0.977	0.0	-1.8796
BBY	32	0.977	90.0	-1.8732
AX1	256	0.977	0.0	-1.0542
AX2	256	0.977	0.0	-1.0486
AY1	256	0.977	90.0	-1.0430
AY2	256	0.977	90.0	-1.0375
AU	256	0.977	45.0	-0.9684
AV	256	0.977	135.0	-0.9629
BX1	384	2.000	0.0	-0.8131
BY1	192	2.000	90.0	-0.7201
BX2	384	2.000	0.0	-0.5727
BY2	192	1.954	90.0	-0.4784
BX3	448	1.954	0.0	-0.3616
BY3	256	1.954	90.0	-0.2827
BU	448	1.954	26.6	-0.0812
CX	512	1.954	0.0	0.6000
CY	320	1.954	90.0	0.6762
DX1	800	1.954	180.0	3.0010
DY1	320	3.175	90.0	3.0884
DU	864	1.954	15.0	3.1771
DV	864	1.954	165.0	3.2979
DY2	320	3.175	90.0	3.3857
DX2	800	1.954	0.0	3.4749
FPX	320	1.954	0.0	7.2113
FPY	320	1.954	90.0	7.2911
FPU	320	1.954	45.0	7.3744
FPV	319	1.954	135.0	7.4550

TABLE 2.2

CHAMBER	No. WIRES	WIRE SEPAR. (mm)	ANGLE	Z-POSITION (meters)
DAU	192	18.247	16.7	6.1982
DAV	192	18.247	-16.7	6.2173
DAX2	176	19.050	0.0	6.2365
DAX1	176	19.050	0.0	6.2554
DBU	192	18.247	16.7	6.9103
DBV	192	18.247	-16.7	6.9293
DBX1	176	19.050	0.0	6.9484
DBX2	176	19.050	0.0	6.9674

TABLE 2.3

TIME-TO-DISTANCE FIT COEFFICIENTS

$$x = at + bt^2 + ct^3$$

CHAMBER	a	b	c
DAU	0.523813×10^{-1}	0.874195×10^{-4}	-0.546074×10^{-6}
DAV	0.501267×10^{-1}	0.101261×10^{-3}	-0.560812×10^{-6}
DAX2	0.530898×10^{-1}	0.887889×10^{-4}	-0.522402×10^{-6}
DAX1	0.580992×10^{-1}	0.415380×10^{-4}	-0.405907×10^{-6}
DBU	0.467933×10^{-1}	0.163693×10^{-3}	-0.801838×10^{-6}
DBV	0.463697×10^{-1}	0.153624×10^{-3}	-0.737331×10^{-6}
DBX1	0.521113×10^{-1}	0.938282×10^{-4}	-0.531402×10^{-6}
DBX2	0.548139×10^{-1}	0.607818×10^{-4}	-0.428359×10^{-6}

REFERENCES

[2.1] Sjostrand T., Computer Phys. Comm. 27(1982)243.

[2.2] Marraffino J., E-623 note on Drift Chambers, Sept. 1982.

[2.3] CAMAC, A Modular Instrumentation System for Data Handling. TID-25875-7 (USAEC, Washington, 1972).

FIGURE CAPTIONS

2.1 Layout of the experimental apparutus. This is the x-z view.

2.2 Same as 2.1 but the y-z view.

2.3 Typical TDC spectrum from wire 94 of plane DAV. The arrow points to the t_0 selection.

Fig. 2.1

E623 LAYOUT

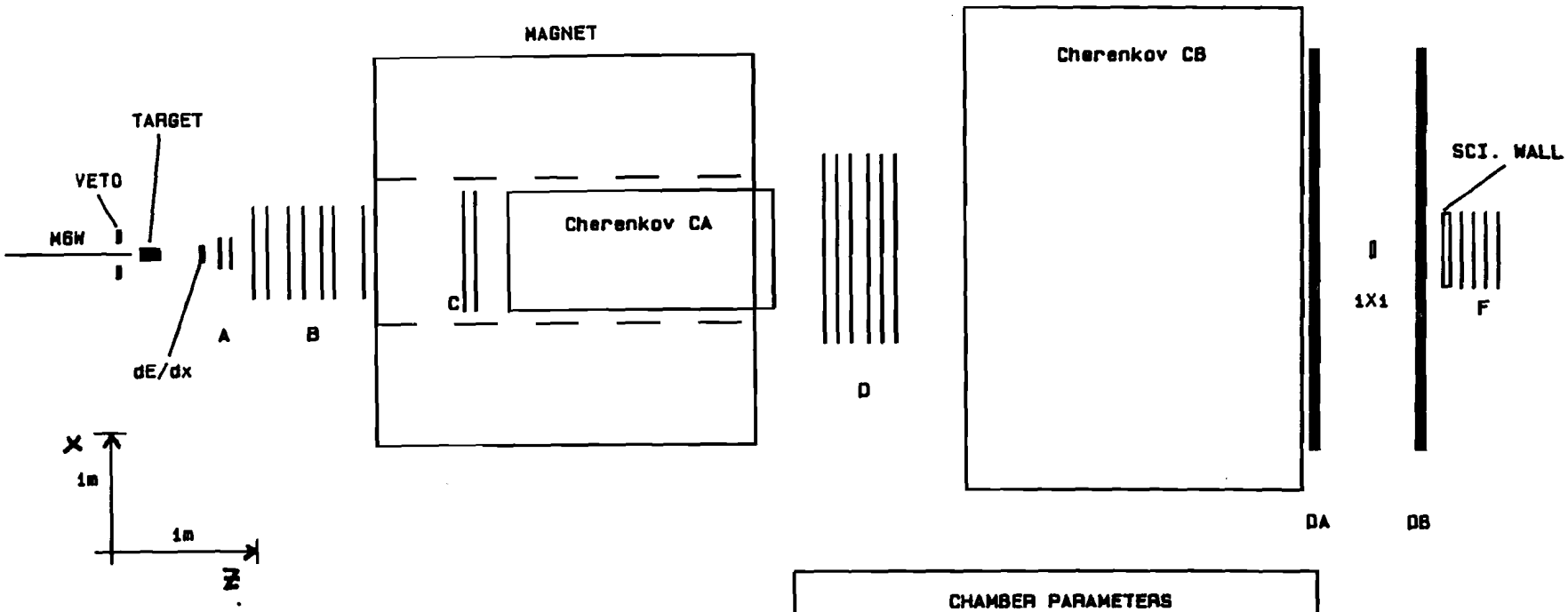

BEAM CHAMBERS

PWCs	Spacing	Planes
BA1	2 mm	Y X
BA2	2 mm	Y X V
BB	1 mm	X X Y

CHAMBER PARAMETERS

PWCs	Spacing	Planes	Wires
A	1 mm	X X1 Y Y1 U V	1536
B	2 mm	X Y X1 Y1 X2 Y2 U	2944
C	2 mm	X Y	832
D	2.3 mm	X Y U V Y1 X1	4416
F	2 mm	X Y U V	1280
Drift Chambers			
DA	19 mm	U V X1 X	736
DB	19 mm	U V X X1	736

Fig. 2.2

E 623 LAYOUT

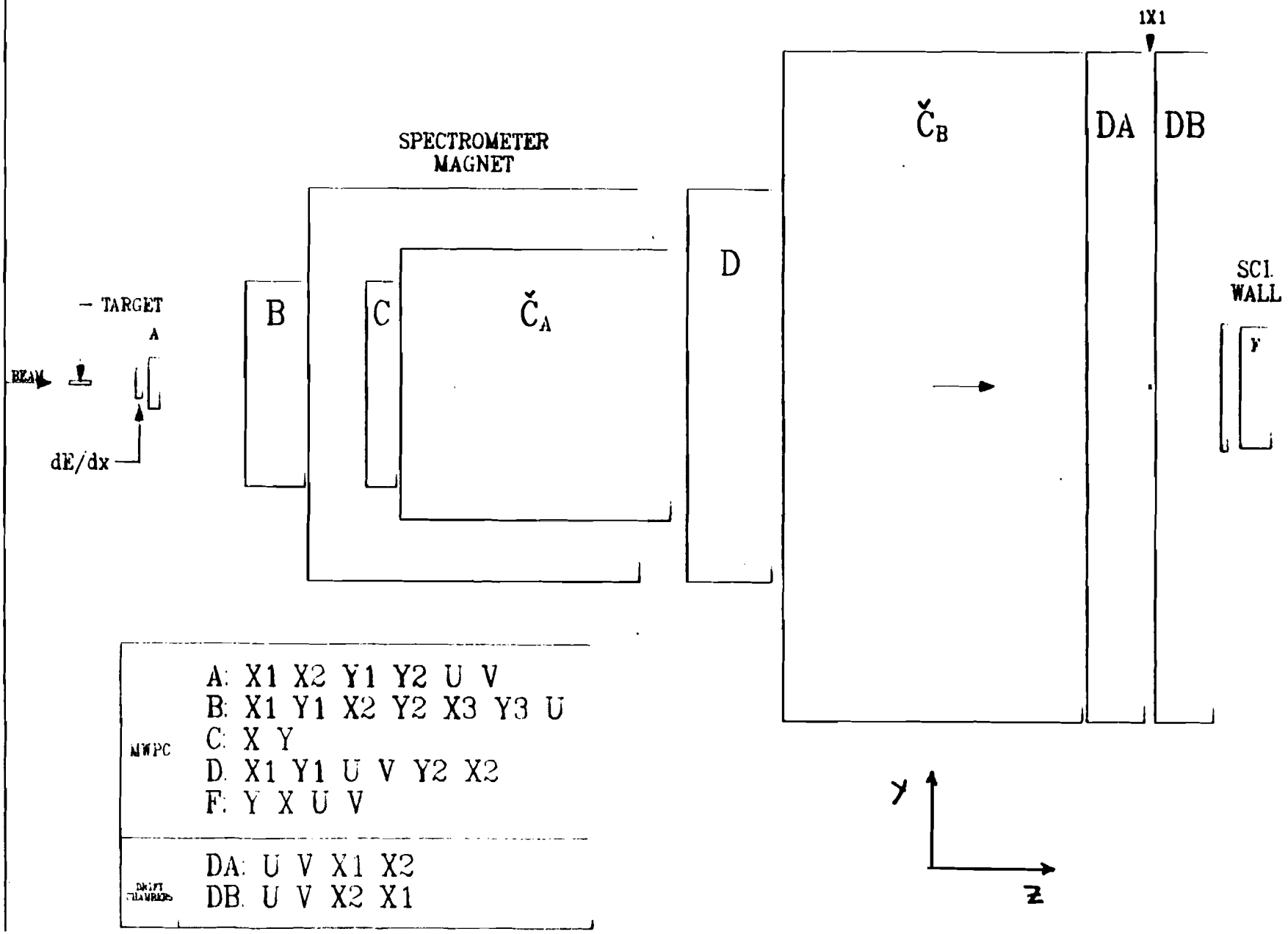

Fig 2.3

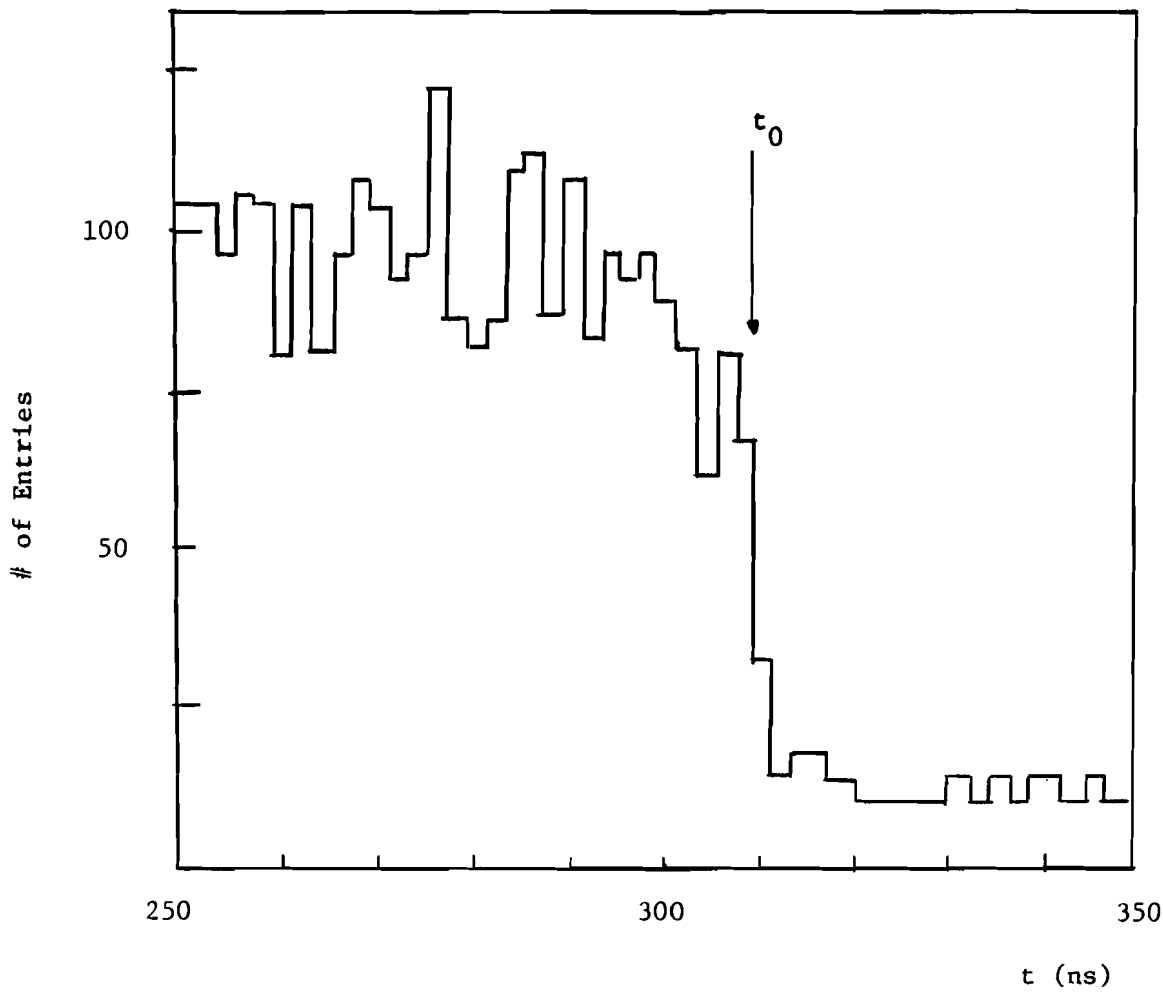

CHAPTER 3

DATA SELECTION

Crucial to this experiment was the design and operation of a high speed processor seeking events containing at least two pairs of oppositely charged kaons with effective mass near the ϕ meson mass [3.1]. The system which was constructed is basically a track finder which determines momentum and production angle as well as detector multiplicity. The system was fast, providing a trigger decision within 150 ns, and comparatively cheap (~20 K$).

3.1 Physical Description

The system is composed of both Fermilab-designed and commercial electronics (Fig. 3.1). The signals are preamplified and are logically OR'ed at the MWPC's P1, P2, and P3 by Fermilab designed electronics and sent to receiver/latches as differential ECL pulses. Phototube signals from the multicell Cherenkov counters C1 and C2 and scintillator hodoscope H1 are discriminated in standard NIM modules. These NIM pulses are also sent to Fermilab-designed latches. For each particle interaction the data is latched and sent to the processor as single-ended transmissions on wire-over-ground multiconductor ribbon cable.

The core of the processor resides in a crate manufactured by MUPAC [3.2] which supports both wire-wrap cards and backplane having very good ground plane and power distribution characteristics. Most of the system logic is implemented on these cards which provide an adequate environment for the ECL-10000 signals [3.3]. The use of the wire-wrap technique was very beneficial in the sense that logic modifications become simple and the processor can be reprogrammed very rapidly.

The latched data are sent to Fermilab-designed window discriminators for multiplicity cuts, and to commercial CAMAC modules which store all of the trigger data for readout to magnetic tape.

3.2 Track Recognition Logic

The detectors used in the trigger processor are three MWPC's, two Cherenkov counters, and a scintillator wall hodoscope. Each of these detectors is divided into 32 elements for triggering purposes.

A track is defined as a coincidental hit in all three elements of a predefined "road" through P1, P2, and P3. A point target plus these three points provides redundant four-point tracking. The coincidences are all performed in parallel rather than by looping over arrays of hits. This parallel processing accounts for the speed of the track finding algorithm. Each road is uniquely identified by its x-z plane production angle θ and momentum P. The production angle is given by the cell number in P1(0-31). The inverse momentum $S \equiv 1/P$, is measured as the difference, in units of P3 cells, between where the particle struck P3 and where a particle with infinite momentum and production angle θ would have struck P3. In Fig. 3.2 the logic diagrams are shown. The logic is arranged so that two neighboring elements of P2 are used in each "road". This compensates for the finite sizes of the beam, target, and detector hodoscopes.

We should note that the non-bend plane component of the production angle could be measured by means of a straight-forward addition to the above logic. For example, a redundant y measurement at P3 for each struck element in P3 would be provided by a coincidence involving two slant planes near this detector. That is

$$H(p,\theta,\theta_y) = P3_{j(p,\theta)} \cdot P3U_{m(j,\theta_y)} \cdot P3V_{n(j,\theta_y)} \cdot$$

This information would require additional fast OR amplifiers, latches, and another MUPAC crate (~10 K$). The measurement would be accessed in the same way that the momentum is retrieved from the road logic. Such a scheme was not implemented in this experiment since the processor reduced the trigger rate to an acceptable level in the presence of the maximum beam flux that the detectors could tolerate.

The kind of road definition used is quite efficient for finding tracks. Only when two tracks traverse exactly the same road is one of them missed. More important is the fairly coarse detector segmentation as compared with other trigger processors [3.4,3.5,3.6]. This size causes a significant number of accidental tracks occuring when a road is satisfied by unrelated detector hits caused by other tracks. The trigger recovers from this in several ways. It uses fast ripple-through electronics so that the interesting tracks are recognized within 75 nanoseconds. This reduces trigger deadtime and allows analysis at a higher rate. By reporting measurements of kinematic quantities for each track in addition to signalling simply the presence of some number of tracks [3.7], this processor allows a higher level decision to be made.

In this experiment the interesting tracks are kaons. However, the track finding is quite general, and the logic and detectors could be configured in such a way that the tracks of interest can be muons, protons etc.

A kaon is defined to occur when a road is satisfied and no cells in C2 which overlap this road have any light. The elements in H1 are placed so that in the small angle region, which has a high track density, they shadow the four-fold vertical segmentation of P3 (Fig. 3.3). With this arrangement, a kaon may be recognized even though a non-kaon shares the same road, if two tracks are produced at sufficiently different vertical angles.
The resulting kaon definition logic is of the form:

$$K(P,\theta) = P1_{\theta} \cdot \sum_{\mu=1}^{2} P2_{i(p,\theta,\mu)} \cdot P3_{(j,\theta)} \cdot \sum_{\nu=1}^{2} (\overline{C2}_{k(j,\nu)} \cdot H1_{m(j,\nu)}).$$

The geometrical arrangement and Cherenkov threshold are such that kaons with momenta between about 6 to 22 GeV/c are recognized.

As shown in Fig. 3.2 only the highest momentum track for each charge is reported to the higher level logic. This is the correct bias to use in this particular experiment where interesting tracks are kaons and pion contamination is present near the Cherenkov threshold.

Once a track recognition and momentum selection procedure is completed, the presence of a satisfied road with production angle θ and charge q is reported to the higher level logic. The momentum corresponding to each road is also available for readout as needed by the logic.

3.3 High Level Logic

A further trigger reduction is possible using the kinematic quantities (P, θ_x, θ_y) of interesting tracks found by the track finder. It is possible to compute values of variables, such as effective mass and transverse momentum very rapidly using memory lookup techniques. In this experiment a kaon pair consistent with a ϕ was ready within 150 ns after the time when detector data were available to the processor.

For the $\phi\phi$ trigger it is desirable to choose two K^+K^- pairs with small opening angles between the K^+ and K^- within a pair. At the same time, since a large $\phi\phi$ effective mass is wanted, a bias in favor of large opening angles between the pairs is imposed. This selection of tracks for calculational purposes is performed by the select board (Fig. 3.4).

The flags representing valid $K^{\pm}$ roads at various production angles θ are

presented to a pair of 32-wide priority encoders. The outputs of these encoders are two five-bit words θ_L^+ and θ_R^- which are the most positive and most negative production angles of all the satisfied kaon roads. Simultaneously, θ_L^- and θ_R^- are determined for the negative kaons. These four words are used to address the corresponding momenta determined in the road logic. Both the four momentum words S and the four words of θ are sent to the next module for use in the kinematic calculation.

These calculations are performed by a combination of arithmetic chips and PROMs loaded with functions (see Fig. 3.5). It was found that new PROM's could be easily burned using the on-line computer. This strategy was adapted instead of direct communication between CAMAC and processor.

The effective mass of a pair of kaons is given approximately by

$$M_{KK}^2 \approx M_K^2 \left[2 + \frac{P_2}{P_1} + \frac{P_1}{P_2} \right] + P_1 P_2 \left[(\theta_x^+ - \theta_x^-)^2 + (\theta_y^+ - \theta_y^-)^2 \right]$$

assuming small angles and relativistic tracks. The trigger processor could, in principle, calculate the effective mass of any pair of selected tracks. In this particular experiment, since low K^+K^- mass is required, and since the trigger rates are low, the approximation used is,

$$M_{KK}^2 \approx P_1 P_2 \, (\theta_x^+ - \theta_x^-)^2 = \frac{(\theta^+ - \theta^-)}{S^+ S^-} \quad .$$

A kaon pair is accepted as a valid ϕ if M_{KK}^2 as calculated is less than a Monte Carlo determined mass. In physical units the cut was about 1.02 GeV. Since the processor uses only the bend plane opening angle and thus always underestimates the mass, this cut is not unreasonably severe.

This processor also calculates the transverse momentum of the ϕ candidates in the xz plane as

$$PT = \left| \frac{\theta^+}{S^+} + \frac{\theta^-}{S^-} \right| \quad .$$

Again, a complete three dimensional calculation for any pair of selected tracks is easily obtained but unnecessary in the present application. The resulting value is compared with a switch-selected cut, and an output is set "true" if the cut is passed. Both the mass and P_T calculations are performed in parallel for the left and right ϕ candidates. To simplify the timing of logic external to the processor, none of the high level decision outputs are set until the processor is strobed by an external enable pulse.

3.4 Gating the Processor

Initial gating of the processor is provided by the IB, or interacting beam , signal which loads the latches (see Fig. 3.6). This signal is derived from the scintillation counters S_i where i=1,5 (Fig. 3.1). An incident beam is defined by $B = S1 \cdot S2 \cdot \overline{S3}$ where S1 and S2 are upstream of the target and define the beam size, while S3 is an annular counter which vetoes beam halo. The counter S5 is downstream of H1 and is used to require an outscattered beam particle. The counter S4 is directly downstream of the target, and the pulse height selection S4 > 3 is used to require an interaction in the target.

In order to reduce the system deadtime a signal E (meaning Enable) is rapidly formed (within 50 nanosec). If the event does not produce an E signal it is aborted. The signal E consists of IB and $\overline{S4 > 15}$ and $\overline{C2 > 5}$. The C2 multiplicity is derived from a NIM module.

The signal E gates the Fermilab-designed multiplicity window discriminators which produce a signal if the multiplicity N is between the limits, N ≡ (NL, NH) that is NL<N<NH. The six hodoscope multiplicities are used to form a signal EG (Event Gate) which is required in all subsequent trigger decisions. The logic schematic for the formation of EG and the trigger is shown in Fig 3.7.

The hodoscope multiplicity distributions observed in this experiment are shown on Fig. 3.8. Note that the true reconstructed track multiplicity downstream of the magnet is about 10, which is higher than the mean hodoscope multiplicity of about 7. The multiplicity limits are indicated on the Figure. The signal EG requires, P1 = (4,9), P2 = (4,9), P3 = (4,10), C1 < 7, C2 < 5, and H1 < 6. In addition since the processor preferentially selects events where the Cherenkov counter C2 is inefficient, the multiplicities in C1 and C2 are allowed to differ by up to two counts.

The purpose of these gates is to select interactions in the target (IB) with limited multiplicity and not too many pions (E). A further refinement is to limit the processor multiplicity to prevent accidental kaon candidates and also to use C1 to limit the effects of C2 inefficiency (EG).

3.5 Trigger Formation

The formation of the triggers is indicated in Fig. 3.7 . The signal EG is required in all triggers. The processor, which is gated by the signal E, provides signals K^+ and K^-, the multiplicities of K^+ and K^- candidates, and ML and MR signals, which are valid if the left-most and right-most K^+K^- pairs have low masses in the magnet bend plane. In addition, determinations of the transverse momenta of the left-most and right-most K^+K^- in the bend plane, PTL and PTR, are available for triggering purposes.

The trigger rates obtained in this experimant are given in Table 3.1. The trigger names correspond to the following logic requirements:

$$2K \equiv EG \cdot (K^+ = (1,4)) \cdot (K^- = (1,4))$$

$$\phi \equiv 2K \cdot (ML + MR)$$

$$\phi PT \equiv \phi \cdot (PTL + PTR)$$

$$4K \equiv EG \cdot (K^+ = (2,4)) \cdot (K^- = (2,4))$$

$2K\phi \equiv 4K \cdot (ML + MR)$

$2K\phi PT \equiv 2K\phi \cdot (PTL + PTR)$

$\phi\phi \equiv 4K \cdot (ML + MR)$

$\phi\phi PT \equiv \phi\phi \cdot (PTL + PTR)$

As can be seen in Table 3.1 the processor is a powerful tool in searching for rare processes. The reduction by track finding and multiplicity cuts is given by $4K/IB \sim 1/300$ and the effect of high level calculations is $\phi\phi/4K \sim 1/8$.

The trigger rate for $\phi\phi$ was low enough, given the maximum flux the detectors could tolerate, that the PTL and PTR signals were not used during the main data taking. The threshold values of PTL and PTR yielding the trigger rates of Table 3.1 correspond to 0.7 GeV/c in the magnet bend plane.

The results of the processor determination of K^+ and K^- multiplicity is shown in Fig. 3.9. Clearly the number of kaon candidates falls rapidly with multiplicity. The cut for the 4K triggers is shown in the figure. Also shown in Fig. 3.9 is the correlation between K^+ and K^- multiplicity. Clearly if $2K^+$ are found, one is likely to find $2K^-$, as expected for real events.

3.6 K^+K^- Mass Measurement Using the Processor

The cut for the triggering purposes was set at a limit of 8 processor mass units, i.e. $ML = mL<8$, $MR = mR<8$. The probability of occurrence of ML and MR in 4K events is shown in Fig. 3.11a. The positive value of the correlation function indicates that if the processor detects an ML signal it is likely to also detect an MR signal. This is expected since $\phi\phi$ production is known to be correlated [3.8].

By utilizing the latched hodoscope information one may study the details of the mass distribution on-line. In Fig. 3.11b are shown the probabilities of

mL and mR for $\phi\phi$ triggers. Clearly a band exists at low mL and mR values. In Fig. 3.11c the Monte Carlo result for the expected m distribution is shown for $\phi\phi$ events. Note that since ~50% of the $\phi\phi$ events give m<2, the trigger cut of 8 mass units is conservative.

A crude background subtraction is shown in Fig. 3.11d. Events with 0<mL<2 are plotted vs mR along with events with 4<mL<6, assumed to be background, normalized to equal rates for 4<mR<6. An excess of events remains at low mR, corresponding to the existence of $\phi\phi$ events. The very fact that $\phi\phi$ events can be seen on-line at the trigger level indicates the discrimination power of this trigger processor for rare event topologies.

3.7 Off-Line Analysis

The experiment generated 3.65×10^6 event triggers (runs 42 through 247), the earlier runs having very few triggers and even fewer good ones. The pattern recognition program "FLOWERS" reduced the number of triggers by about 10%, so after pattern recognition we were left with 3.2×10^6 event triggers.

The next stage of the data processing consisted of a 3-dimensional fit using the real field map of the magnetic field. Also all the tracks that "passed" the fitting routines were used in finding the production vertex point which was then used to determine the intercepts and slopes of these tracks. The output from the second stage of processing ("TIPTOE") was 2.1×10^6 triggers.

The third stage of the processing consisted of particle identification and produced a "level 1" Data Summary Tape. The output consisted of 1.8×10^6 triggers. A detailed description of this stage can be found in Chapter 4. The programs FLOWERS and TIPTOE are described below and a summary of the requirements made at each stage of the processing follows.

(i) FLOWERS

FLOWERS is a pattern recognition program written by J. H. Goldman of Florida State University to analyze the data for this experiment. The code is entirely in FORTRAN and it is easily transportable. The original version was written for a VAX 11/780.

The program is written with the idea that computer time is more important than space, and that clarity and ease of modification are more important than either time or space.

The main program called FLOWERS calls subroutine MASTER which controls the flow of the analysis. Subroutine MASTER has the following structure:

```
      CALL INIT        !Initialize everything in sight
200   CALL DATAIN      !Read in a physical record of data
300   CALL INIEVT      !Event initialization
      CALL UNPACK      !Unpack a logical record
      If no more data in the input buffer go to 200
      CALL SEVENT      !Setup the event
      CALL SMARTR      !Smart target analysis. Find the z position of the
                        vertex
      CALL VERTXB      !Use the beam to find the x,y position of the vertex
      CALL PASS1       !Pass #1 of pattern recognition
      .
      .
      .
      CALL PASSn       !Pass #n of pattern recognition
      Output the event buffer
      Go to 300 if more events exist, otherwise write out the end of run
      summary and terminate.
```

The heart of the pattern recognition algorithm is to find the track first in the downstream x-z view. The reasons are:

(1) The tracks are more spread out after passing through the magnetic field.

(2) Having found the downstream view, the upstream view is easily found, since all tracks come from a single point (our trigger rejected events with long lived neutral tracks).

(3) The trigger processor provides roads in the x-z view within which to search for the kaon tracks. This information considerably speeds up the processing.

Once the track has been found in the downstream x-z view, it is extrapolated to the mid-magnet point and from there to the production vertex. Upstream hits are then searched for, along the extrapolated track. A final χ^2 fit is performed to all the hits in the x-z plane. It is a three parameter fit, with the upstream and downstream portions of the track constrained to intersect at roughly the mid-magnet point. The actual intersection point used is computed first, from the rough values of the slopes.

In general it has been found that the number of hits in a track is more important than the value of χ^2/DF obtained from the fit. Thus if several tracks are found making use of the same hits, then the one with the most downstream hits is kept, while the χ^2/DF is used to choose between tracks with the same number of hits.

With the x-z projection of the track known, the next step is to search for the y-z projection, using the rotated coordinates (i.e u and v) as well as the y-coordinates. The formula used is: $y = (u - x \cdot \cos\theta)/\sin\theta$, where the u-coordinate is rotated by an angle θ. The y-z fit is a two parameter χ^2 fit to a straight line vs. arc length, i.e. it is a 3-dimensional reconstruction, with the y-coordinates allowed to have rotations about the z axis. The

y-coordinates are treated in an equivalent fashion as the u and v coordinates. The only difference is that the number of y-hits and the number of u,v-hits are stored separately for later reference. The reconstruction proceeds in three steps. First, a designated set of chambers is looped over, and each hit is used with the production vertex y-coordinate to generate a road. A second set of chambers is then searched for hits inside that road. Next, the entire set of hits found is used to generate a better road. Finally, all u, v, and y-coordinate chambers are searched for hits inside the road.

The following algorithm is used to choose between versions of the y-z projection match to a x-z track. The version with the most rotated chamber hit is chosen. If several versions have the same number of rotated chamber hits, then the version with the most y-coordinate hits is chosen. Finally if all else is equal, the version with the best χ^2/DF is kept.

PASS1 algorithm is an attempt to find all of the tracks that the on-line trigger processor would have called kaons. To accomplish this, the trigger processor software code is invoked to generate roads in the downstream x-z projection. For each road generated by the trigger processor code, the loops over chamber pairs are conducted in the following order: (DX1,DBX2), (DX2,DBX2), (DX1,DBX1), (DX1,DBX2), (DX1,DAX2), (DX2,DAX2), and (DX1,DAX1). If a loop is started over a pair of chambers, it is carried out to completion. The next loop is started only if no track was found in the previous loop. Before PASS1 is started the x,y,z coordinates of the production vertex are found by calling VERTXB and SMARTR. Then the algorithm described above is followed in order to find the kaon tracks. PASS2 through PASS5 routines are then called which loop over DX1 and DBX2, DX2 and DBX2, DX1 and DBX1, DX2 and DBX1 chambers respectively. At the end of these passes all the hits are marked as used and are not used in the following passes. PASS2 through PASS5 routines

will find the pions and all the tracks that did not trigger the apparatus since the trigger processor hardware covered 50% of CX, 62% of DX1, and 73% of DBX2. All this is then written out to tapes to be processed through the next stage which is called TIPTOE.

(ii) TIPTOE

This stage of processing has two basic goals: (a) refit the tracks the pattern recognition program FLOWERS found in order to improve the momentum resolution and (b) determine from these tracks a vertex point. The first goal is accomplished by doing a broken line least square fit on the tracks that the pattern recognition program found. First with the use of the upstream and downstream x-z slope estimators we determined the z-coordinate where the upstream and downstream portions of each track meet inside the magnet. All the planes are treated equally and a 3-dimensional fit is done using a look-up table in order to take care of edge focusing effects and bending in the y-z view. Once the slopes and intercepts of the tracks are determined the second goal is to use all the upstream tracks to determine a vertex point. The method used a linearized 3-dimensional least square fit. When a vertex is found all the tracks are tested to see how far they lie from that vertex. If a track is far off then it is dropped and the fit is done again using the rest of the tracks. This procedure is repeated until all tracks are reasonably close to the vertex. The minimum number of tracks required to find a vertex is 3. This procedure was tested with Monte Carlo events and was found to be efficient in rejecting tracks that came from secondary vertices due to decay of long-lived neutral particles (V^0). Once a vertex is found all the upstream tracks are then refitted using the known vertex as an additional constraint to determine the upstream slopes and intercepts again. These quantities are then passed on to the next stage of processing which is particle identification, described in detail in Chapter 4.

PROGRAM	EVENTS KEPT	REQUIREMENTS
FLOWERS	3.2×10^6	1. At least one positive track with momentum between 5.0 and 25.0 GeV/c. 2. At least one negative track as above. 3. At least three tracks.
TIPTOE	2.1×10^6	1. At least one possible K^+ with $5.5<p<25.0$ GeV/c 2. At least one possible K^- with $5.5<p<25.0$ GeV/c 3. At least three tracks pass the fitting routines. (The number of possible kaons was determined by counting the number of fitted tracks with $5.5<p<25.0$ in each cell in Cherenkov CB. If there was no light in that cell then all the tracks were counted as kaons. If there was light in the cell, all but one were counted, unless a track with momentum greater than 25 GeV/c was present at which point all the tracks were counted as kaons. In this procedure the kaons were assumed to have zero Cherenkov cone angle while pions were given a finite light cone, making it possible for a pion to be responsible for the light in more than one cell.)
ROSES	1.8×10^6	1. At least one identified K^+ ($5.69<p<23.0$) 2. At least one identified K^- ($5.69<p<23.0$) 3. At least three tracks. (The way this program worked will be described in detail in Chapter 4.)
DST	120,000	Events containing at least $2K^+$ and $2K^-$.

TABLE 3.1

TRIGGER RATES

NAME	σ (μb)
IB $\equiv \sigma_I$	30,000.
E	8,760.
EG	1,077.
2K	377.
ϕ	121.
ϕPT	60.
4K	94.
2Kϕ	51.
2KϕPT	26.
$\phi\phi$	12.
$\phi\phi$PT	4.

REFERENCES

[3.1] Fenker H. C., D. R. Green, S. Hansen, and T. F. Davenport, "The E-623 $\phi\phi$ Trigger Processor", FERMILAB-Pub-82/62-EXP.

[3.2] MUPAC Corporation, Brockton, MA, U.S.A.

[3.3] Blood W. R. Jr., MECL System Design Handbook, Motorola Inc. 1980.

[3.4] Martin J., et al., FERMILAB-Conf-81/40-EXP.

[3.5] Droege T. F., I. Gaines, and K. J. Turner, IEEE Trans. Nucl. Sci. NS-25,(1978)698.

[3.6] Bourgeois P., IEEE Trans. Nucl. Sci. NS-27,(1980)594.

[3.7] Etkin A., et al., Phys. Rev. Lett. 40,(1978)422.

[3.8] Daum C., et al., Phys. Lett. B 104,(1981)246.

FIGURE CAPTIONS

3.1 Plan view of the trigger detectors and block diagram of the trigger electronics.

3.2 Logic system defining a road and system for reporting the momentum of selected roads.

3.3 Detectors H1, C2, and P3 showing the horizontal and vertical relationship of the detector elements. The view is along the beam direction. Also shown is the logic to select kaons in this busy region.

3.4 Block diagram of the logic that chooses roads to be used as left and right kaon pairs and causes the corresponding measurements of P and θ to be used in the kinematic calculations.

3.5 Logic schematic to calculate mass and transverse momentum.

3.6 Logic schematic diagram for generation of the IB and E signals.

3.7 This is the schematic of the logic for generation of the signal EG and of the logic to use the signals K^+, K^-,ML, MR, PTL, and PTR, in the final trigger formation. The window discriminator cuts are shown with notation defined in the text.

3.8 Hodoscope multiplicity for the six detectors used in the trigger.
a) P1 b) C1 c) P2 d) C2 e) P3 f) H1 . The arrows indicate trigger limits.

3.9 Processor selection of kaons.
a) The correlation function for correlations between the K^+ and K^- multiplicity found by the processor.
b) Multiplicity distributions for K^+ and K^- found by the processor.

3.10 Diagram of an event selected by the processor. Solid lines represent the four tracks that triggered the processor. Dashed lines indicate the extra tracks tolerated by the processor.

3.11 Processor determination of masses.

a) Correlation function of ML and MR using 4K triggers.

b) Distribution of mL and mR within the trigger cut for $\phi\phi$ triggers. The tabulated numbers are the fraction of the $\phi\phi$ triggers yielding a particular mL and mR.

c) Monte Carlo generated distribution of the expected processor mass for $\phi\phi$ events.

d) Background estimation in $\phi\phi$ triggers. A column of b) expected to contain $\phi\phi$ events (solid line) is shown along with the a column expected to contain $\phi\phi$ background (solid circles), normalized to the same area for mR>4. Also shown is the expected residual shape due to ϕ events (open circles) using the shape of c).

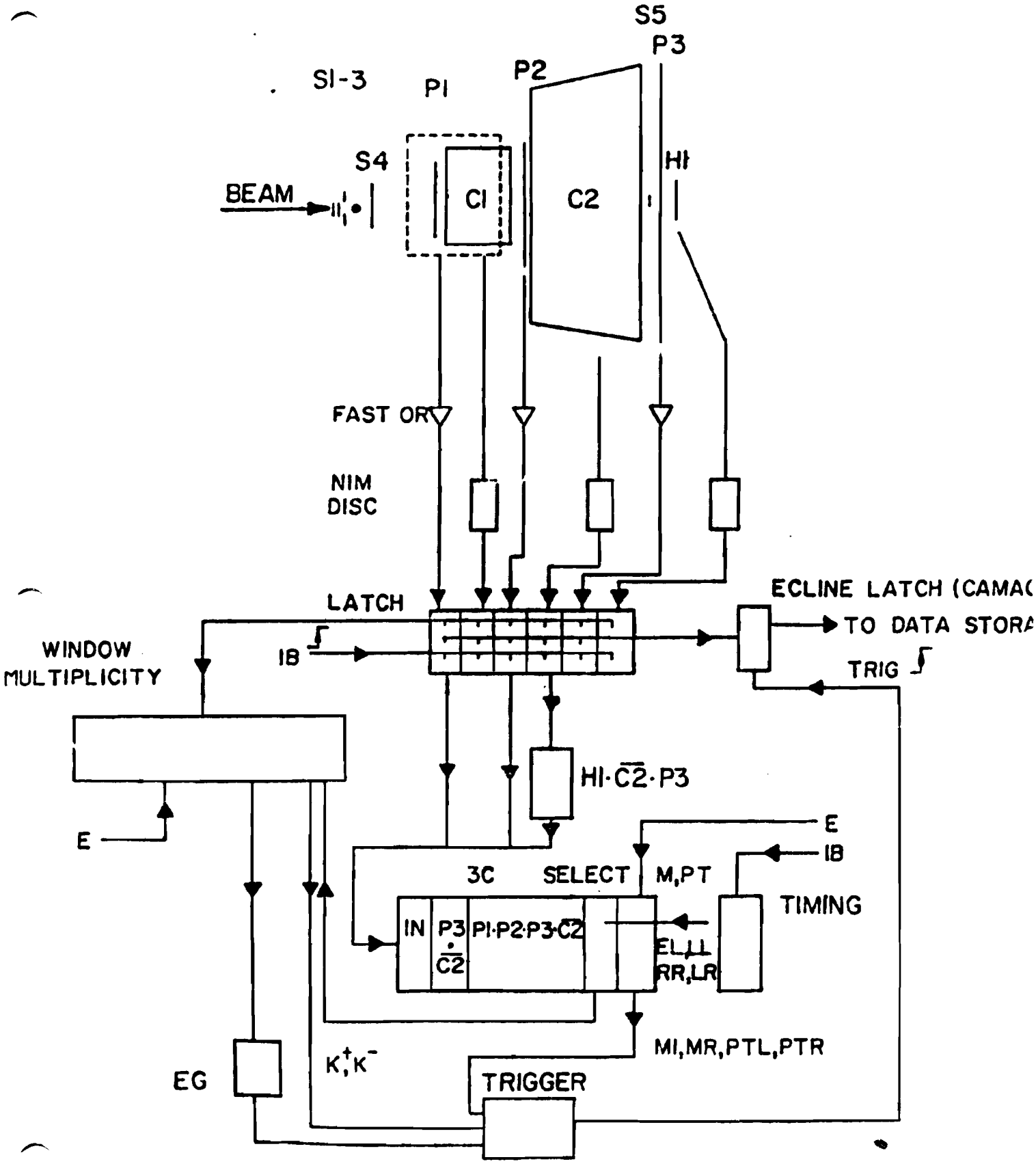
S5
P3
S1-3
P1
P2
S4
BEAM
C1
C2
H1
FAST OR
NIM
DISC
LATCH
ECLINE LATCH (CAMAC
TO DATA STORA
WINDOW
MULTIPLICITY
IB
TRIG
H1·C̄2·P3
E
E
IB
3C
SELECT
M,PT
TIMING
IN
P3
C̄2
P1·P2·P3·C̄2
EL,LL
RR,LR
M1,MR,PTL,PTR
EG
K+,K−
TRIGGER

Fig. 3.1

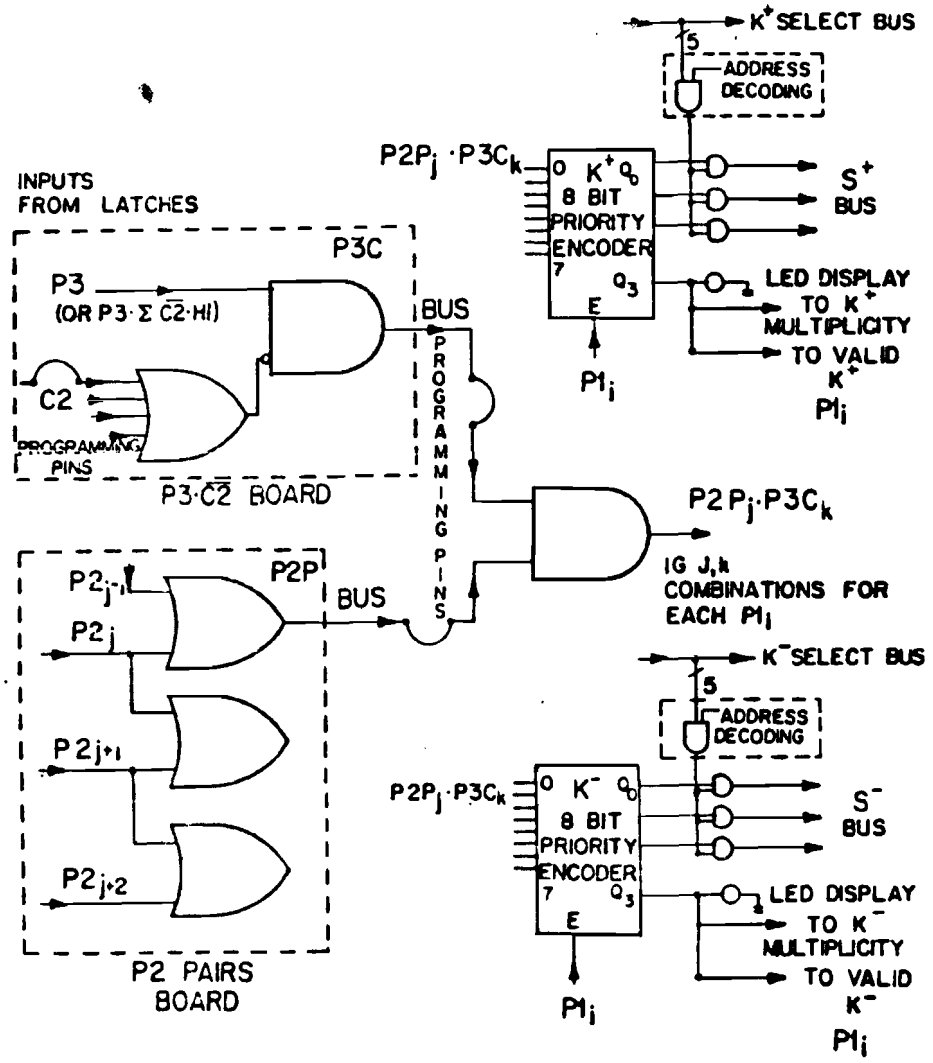

Fig. 3.2

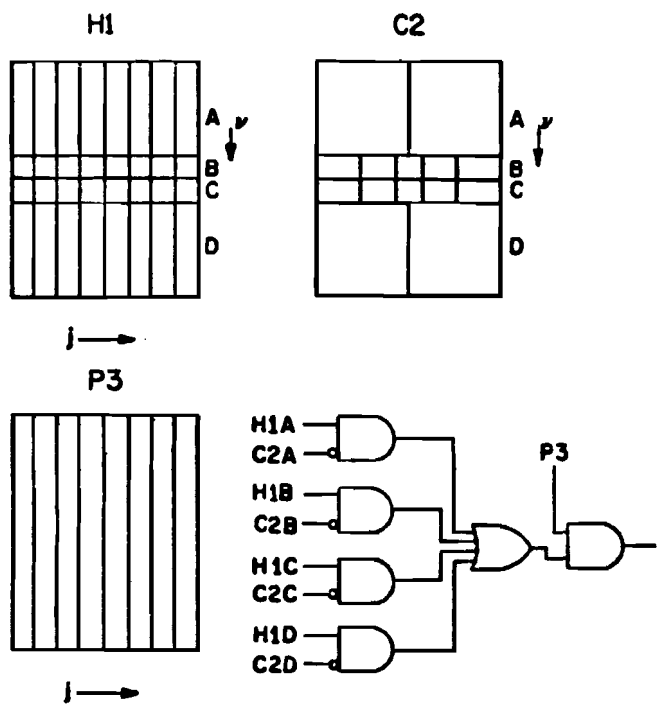

$$P3_j \cdot \sum_{\nu=1}^{4} (\overline{C2}_{k(j,\nu)} \cdot H1_{m(j,\nu)})$$

Fig. 3.3

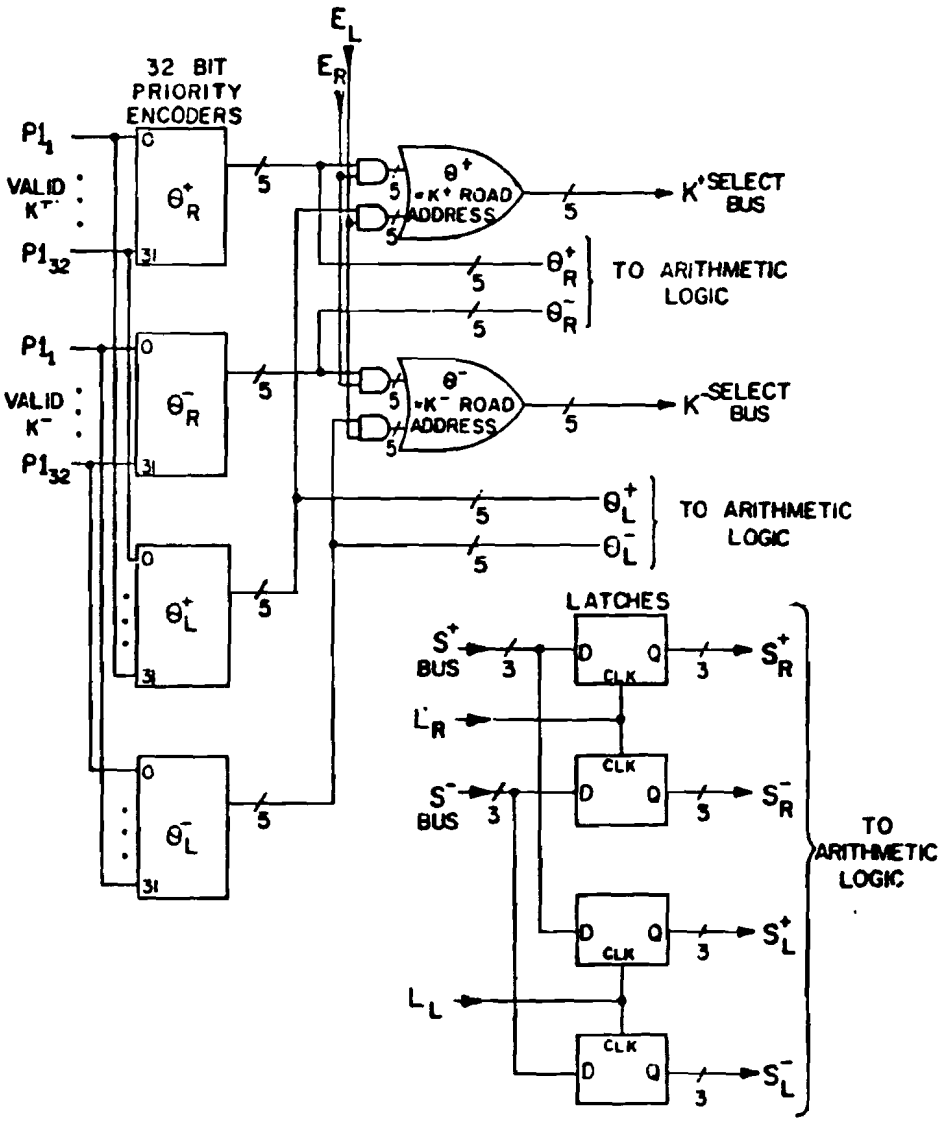
32 BIT PRIORITY ENCODERS
E_L
E_R
PI_1
VALID K^+
PI_{32}
θ_R^+
θ_R^-
θ_L^+
θ_L^-
θ^+ = K^+ ROAD ADDRESS
θ^- = K^- ROAD ADDRESS
K^+ SELECT BUS
K^- SELECT BUS
TO ARITHMETIC LOGIC
LATCHES
S^+ BUS
S^- BUS
L_R
L_L
CLK
S_R^+
S_R^-
S_L^+
S_L^-
TO ARITHMETIC LOGIC

Fig. 3.4

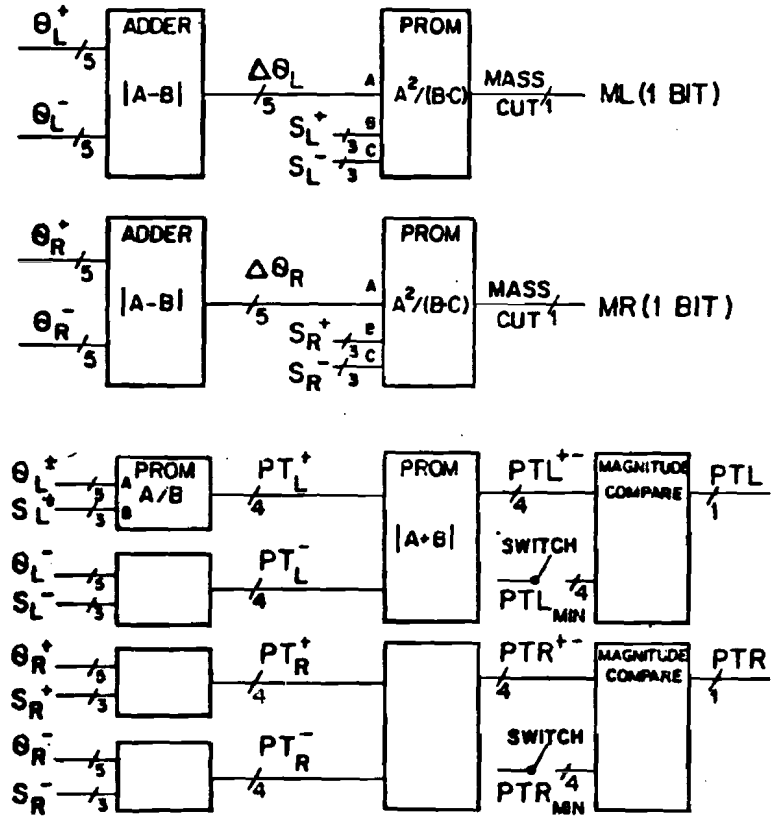
ADDER
|A-B|
$\Delta\theta_L$
$\Delta\theta_R$
PROM
$A^2/(B \cdot C)$
MASS CUT
ML (1 BIT)
MR (1 BIT)
PROM A/B
PT_L^+
PT_L^-
PT_R^+
PT_R^-
PROM |A+B|
PTL^{+-}
PTR^{+-}
SWITCH
PTL_{MIN}
PTR_{MIN}
MAGNITUDE COMPARE
PTL
PTR

Fig. 3.5

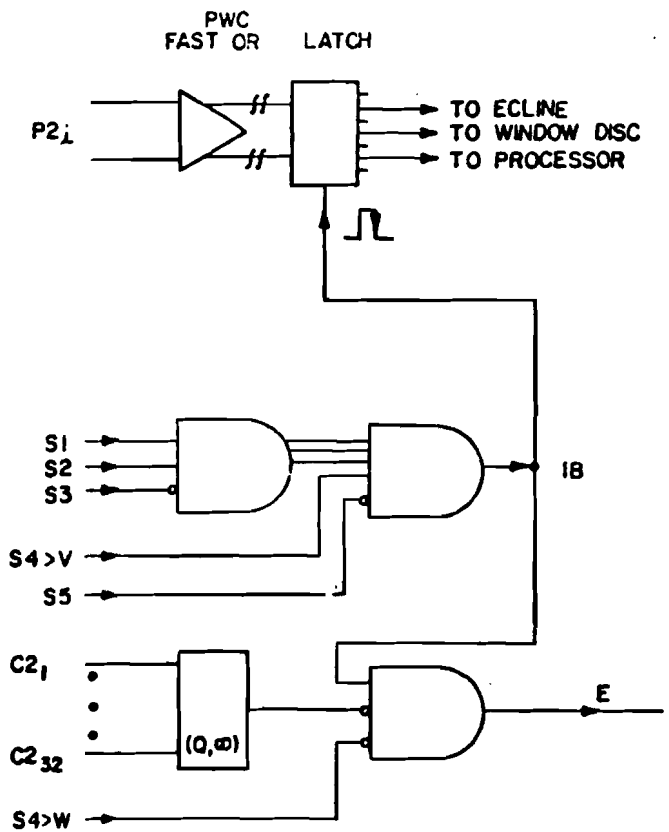
PWC
FAST OR
LATCH
P2
TO ECLINE
TO WINDOW DISC
TO PROCESSOR
S1
S2
S3
S4>V
S5
IB
C2
C2
(Q,∞)
S4>W
E

Fig. 3.6

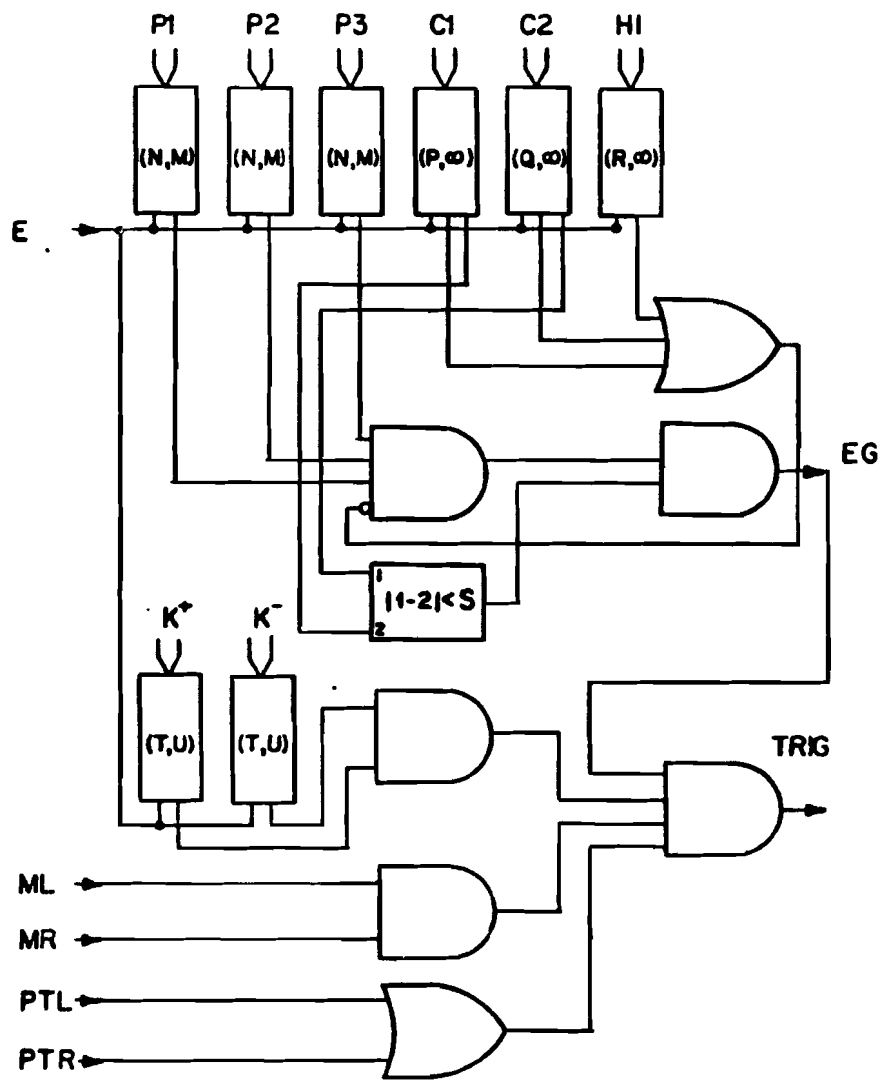
P1
P2
P3
C1
C2
HI
(N,M)
(N,M)
(N,M)
(P,∞)
(Q,∞)
(R,∞)
E
EG
|1-2|<S
K+
K-
(T,U)
(T,U)
TRIG
ML
MR
PTL
PTR

Fig. 3.7

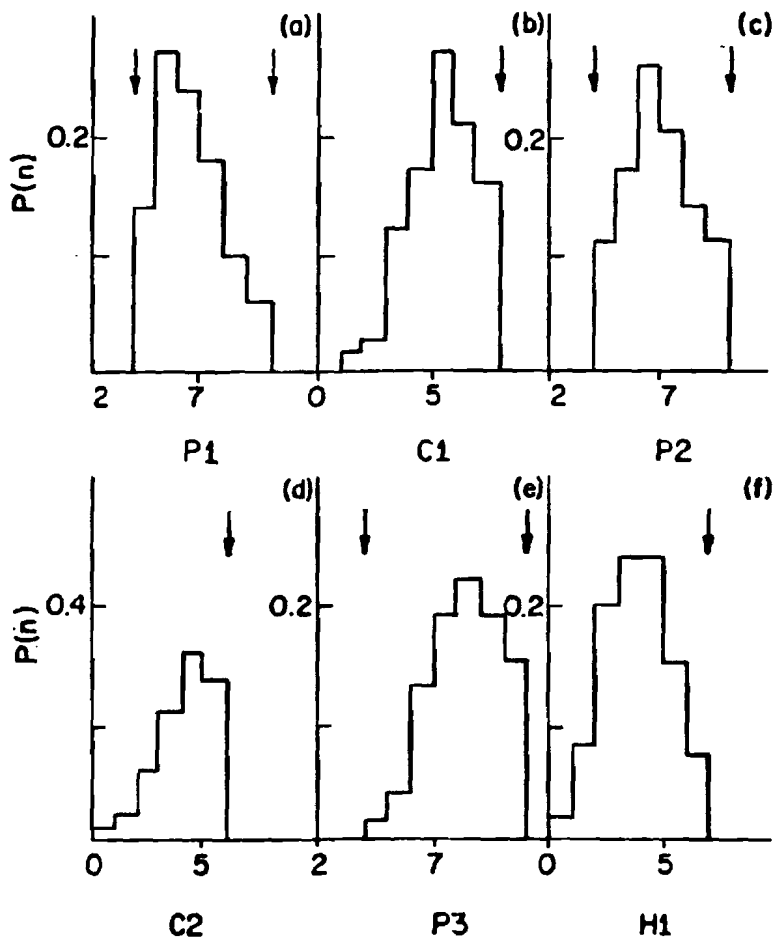

Fig. 3.8

$K^{\pm}$ DETERMINATION

a)

N_{K^-} \ N_{K^+}	0	1	2
0	-.025	-.16	-.003
1	-.20	.062	.23
2	-.059	.23	.32

$$\left[(P_{+-})-(P_{+})(P_{-})\right]/(P_{+})(P_{-})$$

b)

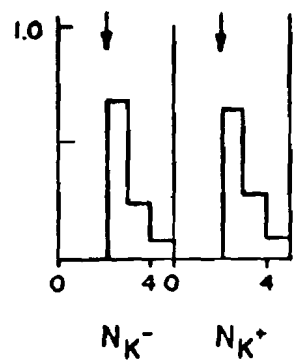

Fig. 3.9

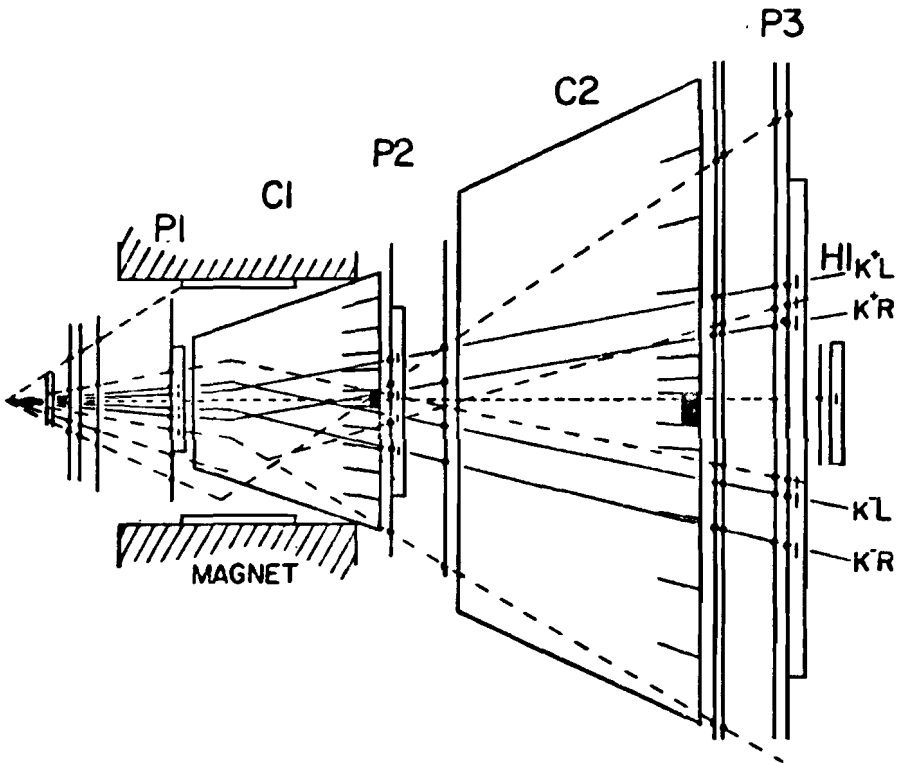

Fig. 3.10

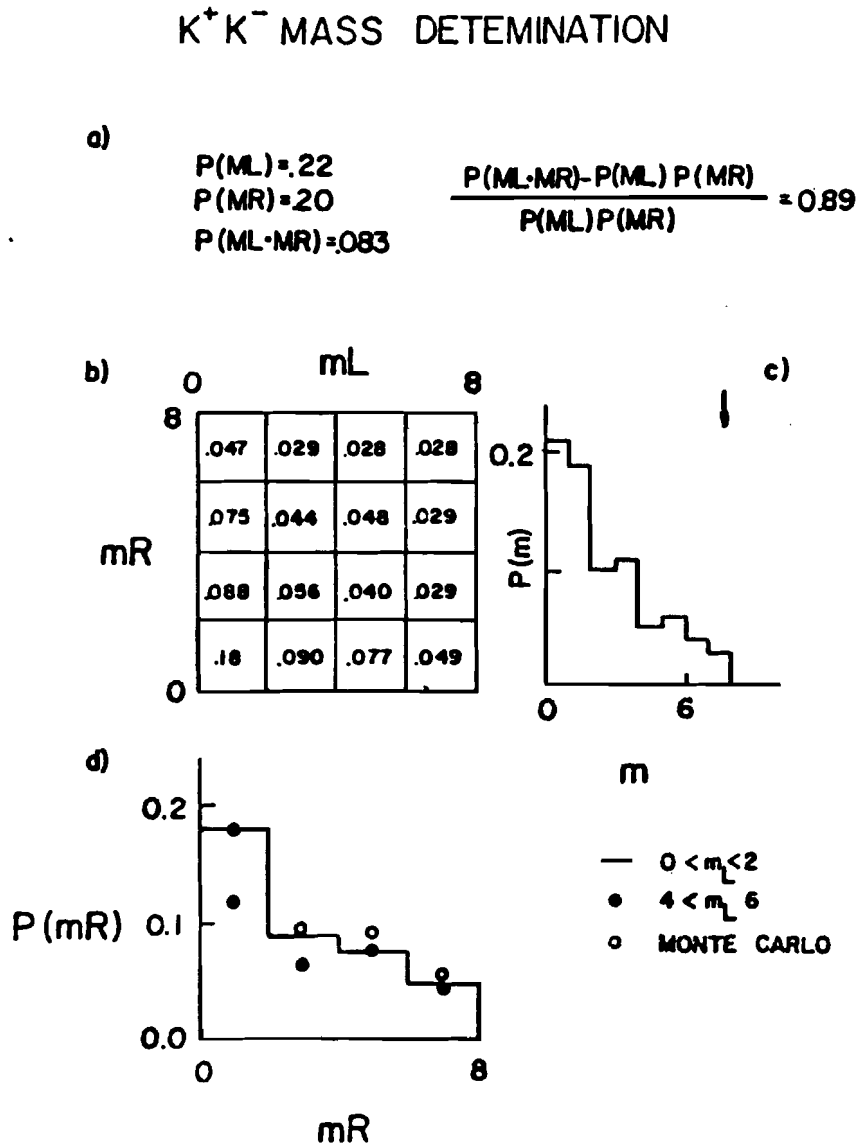

Fig. 3.11

CHAPTER 4

PARTICLE IDENTIFICATION

Threshold Cherenkov counters [4.1] are based on the principle that particles produce Cherenkov light, in a medium with refractive index n, if their velocity v exceeds the phase velocity of the medium c/n. This condition is written as:

$$\cos\theta_c = 1/n\beta$$

where θ_c is the opening angle of the Cerenkov light cone, and $\beta = v/c$. Since β is given by $\beta = 1 / \sqrt{1 + m^2/p^2}$, with p the momentum of the particle, then the momentum at which the particle starts producing light, the threshold momentum, is given by:

$$P_{Thres} = \frac{m}{\sqrt{n^2 - 1}}$$

with

$$\sin\theta_c = n^{-1} \sqrt{n^2 - 1 - m^2/p^2}$$

The interesting quantity however is the number of expected photoelectrons (N_e) in the light collecting photomultipliers. This is given by:

$$N_e = C \sin^2\theta_c \qquad \text{where}$$

$\sin^2\theta_c$ is given by the previous formula and C is a constant determined by the length of the counter, the refractive index $n(\lambda)$ as a function of the wavelength λ and the efficiency of the light collecting system.

4.1 Apparatus Description

In this experiment we used two multicell Cherenkov counters CA and CB (see Fig. 2.1 and 2.2). They were both filled with nitrogen gas at atmospheric

pressure in order to give comparable thresholds for light emission. In Fig. 4.1 and 4.2 is shown the projection of the Cherenkov counter mirrors in the x-y plane. Tables 4.1 and 4.2 summarize the parameters of these counters. Note that the beam is taken to be in the z direction. In the analysis we found that only CB was useful. CA unfortunately was located inside the magnet making particle identification very unreliable due to the fact that the particles were emitting light while they were bending in the magnetic field. Thus a particle of momentum ~ 8 GeV/c would typically give light to at least 3 mirrors. With an average multiplicity of 10 the task of identifying these particles from the pulse heights is close to impossible. Thus, the only use of CA was to provide an on-line multiplicity veto.

CB is composed of individually positioned mirrors of spherical shape treated with aluminum and overcoated with magnesium fluoride in order to reflect ultraviolet Cherenkov light. The mirrors were adjusted so that they would focus most of the light in Winston cones prepared in the same way. A laser-equipped theodolite was used to align these mirrors for maximum efficiency in light collection. The photomultiplier tubes (PMT's) used for CB were of two types. The first type was a 2-inch EMI9839KB for the 10 central cells of CB, and the second type was a 5-inch RCA8854 for the 20 side cells of CB. The fact that these PMT's were ~ 70% inefficient in the ultraviolet region and 60% of the Cherenkov light in nitrogen is in the ultraviolet, forced us to coat each PMT face with p-terphenyl, a wave shifter, absorbing ultraviolet and reemitting visible light (~ 5200 Å) improving our light collecting efficiency by 20%. The PMT output was routed both to an ADC and a commercial discriminator providing the input to the trigger processor. The ADC (LeCroy 2249A) had a 55 μs conversion time and was used for particle identification as will be described below.

In order to use the ADC information from CB we had to determine the characteristics of the detector. We assumed that the one photoelectron level and

the efficiency of a given mirror are characteristics independent of whether a slow or a fast track went through. Thus one can obtain these characteristics from the raw ADC's. From the design of the Cherenkov counter we expect a $\beta=1$ particle to produce an average of 6 photoelectrons. To determine the one photoelectron peaks for each mirror we took the real tracks, assumed they were pions, and propagated them through the counter to obtain the distribution shown in Fig. 4.3. As expected the distribution peaks at the expected number of photoelectrons for a $\beta=1$ particle. Comparing this distribution with the actual one, Fig. 4.4, obtained from the raw ADC's, we can assume that the peak observed is the expected pulse height for a $\beta=1$ particle and thus get the one photoelectron peaks for the mirrors after we subtract the pedestal values. The pedestals were read for each mirror in between beam spills to assure that any changes were recorded. Over the whole running period they remained stable to within 1%. The ADC's were dead some of the time for some mirrors, due to an AC coupling effect, that is the ADC value was read to be zero instead of the pedestal. A summary of the performance characteristics of CA anf CB is included in Table 4.2.

4.2 Cherenkov Algorithm

The Cherenkov algorithm consists of the following:

(a) For each track the Cherenkov cone is calculated as if it were a π using the appropriate radiation length, and each intersection area of the cone with the corresponding mirrors is weighted in order to take into account the 1/R dependence of the number of photons in the Cherenkov cone. Thus any strip of width α, height Y_p-Y_m, and radius R will have a weight:

$$W = [F(Y_p,R+\alpha)-F(Y_p,R)] - [F(Y_m,R+\alpha)-F(Y_m,R)]$$

where

$$F(X,Y) = [Y \cdot \ln(X/Y + \sqrt{(X/Y)^2+1} + X \cdot \ln(1+ \sqrt{\frac{(X/Y)^2+1}{(X/Y)}})]$$

For more information see section 4.3.

(b) For each track the expected number of photoelectrons is calculated as if the particle were a pion, a kaon, or a proton, using the formula:

$$N_{phe} = N_{max} \times [1 - (\frac{m}{p})^2 \times (n^2 - 1)^{-1}]$$

where $N_{max} = 6$, the average number of photoelectrons for a $\beta=1$ particle and

$n = 1.0003$ the index of refraction for nitrogen.

(c) All of the above is stored by mirror number. That is, the expected number of photoelectrons for each track is weighted with the factor determined in (a) and stored in the appropriate arrays.

(d) Next we loop over all the mirrors picking up first the mirrors with one track (or a portion of it) through, and then the mirrors with two, three, etc. and calculate an expected pulse height.

e) For mirrors with an observed pulse height below threshold, identify the tracks that go through according to their momentum. Note that the track has to have at least 30% of its weighted area inside the mirror in question to be identified.

(f) Pick up the mirrors that have a pulse height greater than the pulse height threshold and calculate the number of photoelectrons detected by this mirror. Then start looping over the tracks that hit the mirror or that have some piece of their cone in this mirror. Pick up first the tracks above proton threshold and subtract the calculated number of photoelectrons for this track from the number of photoelectrons in the mirror. Perform the subtraction as if the track were a pion, a kaon, or a proton, using the information from parts (a), (b) and (c), and

assign the identification that yields the result closest to zero. If there is still light, look at tracks above kaon threshold and do the same as for tracks above proton threshold. Assign the remaining tracks that go through this particular mirror according to momentum if no more light is left. Otherwise compare the remaining light with the expected value for these tracks and decide accordingly.

(g) The decision for the track is based on information obtained from the mirror the track went through.

The assignments are the following:

0 : $\pi/K/p$ for tracks below pion threshold (5.7 GeV/c).

1 : π (momentum between 5.7 and 23.0 GeV/c giving light)

2 : K/p (momentum between 5.7 and 23.0 GeV/c not giving light)

3 : p (momentum between 23.0 and 38.3 GeV/c not giving light)

4 : π/K (momentum between 23.0 and 38.3 GeV/c giving light)

5 : $\pi/K/p$ (momentum above 38.3 GeV/c giving light)

6 : unidentified tracks (the algorithm was unable to decide, e.g. track cone split between 4 mirrors, more than 4 tracks in one mirror etc.)

7 : tracks above proton threshold (38.3 GeV/c) with no light.

8 : tracks below pion threshold (alone in the mirror) with ADC on.

Each track is assigned a weight and a flag that signifies the quality of the identification decision. The weight is defined as follows:

$$\text{Weight} = \frac{99}{SU}$$

where SU = sum of the weighted areas of the Cherenkov cones of tracks that went through the mirror the decision for track "I" was based on, and were responsible for giving light.

For tracks below pion threshold, the weight is 0. So a weight of 99 for a kaon would mean that the mirror on which the decision for that kaon was based did not have any light in it. Note that if 3 tracks were in the same mirror and no light was present the weight of each track would still be 99. For pions the weight takes a slightly different meaning since all the tracks play a role now, however the fact remains that the greater the weight the better the quality of the decision.

In the analysis that follows in Chapter 6 for the $\phi\pi^{\pm}$ final state, we use as kaons only tracks with assignment of 2 and without any weight reduction. This comes from the fact that the ϕ signal observed is best under these conditions. For pions we chose to use tracks with assignments 1, 4, and 5, since all other assignments (0,6,8) are not well understood and are probably due to the inefficiency of the Cherenkov counter. More details will be given in Chapter 6 on how those decisions were made.

4.3 Distribution of the number of photons in a Cherenkov cone

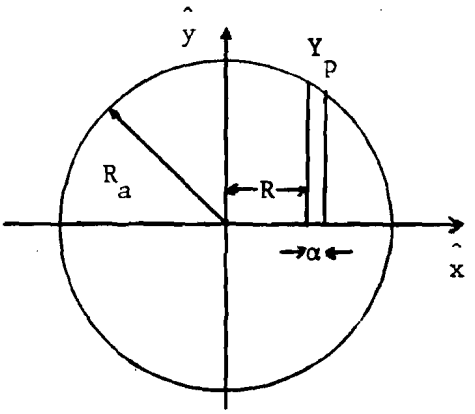

For α sufficiently small we can assume that over the range of α the value of Y will remain invariant.

The weight will go as $\frac{1}{R_a}$

Since all four quadrants in the Cherenkov cone are equivalent we calculate the weight of the strip of height Y_p and width α in one of the quadrants and extrapolate to the others. Calling the weight W we have

$$W = \int_R^{R+\alpha} \int_0^{Y_p} \frac{1}{\sqrt{R^2 + Y^2}}\, dY\, dR = \int_R^{R+\alpha} \sinh^{-1}\left(\frac{Y_p}{R}\right) dR$$

Using the substitution $Y = \frac{Y_p}{R}$

$$W = \left[R \cdot \ln(Y/R + \sqrt{(Y/R)^2+1}) + R \cdot \ln\left(1+ \sqrt{\left(\frac{(Y/R)^2+1}{(Y/R)}\right)}\right)\right]_R^{R+\alpha}$$

Calling $F(Y,R) = \left[R \cdot \ln(Y/R + \sqrt{(Y/R)^2+1}) + R \cdot \ln\left(1+ \sqrt{\left(\frac{(Y/R)^2+1}{(Y/R)}\right)}\right)\right]_R^{R+\alpha}$

Thus any strip of width α and height $Y_p - Y_m$ will have a weight

$$W = [F(Y_p,R+\alpha)-F(Y_p,R)] - [F(Y_m,R+\alpha)-F(Y_m,R)]$$

TABLE 4.1

CA DETECTOR CHARACTERISTICS

Number of Mirrors = 40

Average Length of Radiator = 1.78 m

Index of refraction n = 1.0003

Momentum thresholds: 5.69 23.0 38.3

for π K p

Mirror no.	Pedestal	One P.E. level	% Dead	% Overflow
1	37	18	1	0
2	46	34	3	0
3	38	52	0	0
4	46	54	0	5
5	32	78	0	7
6	37	26	0	20
7	37	29	2	9
8	35	45	5	3
9	26	26	6	0
10	31	20	2	0
11	6	34	8	0
12	20	80	5	0
13	34	86	0	0
14	20	30	0	4
15	77	90	0	9
16	43	17	5	15
17	32	38	3	7
18	38	37	2	3
19	45	22	3	0
20	70	21	0	0
21	37	38	0	0
22	40	40	0	0
23	37	63	3	1
24	32	58	10	7
25	32	68	0	30
26	33	67	20	4
27	27	33	3	1
28	30	40	4	0
29	30	40	2	0
30	31	49	6	0
31	37	20	0	0
32	30	13	0	0
33	40	23	2	0
34	39	26	3	5
35	42	20	0	7
36	46	24	5	3
37	45	28	0	2
38	43	12	4	0
39	44	32	2	0
40	40	23	2	0

TABLE 4.2

CB DETECTOR CHARACTERISTICS

Number of Mirrors = 30

Average Length of Radiator = 1.72 m

Index of refraction n = 1.0003

Momentum thresholds: 5.69 23.0 38.3

for π K p

Mirror no.	Pedestal	One P.E. level	% Dead	% Overflow
1	25	0	100	0
2	19	27	2	0
3	25	17	0	0
4	19	12	6	0
5	21	10	1	0
6	20	23	5	0
7	21	24	10	0
8	21	14	1	0
9	21	12	10	0
10	21	18	1	0
11	22	14	73	1
12	22	15	49	2
13	21	14	49	4
14	20	18	55	4
15	32	26	55	1
16	21	20	59	4
17	10	20	42	7
18	10	23	54	7
19	8	17	62	8
20	0	28	79	1
21	9	10	37	0
22	11	10	22	0
23	9	19	40	0
24	12	10	32	0
25	21	10	0	0
26	21	30	0	0
27	21	20	0	0
28	22	14	0	0
29	21	20	0	0
30	20	10	0	0

REFERENCES

[4.1] Cherenkov P. A., Phys. Rev., 52(1937)378,

Jelley J. V., Cherenkov Radiation and its Applications, New York, Pergamon Press, 1958.

FIGURE CAPTIONS

4.1 x-y plane projection of Cherenkov CA mirrors.

4.2 x-y plane projection of Cherenkov CB mirrors.

4.3 Expected pulse height distribution for real tracks that are assumed to be pions and are propagated through Cherenkov counter CB.

4.4 Real pulse height distribution for Cherenkov counter CB corresponding to the above tracks.

Fig. 4.1

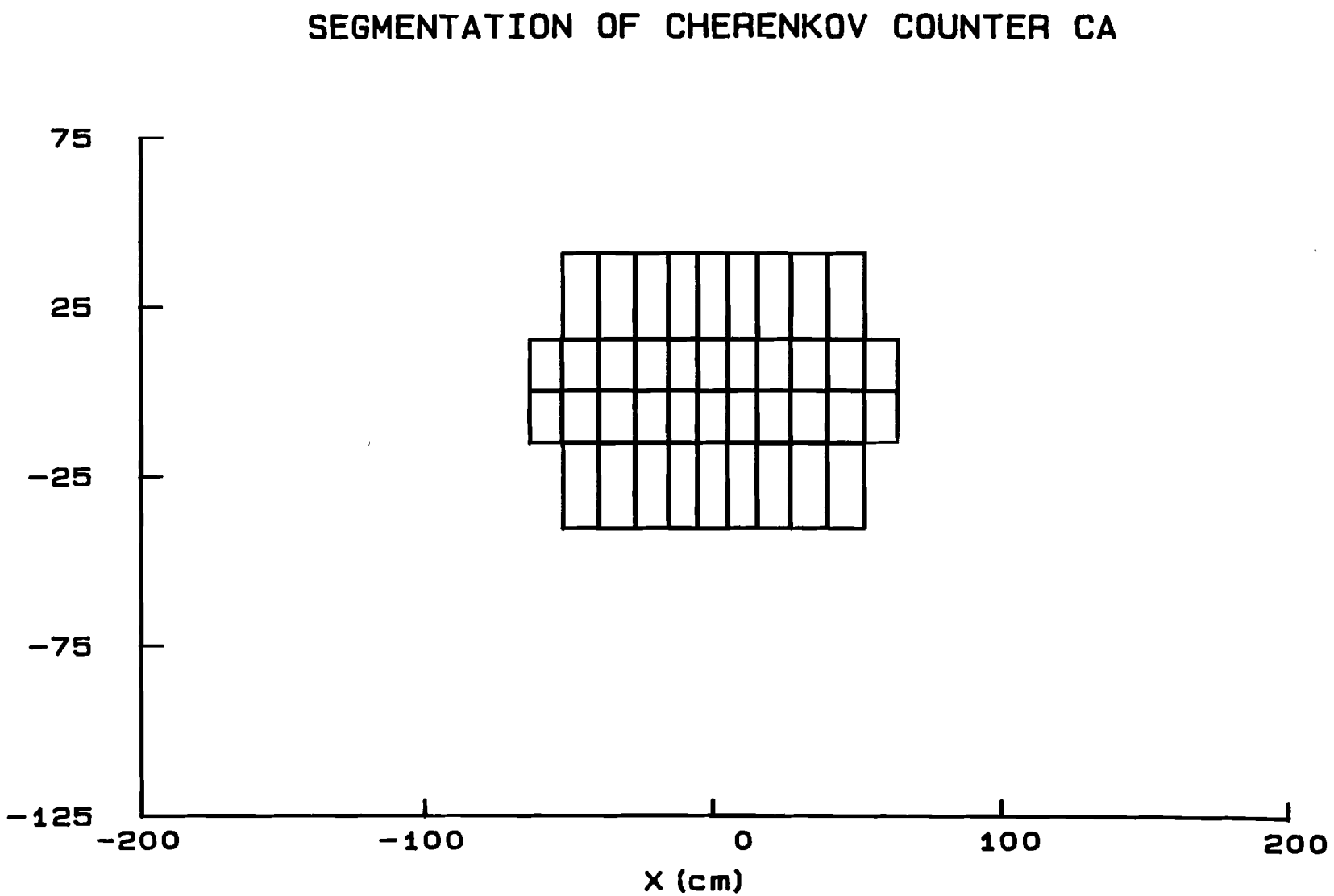
SEGMENTATION OF CHERENKOV COUNTER CA
75
25
-25
-75
-125
-200
-100
0
100
200
X (cm)

Fig. 4.2

SEGMENTATION OF CHERENKOV COUNTER CB

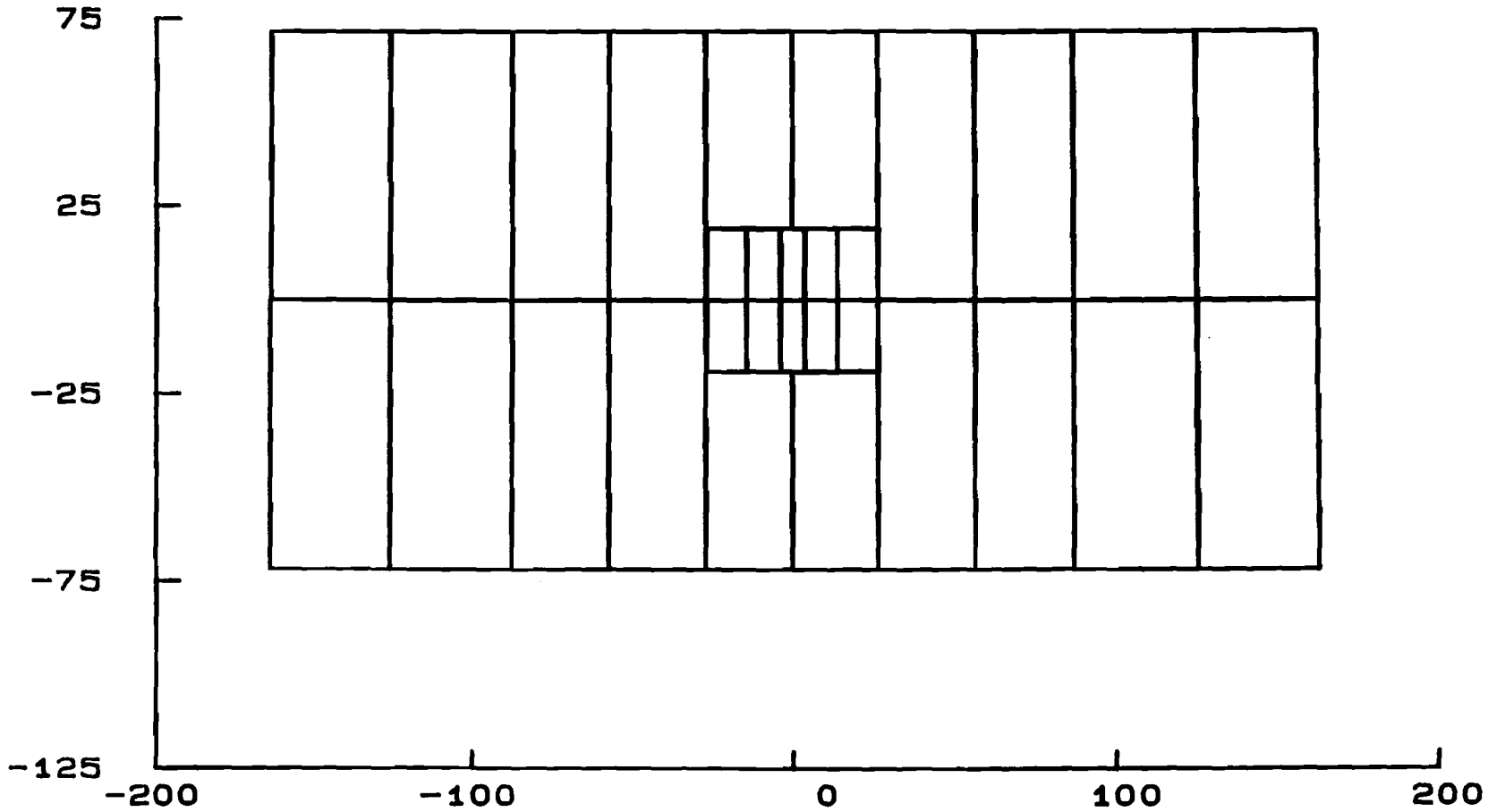

Fig. 4.3

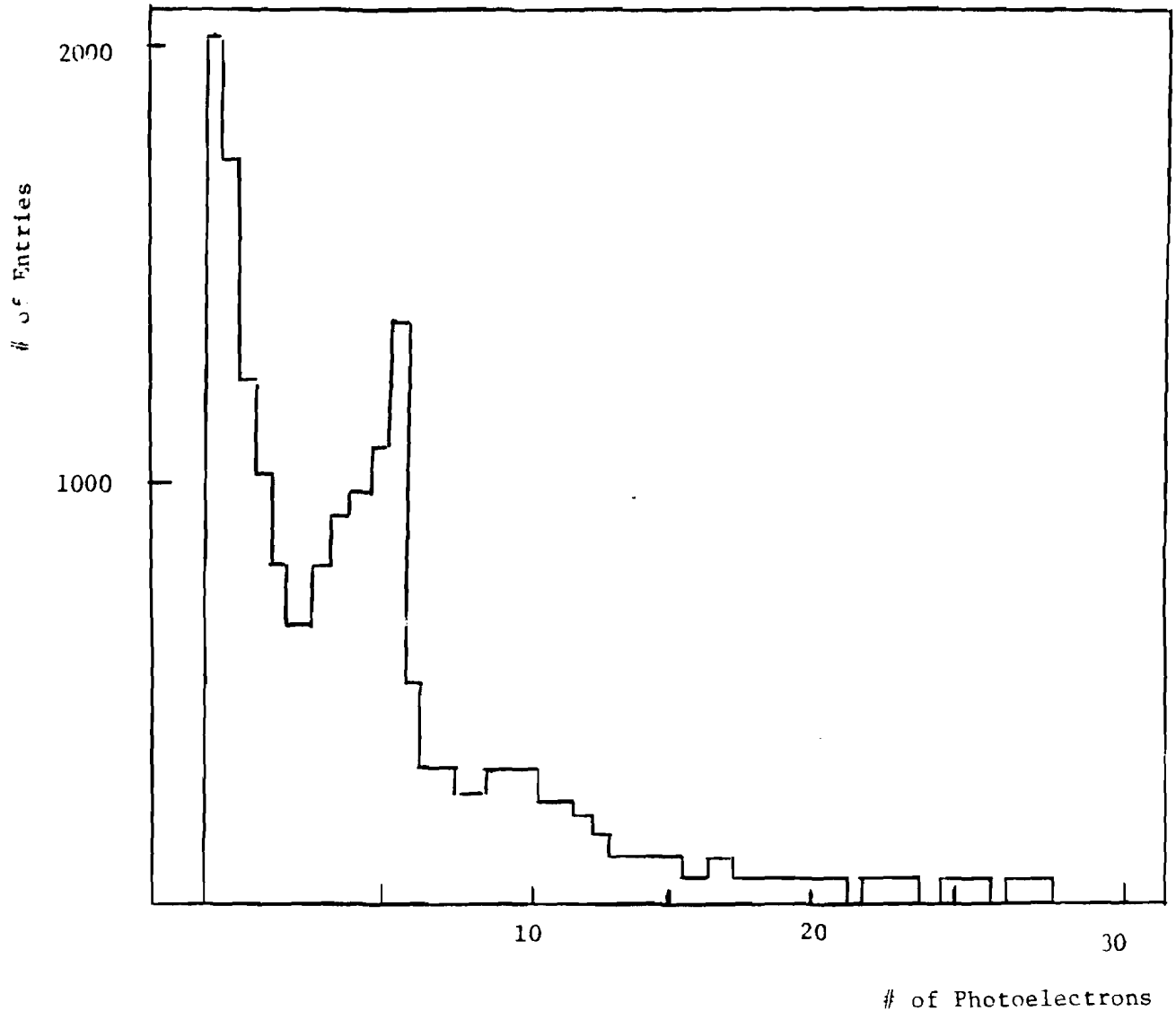

Fig. 4.4

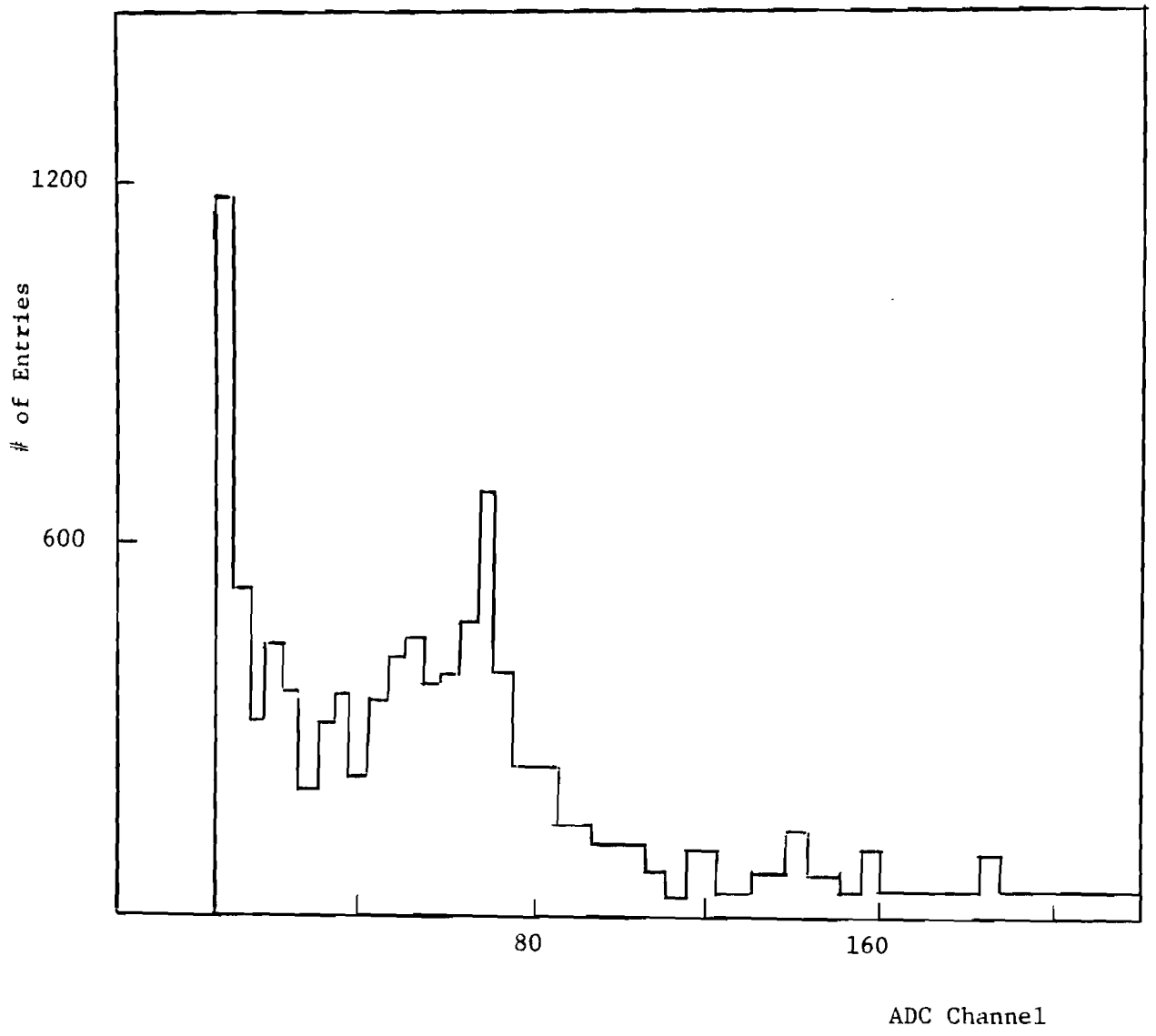

CHAPTER 5

CHARM PRODUCTION AND DECAY

In the current view of particle physics, quarks and leptons are believed to be the fundamental constituents of matter. The leptons (e,μ,τ) can be observed directly in nature but as yet quarks remain confined within the hadrons. The evidence for quarks is overwhelming as derived from the spectroscopy of known particles and the deep inelastic scattering of electrons and neutrinos from nucleons. It was, however, the observation of hadrons which could only be understood if an additional quark (charm quark) was incorporated in the existing view, that gave this theory believability. Thus the enormous number of known hadronic states can be simply explained by postulating the existence of 5 flavors of quarks (u,d,s,c,b). Mesons are then systems of a quark and an antiquark and baryons are composed of three quarks [5.1]. One should note that this scheme has its complications, mainly that in order to arrange the correct wavefunctions of baryons and account for the large cross section for production of hadrons in e^+e^- annihilation, a further degree of freedom called color should be added [5.2]. Each quark appears then in three colors, often called red, yellow, and blue. Thus, we can blame this extra degree of freedom for the non-observation of free quarks, by requiring that color should be confined. In other words, no state containing explicit color can be observed in nature. Note that this is an ad-hoc solution to this problem since the theory believed to describe strong interactions, namely Quantum Chromodynamics, has never proven color confinement.

Quarks and leptons experience weak and electromagnetic interactions. These interactions are mediated by the exchange of vector bosons ($\gamma,W^{\pm},Z$) and are united in current gauge theories. On the other hand the strong interaction is experienced only by the quarks and is mediated by colored vector gluons.

The electroweak interaction is described within an SU(2) × U(1) gauge group [5.3]. The strong interaction is believed to be described within a $SU(3)_c$ gauge group [5.4] which exhibits exact color symmetry. Although this group has many attractive features neither confinement of color has been proven nor the known spectrum of the hadrons has ever been reproduced.

5.1 The Need for Charm.

With the success of the quark model (SU(3) incorporating u,d,s quarks which has nothing to do with color $SU(3)_c$) many people considered the possibility that heavier quarks might exist. The motivation was due partly to notions of quark-lepton symmetry. At that time only 4 leptons were known (e, μ, ν_μ, ν_e) so why not 4 quarks [5.5]. This is not a very compelling reason for the existence of a fourth quark, but a problem in weak interaction phenomenology led Glashow, Iliopoulos and Maiani [5.6] in their classic paper of 1970 to provide a genuine reason for the existence of a fourth quark. For decades it had been known that weak interactions could be described by the interaction of two charge-changing currents with an interaction strength of $G_M \approx 10^{-5}/M_p^2$. We know now that neutral currents do play a role in weak interactions. Up until 1970 neutral currents were not seen nor were they ruled out at the level of G_F. There was an embarrassing problem however with this point of view. One class of neutral current interactions, the strangeness-changing hadronic weak currents, was known to be suppressed. The suppression factor was tremendous [5.7] as one can see from,

$$\frac{\Gamma(K_L^0 \to \mu^+\mu^-)}{\Gamma(K_L^0 \to \text{all})} = (9.1 \pm 1.9) \times 10^{-9}, \qquad \frac{\Gamma(K^\pm \to \pi^\pm e^+ e^-)}{\Gamma(K^\pm \to \text{all})} = (2.7 \pm 0.5) \times 10^{-7}$$

$$\frac{\Gamma(K^\pm \to \pi^\pm \nu\nu)}{\Gamma(K^\pm \to \text{all})} < 1.4 \times 10^{-7}, \qquad \left| \frac{M_{K_L^0} - M_{K_S^0}}{M_K} \right| = 0.7 \times 10^{-14}$$

The fact that strangeness-changing neutral currents could have been expected resides in the structure of the charge-changing hadronic weak current given by:

$$J^{\mu}_{\pm} = \bar{q}\,\gamma^{\mu}\,\frac{1}{2}\,(1 - \gamma_5)\,T_{\pm}\,q$$
$$\equiv \bar{q}_L\,\gamma^{\mu}\,T_{\pm}\,q_L$$

where the quark spinor q contains 4 × N components, N being the number of flavors, and $T_{\pm}$ is an N × N matrix which changes the electric charge by ± 1 unit. $q_L \equiv \frac{1}{2}(1 - \gamma_5)\,q$ is the left-handed part of the quark field. Strictly speaking the spinor field q_L is not left-handed. The operator $\frac{1}{2}(1 - \gamma_5)$ projects out the left-handed negative helicity part of the Dirac spinor u(p) only in the zero-mass limit. Thus for large momentum components of $q_L(x)$, $\frac{1}{2}(1 - \gamma_5)$ can be thought of as a covariant version of a left-handed projection operator. Unified field theories demanded that there should exist a neutral partner to these two currents coupling with the same strength G_F by:

$$J^{\mu}_{0} = \bar{q}\,\gamma^{\mu}\,\frac{1}{2}\,(1 - \gamma_5)\,T_0\,q \quad \text{where} \quad T_0 = [\,T_+\,,\,T_-\,]$$

The charged-current was known to have a Cabibbo form [5.8] given by:

$$J^{\mu}_{+} = \bar{u}\,\gamma^{\mu}\,\frac{1}{2}\,(1 - \gamma_5)\,(d\cdot\cos\theta_c + s\cdot\sin\theta_c) \quad \text{with} \quad \sin\theta_c = 0.23.$$

Therefore the neutral current should contain a piece of the form

$$J^{\mu}_{0} = \bar{u}\cdot u - \bar{d}\cdot d\cdot\cos^2\theta_c - \bar{s}\cdot s\cdot\sin^2\theta_c - \sin\theta_c\cdot\cos\theta_c(\bar{d}\cdot s - \bar{s}\cdot d),$$ suppressing the $\gamma^{\mu}\,\frac{1}{2}\,(1 - \gamma_5)$, giving rise to a $\Delta S = 1$ neutral interaction of order G_F.

5.2 The GIM Solution - The Charm Quark

The Glashow-Iliopoulos-Maiani solution [5.6] introduced a new, heavy, charge $\frac{2}{3}$ quark called c (for charm) with a left-handed weak coupling to the original Cabibbo combination $s\cos\theta_c - d\sin\theta_c$. It carried a new quantum number called charm conserved by the strong interactions. It can be seen that if

$$J^{\mu}_{+} = \bar{u}\,\gamma^{\mu}\,\frac{1}{2}\,(1 - \gamma_5)\,(d\cdot\cos\theta_c + s\cdot\sin\theta_c) + \bar{c}\,\gamma^{\mu}\,\frac{1}{2}\,(1 - \gamma_5)\,(-d\cdot\sin\theta_c + s\cdot\cos\theta_c)$$

the $\Delta S=1$ piece of the J_0^μ cancels and the neutral current becomes diagonal in all flavors. This current couples to itself and to leptonic neutral currents with strength G_F. Substituting in the above equation the Cabibbo rotated quark states $d' = d\cdot\cos\theta_c + s\cdot\sin\theta_c$, $s' = -d\cdot\sin\theta_c + s\cdot\cos\theta_c$ we get $J_+^\mu = \bar{u}\,\gamma^\mu \frac{1}{2}(1-\gamma_5)\,d' + \bar{c}\,\gamma^\mu \frac{1}{2}(1-\gamma_5)\,s'$. Thus the quark multiplets in terms of $SU(2) \times U(1)$ representations are:

$$\begin{pmatrix} u \\ d' \end{pmatrix}, \begin{pmatrix} c \\ s' \end{pmatrix}, u_R, d'_R, c_R, s'_R$$

and the weak charged currents cause transitions within the multiplets of left-handed quarks while right-handed ones are impotent. Moreover for the Cabibbo allowed weak transition $c \to s$ the selection rule $\Delta S = \Delta Q = \Delta C$ is apparent in analogy with the familiar $\Delta Q = \Delta S$ rule for weak decays of strange particles. Also the transition to strange quarks is favored over those to down quarks by a factor of $\sim \cot^2\theta_c \approx 16$ [5.6].

The GIM model solves the problems described above in the following way:

(a) No flavor-changing neutral current.

Since $T_0 = [\,T_+ , T_-\,]$ then $J_0^\mu = \bar{u}'\gamma^\mu \frac{1}{2}(1-\gamma_5)\,u' + \bar{c}'\gamma^\mu \frac{1}{2}(1-\gamma_5)\,c' - \bar{d}'\gamma^\mu \frac{1}{2}(1-\gamma_5)\,d' - \bar{s}'\gamma^\mu \frac{1}{2}(1-\gamma_5)\,s' = \bar{u}u + \bar{c}c - \bar{d}d - \bar{s}s$

if we ignore the gamma matrices and use the Cabibbo rotated states. Thus there are no flavor-changing neutral currents (i.e. no $s \to d$ transitions).

(b) Suppression of second order charged-current transitions.

In Fig. 5.1a the diagram showing the $K_L^0 \to \mu^+\mu^-$ is not the only one any more. A further diagram (Fig. 5.1b) should be added showing the charm quark contributions. The total amplitude from these diagrams is proportional to

$$\sin\theta\,\cos\theta\left(\frac{1}{\not{p} - m_u} - \frac{1}{\not{p} - m_c}\right)$$

A cancellation can occur in this amplitude for second order charged-current transitions. We see here that if $m_c = m_u$ then no $K_L^0 \to \mu^+\mu^-$ should occur, and if $m_c \approx \infty$, no suppression should be observed. Thus the upper limit on the mass

of the charm quark is set to be [5.9]: $m_c < 1.5$ GeV.

The properties of the charm quark then turn out to be very specific and are summarized as follows:

(1) New quantum number called charm in hadronic states

(2) Charge $Q = 2/3$

(3) Spin = 1/2

(4) Mass < 1.5 GeV

(5) (V-A) weak current and strength of interaction G_F

(6) Only charged-current weak transitions to the Cabibbo quark composition

(7) No flavor-changing weak neutral current transitions i.e. $c \to u$ or $s \to d$.

5.3 The Observation of Charm and its Decay

In October 1974 two spectacular observations were announced:

(a) A state of mass ~ 3.1 GeV called the J was observed in $pp \to e^+e^-X$ [5.10]

(b) A narrow resonance at 3.09 GeV called Ψ in the reaction $e^+e^- \to$ hadrons was seen [5.11].

In both cases the widths were consistent with the experimental resolution. A little later another narrow state the Ψ' was observed at a mass of 3.685 GeV. Although other interpretations were possible, like explicit excitations of the color degree of freedom, these states were widely believed to be the charm-anticharm quark mesons. The situation cleared up as more information (especially from e^+e^- annihilation) was gathered confirming the hypothesis of the charm quark. Specifically:

(a) γ-ray transitions from the Ψ' to other states in between the Ψ and the Ψ' were observed [5.12].

(b) A threshold was seen in the e^+e^- total cross section at energies greater than 3.8 GeV which also possessed resonant-like structure [5.13,5.14].

(c) A narrow meson, the D meson, was seen [5.15] at a mass of ~ 1.870 GeV decaying to $K\pi$ and $K\pi\pi$ final states.

5.4 Expected Properties of Open Charm Decay

We discuss here the properties of states characterized by non-zero charm values. Just like the strange quantum number, the charm quantum number of a given state is conserved in strong and electromagnetic interactions and can only change in weak interactions. The change occurs via a charged current as described in the previous sections. Thus only the lowest-lying states are unstable to weak interactions. Let us now concentrate on the spectroscopy of these lowest-lying states, and first the mesons.

The introduction of a charm quark changes the usual SU(3) octet to a SU(4) 15-plet plus a singlet. In Fig. 5.2 is shown the weight diagram of these pseudoscalar mesons. Table 5.1 lists the properties of the ones with charm content. We have implicitly assumed here that the pseudoscalars are the ones with the lowest mass (for the case of $c\bar{c}$ it has already been established that the η_c [5.16] is the lowest-lying $c\bar{c}$ state, the same being true for the $c\bar{d}$ and $c\bar{u}$ states).

We now consider the lowest-lying $J^P = \frac{1}{2}^+$ baryons for which the SU(3) octet becomes a SU(4) 20-plet. The weight diagram is shown in Fig. 5.3 and the properties of the charm-containing states are listed in Table 5.2 .The masses of the lowest-lying states can be estimated from the known J/Ψ mass and the masses of the light quarks, to be in the neighborhood of 2.0 GeV. From

$$J_+^\mu = \bar{u}\,\gamma^\mu \frac{1}{2}(1-\gamma_5)(d\cdot\cos\theta_c + s\cdot\sin\theta_c) + \bar{c}\,\gamma^\mu \frac{1}{2}(1-\gamma_5)(-d\cdot\sin\theta_c + s\cdot\cos\theta_c),$$

the weak current, and the smallness of the Cabibbo angle, one can obtain the hierarchy of the decay amplitude strengths corresponding to increasing powers

of $\sin\theta_c$. The selection rules are listed in Table 5.3 . One can make from this table some general comments about the decay properties of charm particles. If we consider only the dominant amplitudes, since they presumably lead to the most easily observable modes, we have the following:

(1) $\Delta S = \Delta C$ rule must be satisfied. Thus non-strange charmed particles will predominantly decay to final states which contain a strange particle.

(2) Decay modes containing leptons should be reasonably prominent. From W decay one would naively expect a 20% branching fraction for semileptonic decays to electrons, and similar branching fraction for muons (this however may be an overestimate since hadronic decays may be enhanced similarly to the strange decay enhancement observed for $\Delta I=1/2$ rule).

(3) $\Delta I_3 = \pm 1$ rule for hadronic decay modes will lead for appropriate initial I_3 values to exotic final states. e.g $D^+ \to K^-\pi^+\pi^+$ is an $I_3 = 3/2$ final state.

In Table 5.4 the known modes of open charm decay are summarized [5.17].

5.5 Hadronic Production of Charm

In this section I will present some recent theoretical approaches to hadronic charm production.

(i) Phenomenological Approach to Central Charm Production

The simple model of Bourquin and Gaillard [5.18,5.19] became popular as a model for charm production after its introduction in 1975. A single parametrization is applied to production of "non-leading" particles (π^-,ρ,ω,Ψ) in pp interactions over a wide range of energies, that is:

$$E\frac{d^3\sigma}{d^3p} = \frac{A}{(E_T + 2.7)\times 16.5}\, f(y)\, \exp\left(\frac{-25p_T}{\sqrt{s}}\right)$$

The choice of the rapidity y and transverse momentum p_T offer a better alternative than x_F and p_T due to the superiority of fitting the data.

In 1976 Bourquin and Gaillard [5.19] extended their parametrization to include pair production of states. The important assumption here was that due to local conservation of quantum numbers, particle pairs such as $p\bar{p}$ or $D\bar{D}$ come from the decay $R \to D\bar{D}$ of a single "state" R which has a mass M_R about 100 MeV above the combined pair mass. The invariant cross section for production of the object R is

$$\frac{\partial}{\partial M_R} E \frac{d^3\sigma}{d^3p} = A\, F(M_R, M_D)\, g(p_T^R, E_T^R)\, f(y^R)$$

Bourquin-Gaillard based this composite model on $\bar{p}$ and $\bar{K}$ production data. The overall normalization A is found to be the same order of magnitude for all particles considered. We summarize the main features of this model:

(a) Production is predominantly central with $d\sigma/dy$ nearly constant for low y and falling off at higher y; that is, the model is designed to reproduce the main features of the rapidity distributions of non-leading particles.

(b) The total $D\bar{D}$ cross section rises by a factor of about 2.5 over a C.M. energy range of 27 to 63 GeV.

(c) The low relative momenta of D and $\bar{D}$ in the C.M. implies close correlation between the two particles. This feature strongly influences total cross sections estimated from limited phase space by the use of Bourquin-Gaillard parametrization.

(ii) <u>Central Production in Perturbative QCD</u>

Perturbative non-scaling QCD was used by Combridge [5.20] for associated production of charm. The following processes to lowest order in QCD were considered:

(a) Flavor creation or fusion (Fig. 5.4a) : $q\bar{q} \to c\bar{c}$, $gg \to c\bar{c}$

(b) Flavor excitation (Fig. 5.4b) : $qc \to qc$, $gc \to gc$

The calculations use the parton model with some modifications listed below:

(a) The structure functions have scale breaking in Q^2 of the form predicted by Buras and Gaemers [5.21] for deep inelastic lepton-hadron scattering.

(b) The charmed sea structure function $c(x,Q^2)$ evolves as the normal sea, apart from a delay in the evolution which begins at $Q^2 = Q_0^2 = m_D^2$.

(c) The non-perturbative cut-off in flavor excitation is $t_{min} = -Q_0^2$.

The main predictions of this model are the following:

(1) Charm cross sections are predicted to range from a few microbarns at C.M. energies of 20 GeV to about 100 μb at 60 GeV.

(2) Flavor excitation cross sections are typically an order of magnitude larger than those for flavor creation.

(3) Production is central with a large increase at $x_F \approx 0$. as the energy increases.

(4) Gluon processes are dominant at high energies.

(iii) Forward Production

The observation in 1979 of forward production of charmed baryons at the level of a few hundred microbarns at the CERN ISR [5.22] was not anticipated in QCD models of the type discussed above. This led to new models which include flavor excitation [5.23], flavor excitation and recombination [5.24], intrinsic charm production [5.25], and large x_F counting rules [5.26]. All these models are sophisticated but none predict the observed quantities with considerable accuracy.

In summary, initial prediction of charm yields were based on central production models, both QCD-based calculations and phenomenological extrapolations of light quark production data. They were all found to be far from the measured values and the flavor excitation mechanism $gc \rightarrow gc$ was then suggested to account for the discrepancy. Flavor excitation can probably account for the forward production of Λ_c in pN and $D,\bar{D}$ in πN interactions.

These calculations however have large uncertainties due to lack of knowledge of the charm sea structure function and other parameters.

Inclusive differential cross sections for central charm production are parametrized in the following way:

$$E\frac{d^3\sigma}{dp^3} \propto x_F \frac{d^2\sigma}{dx_F dp^2} \propto (1 - x_F)^n e^{-bp_T^2}$$

based largely on experimental data on light particle production. We should note that the central form $x_F \frac{d\sigma}{dx_F} \propto (1 - x_F)^n$ goes over to $\frac{d\sigma}{dx_F} \propto (1 - x_F)^n$ for processes involving valence quarks since the 1/x factor arises from parton densities at $x_F \approx 0$.[5.27]. Counting rules provide guidelines for the value of n [5.26] in forward production.

We can safely conclude that theory up to now has provided little guidance on the nature of $c\bar{c}$ correlations in the production process. Thus inclusive cross sections extracted from observations of charm production with a limited angular acceptance are very uncertain. Finally we should note that the situation of charm production is still very open and the end does not seem to be near.

TABLE 5.1

Pseudoscalar meson states with charm quarks

Name	Quark content	SU(3)	I, I_3	Strangeness	Charm
D^+	$c\bar{d}$	$\bar{3}$	1/2,1/2	0	+1
D^0	$c\bar{u}$	$\bar{3}$	1/2,-1/2	0	+1
F^+	$c\bar{s}$	$\bar{3}$	0,0	+1	+1
$\bar{D}^0$	$\bar{c}u$	3	1/2,1/2	0	-1
D^-	$\bar{c}d$	3	1/2,-/12	0	-1
F^-	$\bar{c}s$	3	0,0	-1	-1
η_c	$c\bar{c}$	1	0,0	0	0

TABLE 5.2

$J^P = 1/2^+$ baryon states with charm quarks

Name	Quark content	SU(3)	I, I_3	Strangeness	Charm
C_1^{++} or Σ_c^{++}	cuu	6	1,1	0	1
C_1^{+} or Σ_c^{+}	$c(ud)_{sym}$	6	1,0	0	1
C_1^{0} or Σ_c^{0}	cdd	6	1,-1	0	1
S^+	$c(us)_{sym}$	6	1/2,1/2	-1	1
S^0	$c(ds)_{sym}$	6	1/2,-1/2	-1	1
T^0	css	6	0,0	-2	1
C_0^{+} or Λ_c^{+}	$c(ud)_{anti}$	$\bar{3}$	0,0	0	1
A^+	$c(us)_{anti}$	$\bar{3}$	1/2,1/2	-1	1
A^0	$c(ds)_{anti}$	$\bar{3}$	1/2,-1/2	-1	1
X_u^{++} or Ξ_c^{++}	ccu	3	1/2,1/2	0	2
X_d^{+} or Ξ_c^{+}	ccd	3	1/2,-1/2	0	2
X_s^{+}	ccs	3	0,0	-1	2

TABLE 5.3

Selection rules for charm quark decay

Amplitude dependence on $\cos\theta_c$	Selection rules: c decay	Selection rules: $\bar{c}$ decay
	Leptonic or semileptonic modes	
$\cos\theta_c$	$\Delta S = \Delta C = \Delta Q = -1$	$\Delta S = \Delta C = \Delta Q = +1$
	$\Delta I_3 = \lvert\Delta I\rvert = 0$	$\Delta I_3 = \lvert\Delta I\rvert = 0$
$\sin\theta_c$	$\Delta C = \Delta Q = -1$	$\Delta C = \Delta Q = +1$
	$\Delta S = 0$	$\Delta S = 0$
	$\Delta I_3 = -1/2,\ \lvert\Delta I\rvert = 1/2$	$\Delta I_3 = +1/2,\ \lvert\Delta I\rvert = 1/2$
	Hadronic modes	
$\cos^2\theta_c$	$\Delta S = \Delta C = -1$	$\Delta S = \Delta C = +1$
	$\Delta I_3 = +1,\ \lvert\Delta I\rvert = 1$	$\Delta I_3 = -1,\ \lvert\Delta I\rvert = 1$
$\cos\theta_c \sin\theta_c$	$\Delta S = 0,\ \Delta C = -1$	$\Delta S = 0,\ \Delta C = +1$
	$\Delta I_3 = +1/2,\ \lvert\Delta I\rvert = 1/2, 3/2$	$\Delta I_3 = -1/2,\ \lvert\Delta I\rvert = 1/2, 3/2$
$\sin^2\theta_c$	$\Delta S = +1,\ \Delta C = -1$	$\Delta S = -1,\ \Delta C = +1$
	$\Delta I_3 = 0,\ \lvert\Delta I\rvert = 0, 1$	$\Delta I_3 = 0,\ \lvert\Delta I\rvert = 0, 1$

TABLE 5.4

Charmed Nonstrange Mesons

Name	I (J^P)	Mass (GeV)	Mean life (sec)	Decay mode	Branching fraction
				D^+ (or $D^- \to$ chg. conj.)	
$D^\pm$	$1/2(0^-)$	1.8694 ±0.0006	$(9.2^{+1.7}_{-1.2})\times10^{-13}$	$e^+ X$	(19 ± 4)%
				$K^- X$	(16 ± 4)%
				$\overline{K}^0X+K^0X$	(48 ± 15)%
				$K^+ X$	(6.0 ± 3.3)%
				ηX	(< 13)%
				$\mu^+\nu$	(< 2)%
				$K^-\pi^+\pi^+$	(4.6 ± 1.1)%
				$K^-\pi^+\pi^+\pi^0$	(2.6 ± 3.1)%
				$K^-\pi^+\pi^+\pi^+\pi^-$	(<4)%
				$\overline{K}^0\pi^+$	(1.8 ± 0.5)%
				$\overline{K}^0\pi^+\pi^0$	(13 ± 8)%
				$\overline{K}^0\pi^+\pi^+\pi^-$	(8.4 ± 3.5)%
				$\overline{K}^0K^+$	(.45 ± .30)%
				$K^+K^-\pi^+$	(<0.6)%
				$K^+\pi^+\pi^-$	(<0.23)%
				$\pi^+\pi^0$	(<0.5)%
				$\pi^+\pi^+\pi^-$	(<0.4)%
				$\overline{K}^{*0}\pi^+$	(<3.7)%
				D^0 (or $\overline{D}^0 \to$ chg. conj.)	
D^0 $\overline{D}^0$	$1/2(0^-)$	1.8647 ±0.0006	$(4.4^{+0.8}_{-0.6})\times10^{-13}$	$e^+ X$	(5.3 ± 2.9)%
				$K^- X$	(44 ± 10)%
				$\overline{K}^0X+K^0X$	(33 ± 10)%
				$K^+ X$	(8 ± 3)%
				ηX	(< 13)%
				$K^-\pi^+$	(2.4 ± 0.4)%
				$K^-\pi^+\pi^0$	(9.3 ± 2.8)%
				$K^-\pi^+\pi^+\pi^-$	(4.6 ± 1.4)%
				$K^-\pi^+\pi^0\pi^0$	(seen)
				$\overline{K}^0\pi^0$	(2.2 ± 1.1)%
				$\overline{K}^0\pi^+\pi^-$	(4.2 ± 0.8)%
				$\pi^+\pi^-$	(7.9 ± 3.8)%
				$\pi^+\pi^+\pi^-\pi^-$	(<1.0)%
				K^+K^-	(2.7 ± 0.8)%
				$K^{*-}\pi^+$	(3.4 ± 1.4)%
				$\overline{K}^{*0}\pi^0$	(1.4 ± 1.4)%
				$K^-\rho^+$	(7.2 ± 3.1)%
				$\overline{K}^0\rho^0$	(0.1 ± 0.1)%
				$\overline{K}^{*0}\rho^0$	(0.7 ± 0.7)%
				$K^-\pi^+\rho^0$	(3.9 ± 1.6)%
				$\overline{K}^{*0}\pi^+\pi^-$	(<2.3)%
				$K^-A_2^+$	(<0.8)%

TABLE 5.4 (cont'd)

Charmed Strange Mesons

Name	I (J^P)	Mass (GeV)	Mean life (sec)	Decay mode	Branching fraction
				F^+ (or $F^- \to$ chg. conj.)	
$F^\pm$	$0(0^-)$	1.971 ±0.006	$(1.9^{+1.3}_{-0.7})\times10^{-13}$	$\phi\pi^+$	(seen)%
				$\eta\pi^+$	(poss. seen)%
				$\eta\pi^+\pi^+\pi^-$	(poss. seen)%
				$\eta'\pi^+\pi^+\pi^-$	(poss. seen)%
				$\phi\rho^+$	(poss. seen)%

Nonstrange Charmed Baryons

Name	I (J^P)	Mass (GeV)	Mean life (sec)	Decay mode	Branching fraction
Λ_c^+	$0(1/2^+)$	2.2820 ±0.0031	$(2.3^{+1.0}_{-0.6})\times10^{-13}$	$pK^-\pi^+$	(2.2 ± 1.0)%
				$p\overline{K}^0$	(1.1 ± 0.7)%
				$pK^0\pi^+\pi^-$	(<4, seen)%
				Λ X	(33 ± 29)%
				$\Lambda\pi^+$	(0.6 ± 0.5)%
				$\Lambda\pi^+\pi^+\pi^-$	(<3.1 seen)%
				$\Sigma^0\pi^+$	(seen)%
				pK^{*0}	(.48 ± .30)%
				$\Delta^{++}K^-$	(.45 ± .27)%
				$pK^{*-}\pi^+$	(seen)%
				e^+ X	(4.5 ± 1.7)%
				pe^+ X	(1.8 ± 0.9)%
				Λe^+ X	(1.1 ± 0.8)%
Σ_c^+		2.450		possibly seen in $\Lambda_c\pi$ mode.	

REFERENCES

[5.1] Greenberg O. W., Ann. Rev. Nucl. Part. Sci. 28(1978)327-386.

[5.2] Greenberg O. W., Phys. Rev. Lett. 13(1964)598.

[5.3] Glashow S. L., Nucl. Phys. 22(1964)579,
Weinberg S., Phys. Rev. Lett. 19(1967)1264,
Salam A., Elementary Particle Theory, ed. N. Svartholm (1968)367.

[5.4] Politzer H. D., Phys. Rev. Lett. 26(1973)1346.
Gross D., and F. Wilczek, Phys. Rev. Lett. 26(1973)1343.
Fritzsch H., and M. Gell-Mann, 16th Int. Conf. Proc. on HEP, Chicago IL 1972, Edited by J. D. Jackson and A. Roberts, Vol. 2 p. 135.

[5.5] Bjorken J. D., and S. L. Glashow, Phys. Lett. 11(1964)255.

[5.6] Glashow S. L., J. Iliopoulos, and L. Maiani, Phys. Rev. D2(1970)1285.

[5.7] Carithers W. C., Phys. Rev. Lett. 30(1973)1336.
Fukushima Y., Phys. Rev. Lett. 31(1973)1025.

[5.8] Cabibbo N., Phys. Rev. Lett. 10(1963)531.

[5.9] Gaillard M. K., and B. W. Lee, Phys. Rev. D10(1974)897.

[5.10] Aubert J. J. et al., Phys. Rev. Lett. 33(1974)1404.

[5.11] Augustin J. E. et al., Phys. Rev. Lett. 33(1974)1406.

[5.12] Braunschweig W. et al., Phys. Lett. 57B(1975)407.

[5.13] Whittaker J. R. Phys. Rev. Lett. 37(1976)1596.

[5.14] Scwitters R. F., Proc. of the 1975 Int. Symp. on Lepton and Photon Interactions at High Energy. (Stanford U. 1975) p. 5.

[5.15] Goldhaber G. et al., Phys. Rev. Lett. 37(1976)255,
Peruzzi I. et al., Phys. Rev. Lett. 37(1976)569.

[5.16] Himel T. et al., Phys. Rev. Lett. 45(1980)1146,
Partridge R. et al., Phys. Rev. Lett. 45(1980)1150.

[5.17] Wohl C. G., et al., Rev. Mod. Phys. 56(1984)S1.

[5.18] Bourquin M., and J. M. Gaillard, Phys. Lett. 59B(1975)191.

[5.19] Bourquin M., and J. M. Gaillard, Nucl Phys. B114(1976)334.

[5.20] Combridge B. L., Nucl Phys. B151(1979)429.

[5.21] Buras A. J., and K. J. F. Gaemers, Nucl Phys. B123(1978)249.

[5.22] Giboni K. L., et al., Phys. Lett. 85B(1979)437,

Lockman W., et al., Phys. Lett. 85B(1979)443,

Drijard D., et al., Phys. Lett. 85B(1979)452.

[5.23] Barger V., F. Halzen, and W. Y. Keung, Phys. Rev. D25(1979)112.

[5.24] Odorico R., Phys. Lett. 107B(1981)232.

[5.25] Brodsky S. J., et al., Phys. Lett. 93B(1980)451,

Brodsky S. J., et al., Phys. Rev. D10(1981)2745.

[5.26] Gunion J. F., Phys. Rev. D10(1974)242,

Gunion J. F., Phys. Lett. 88B(1979)150.

[5.27] Horgan R. and M. Jacob, Phys. Lett. 107B(1981)395.

FIGURE CAPTIONS

5.1a,b The two diagrams contributing to the decay of $K_L^0 \to \mu^+\mu^-$.

5.2 "Cuboctahedron" representation of the pseudoscalar ($J^P = 0^-$) mesons .

5.3 Truncated tetrahedron representation of the $J^P = 1/2^+$ baryons.

5.4 Typical fusion and flavor excitation diagrams contributing to heavy flavor production.

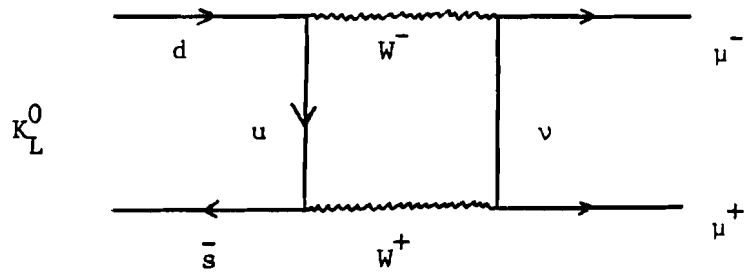

Fig. 5.1a

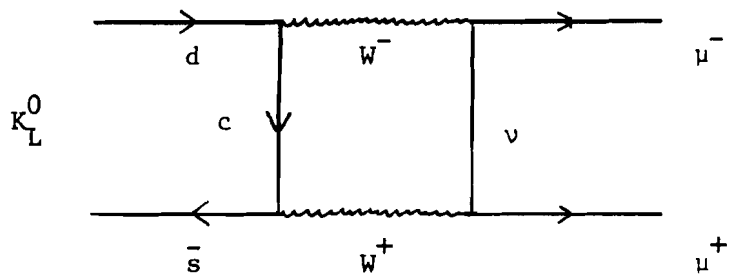

Fig. 5.1b

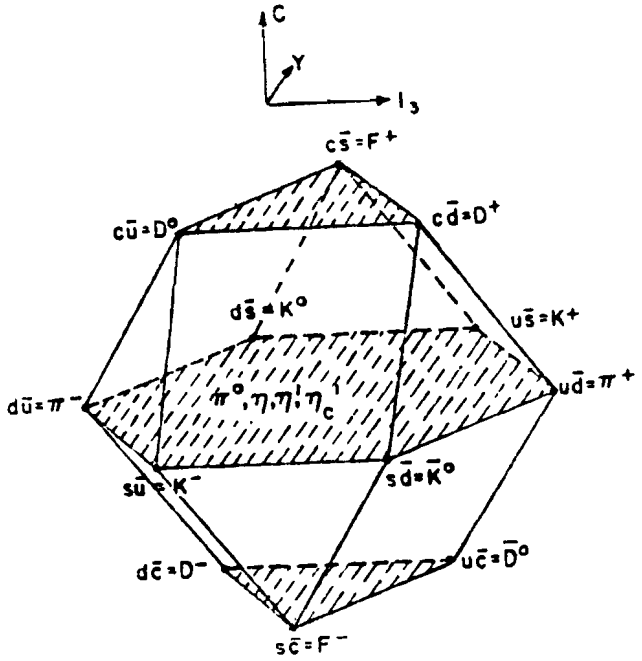
C
Y
I_3
$c\bar{s}=F^+$
$c\bar{u}=D^0$
$c\bar{d}=D^+$
$d\bar{s}=K^0$
$u\bar{s}=K^+$
$d\bar{u}=\pi^-$
π^0,η,η',η_c
$u\bar{d}=\pi^+$
$s\bar{u}=K^-$
$s\bar{d}=\bar{K}^0$
$d\bar{c}=D^-$
$u\bar{c}=\bar{D}^0$
$s\bar{c}=F^-$

Fig. 5.2

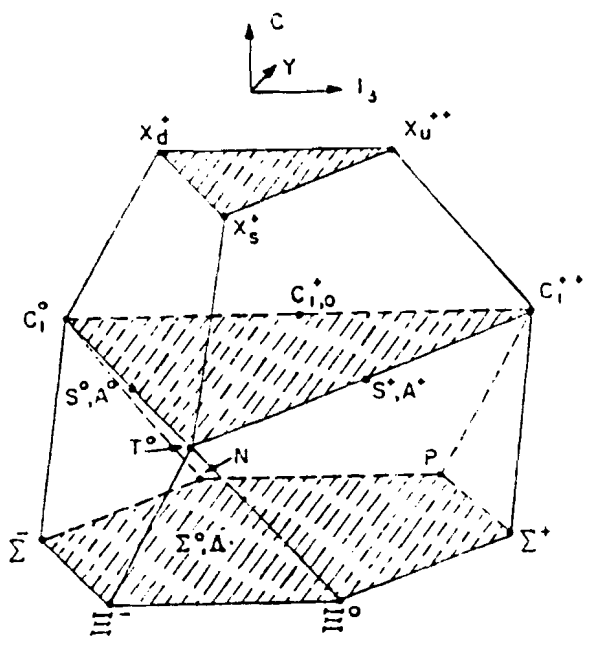
C
Y
I_3
X_d^+
X_u^{++}
X_s^+
$C_{1,0}^+$
C_1^0
C_1^{++}
S^0,A^0
S^+,A^+
T^0
N
P
Σ^-
Σ^0,Λ
Σ^+
Ξ^-
Ξ^0

Fig. 5.3

FUSION

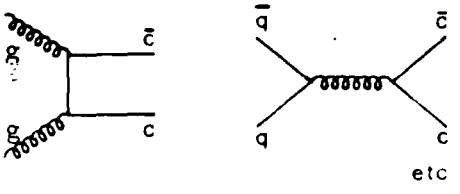

EXCITATION

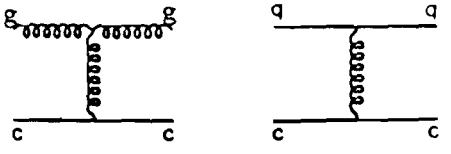

Fig. 5.4

CHAPTER 6

STUDY OF THE $\phi\pi^{\pm}$ FINAL STATE

The final state $\phi\pi^{\pm}$ is particularly interesting in searches for new objects, because the $\phi\pi$ decay is an OZI violating process[6.1] for any meson constructed from a quark-antiquark pair[6.2]. The OZI rule forbids processes in which a quark from one meson annihilates with an antiquark from another meson, or the equivalent pair production. Thus resonances in the $\phi\pi$ final state can indicate three things, (a) a new object like a four quark state [6.3], (b) an OZI-violating decay of a conventional meson, and (c) a weak decay into a system containing a strange quark-antiquark pair. In particular the decay of the F meson is expected to have a substantial branching fraction to the Cabibbo-allowed $\phi\pi^{\pm}$ final state [6.4]. Recently this mode has been reported [6.5] and confirmed [6.6] in e^+e^- collisions with a mass of 1970 ± 5 MeV and a branching fraction of about 4.4% [6.5].

6.1 Data Selection

As described in section 3.7 we ended up, after pattern recognition, kinematic fitting, and particle identification with 120,000 events containing at least $2K^+$ and $2K^-$. The analysis that follows is based on this sample of events only. The following cuts were applied on the DST on the basis of improving the signal to noise ratio:

(a) Only tracks that made it through the fitting routines were used.

(b) Since our magnet had only a small bend in the y-z view there were tracks that shared the same track points in this view. We called these duplicates, and a special procedure was used to resolve the ambiguity. If the opening angle in the y-z view of two tracks was less than 0.3 mrad the tracks were defined as

duplicates and only one was chosen according to the total number of hits in the track.

(c) A vertex cut was applied: If the reconstructed vertex was not within the following limits the event was thrown out. The limits are within 3σ from the edges of the known target x, y, and z position(cm):

$$-1.87 < x < 1.17$$
$$-1.52 < y < 1.52$$
$$-170.00 < z < -130.00$$

(d) Kaons below 5.8 GeV/c momentum are renamed as pions.

For the analysis we called kaons all particles with ID = 2 and pions all particles with ID = 1,4,5 (see section 4.2 for definitions of ID's). This choice was basically made from the fact that ID's 6,7,8 (ID = 3 are protons) are basically bad decisions from the Cherenkov algorithm and only add to the background without improving the signal to noise in both the ϕ and the $K^*(890)$ signals.

6.2 Observation of the Cabibbo-Suppressed decay $D^\pm \to \phi\pi^\pm$

The mass spectrum of all K^+K^- pairs found in the 120,000 events of the type $pN \to K^+K^-K^+K^-X$ is shown in Fig. 6.1. To fit the data we used the sum of an integrated Gaussian with mean, sigma, and normalization free to vary, with a background function. The integrated Gaussian is of the form,

$\frac{N}{\sqrt{\pi}} \left[\mathrm{erf}\left(\frac{b - \bar{x}}{\sqrt{2}\,\sigma}\right) - \mathrm{erf}\left(\frac{a - \bar{x}}{\sqrt{2}\,\sigma}\right) \right]$ where $\mathrm{erf}\,(y) = \int_0^y e^{-u^2}\,du$, and the background function is given by the form $A(x-B)^C \times e^{-D(x-B)}$,where A,B,C,D, are free to vary, N is the number of events under the peak, $\bar{x}$ is the mean of the Gaussian giving the mass of the resonance, σ is the width from which the FWHM is calculated as $2.36 \times \sigma$, and a (b) are the lower (upper) limits of each bin. A summary of the parameters from all the fits that follow can be found in Table 6.1. The fit gives a mass of 1.0199 ± 0.0003 GeV/c^2, and a width of 0.0074

± 0.0004 GeV/c^2 (FWHM). These results are consistent with the accepted values [6.7] given our resolution of 0.006 GeV/c^2 (FWHM) at the ϕ mass determined using Monte Carlo techniques. The fit gives 2012 ± 97 ϕK^+K^- events. The χ^2/DF for this fit is 50/48. The ϕ signal serves as a calibration point for the mass scale.

We define as ϕ candidates the K^+K^- mass combinations within ± 0.006 GeV/c^2 of the nominal ϕ mass. Invariant mass combinations are then made with π's from the same event. The resulting $\phi\pi^\pm$ mass distribution is shown in Fig. 6.2a. A clear enhancement is seen near the D mass while nothing is seen at the F mass. A fit with a third order polynomial of the form $A + Bx + Cx^2 + Dx^3$, with A, B, C, and D free to vary plus a Gaussian of the same form as before gives a mass of 1.8654 ± 0.0087 GeV/c^2 and a width of 0.053 ± 0.018 GeV/c^2 (FWHM), with a χ^2/DF of 41/44. The width is consistent with our experimental resolution of 0.052 GeV/c^2 as determined by a Monte Carlo simulation of events which were propagated through the experimental apparatus and passed through the track reconstruction and fitting programs. The fit gives a 5.4 standard deviation excess of 234 ± 43 events above background. Using the ϕ we can set an upper limit on our mass scale error of ± 0.02 GeV/c^2 at the D mass. Hence, this enhancement can not be the F meson. We should note here that the π's in this $\phi\pi^\pm$ mass spectrum belong to three distinct momentum regions, specified by thresholds in the Cherenkov counter. If we plot separately the $\phi\pi^\pm$ mass spectra with π's from these different regions then the enhancement observed in Fig. 2a is present in all three regions. In Fig. 6.2b the $\phi\pi^\pm$ background mass spectrum is shown, where the "ϕ" candidates are K^+K^- pairs with invariant mass just below or just above the ϕ mass, yielding roughly the same number of combinations as in Fig 6.2a. No apparent signal is observed. The smooth curve has a χ^2/DF equal to 31/47. The MARK III group [6.8] has recently reported in e^+e^- collisions the $D^\pm \to \phi\pi^\pm$ mode and has measured the ratio of the branching fractions of $D^\pm \to \phi\pi^\pm$ to $D^\pm \to$

$K^+K^-\pi^\pm$ to be 1.15 ± 0.65. No evidence for a signal is observed in our $K^+K^-\pi^\pm$ mass spectrum mainly due to an increase in our background levels by a factor of 23 from $\phi\pi$ to $KK\pi$.

Further evidence that this enhancement is the $D^\pm$ meson comes from the separately fitted yields of $\phi\pi^+$ and $\phi\pi^-$ (Fig. 6.2c). One finds that the D^+/D^- ratio is 0.91 ± 0.16, consistent with unity as expected if valence quarks did not play a role in the production. In Fig. 6.3 the $\phi\pi^\pm$ spectrum is shown for events with $p_T(\phi\pi\pm) > 0.5$ GeV/c where the mass and width are fixed at the best fit values from Fig. 6.2a. The improved signal/noise ratio (6.7 standard deviations) with respect to Fig. 2a implies that this enhancement is produced with large p_T compared to uncorrelated $\phi\pi$ background, as expected of charm. In Fig. 6.4 the $K^\pm\pi^\mp$ mass spectrum is shown for events of the type $pN \rightarrow (\phi\pi)(K\pi)KX$ where the $\phi\pi^\pm$ mass combination is in the D region (Fig. 4a) and outside the D region (Fig. 4b). The D region is defined to be the $\phi\pi^\pm$ mass combination within ± 0.040 Gev/c^2 of the fitted $D^\pm$ mass. A fit with a Breit-Wigner plus an exponential for background gives 172 ± 25 $K^*(890)$ events. The χ^2/DF for Fig. 4a is 50/43. For Fig. 4b an exponential was used and the χ^2/DF is 57/46. Thus we observe a greatly enhanced production of $K^*(890)$ associated with the $D^\pm$ as one might expect from charm pair production. Separate fits were made to the $K^\pm\pi^\mp$ distributions for events containing $D^+ \rightarrow \phi\pi^+$ (104 ± 19 K^*'s) and those with $D^- \rightarrow \phi\pi^-$ (59 ± 19 K^*'s). This difference in associated $K^*(890)$ production might be expected if the K^*'s arise from fragmentation of the anti-charm (charm) quark produced together with the $D^+(D^-)$, and if proton valence quarks play a significant role. For example, a leading Λ_c^+ (cud) would be produced together with a central $D^-(\bar{c}d)$ or $D^0(cu)$ but not with a central $D^+(c\bar{d})$. A leading D^- or $\overline{D^0}$ containing a proton valence quark would be accompanied by a central D^+. The fragmentation of a Λ_c^+ is less likely to yield a K^{*0} or a $\overline{K^{*0}}$ than the

fragmentation of a leading meson containing a $\bar{c}$ quark. Thus we have an indication that leading Λ_c^+ may be produced in association with the D^- we observe. We also looked for $K^*(890)$ production in events of the type $pN \to \phi\pi^\pm(K^\mp\pi^\pm)K^\pm X$ as compared with events of the type $pN \to \phi\pi^\pm(K^\pm\pi^\mp)K^\mp X$, where the $\phi\pi^\pm$ mass falls in the D region. We separately fitted each $K\pi$ mass spectrum using a Breit-Wigner plus an exponential for background. The results were the following: For $D^+ \to \phi\pi^+$ we obtained 53 ± 19 $K^* \to K^+\pi^-$ and 76 ± 14 $\overline{K^*} \to K^-\pi^+$. For $D^- \to \phi\pi^-$ we obtained 23 ± 16 $K^* \to K^+\pi^-$ and 18 ± 14 $\overline{K^*} \to K^-\pi^+$.

We have examined the angular distributions of the decay products from the above enhancement to see whether they are consistent with the decay characteristics of a spin 0 object (D) going to a spin 1 (ϕ) and a spin 0 (π). For a detailed definition of these angles see Appendix A. There are two independent angular distributions to be checked. First, the angular distribution of the ϕ in the $\phi\pi$ rest frame, $\cos\theta_\phi$, should be isotropic. Second, since the helicity of the ϕ in the $\phi\pi$ rest frame must be zero, the angular distribution of the K^+ with respect to the ϕ direction should be $\cos^2\theta_K$. The $\phi\pi^\pm$ spectra in various angular distributions were fitted by the sum of a polynomial and a Gaussian centered at 1.8654 GeV/c^2 with a fixed width of 0.053 GeV/c^2. The number of events in each Gaussian peak is plotted in Fig 6.5 vs. $\cos\theta_\phi$ and $\cos\theta_K$ together with the expected distributions as modified by experimental acceptance and trigger bias using Monte Carlo events. The angular distributions of the signal are consistent with those expected for a spin 0 object. However if the object is produced unpolarized with spin 1 we would also get an isotropic distribution for $\cos\theta_\phi$. The distribution of the K^+ however, has a more complicated dependence on the azimuthal angle and is proportional to,

$$\sin^2\theta_K \cos^2\theta_K \cos(2\phi_K)$$

where ϕK is defined in Fig. A.1. Thus we cannot exclude a higher spin assignment.

6.3 Cross Section Estimates

The $D^{\pm} \rightarrow \phi\pi^{\pm}$ enhancement is observed in events with at least $2K^{+}$ and $2K^{-}$. From $D\bar{D}$ production we would expect only 3 charged kaons. Thus, the role of the additional $K^{\pm}$ required by our trigger processor is unclear and it is difficult to reliably estimate the product of the production cross section and the branching fraction, since our geometric acceptance and trigger efficiency are strongly dependent on the model used to generate the 4th kaon, giving acceptance correction factors up to an order of magnitude different. However, for the charm and strangeness conserving process $pN \rightarrow DFKX$ one knows the decay branching fractions $D \rightarrow KX$[6.7], and $F^{\pm} \rightarrow \phi\pi^{\pm}$[6.5]. Hence, given our failure to observe the F meson we can set an upper limit on the cross section for F production. To set a 90% confidence level upper limit on a cross section we define a mass interval $\Delta m \approx 5\sigma$ where σ is the Gaussian-σ from the predicted mass resolution. From Monte carlo determinations the mass resolution at the F mass was determined to be 52 MeV/c^2. Thus σ = 22 MeV/c^2 and Δm = 110 MeV/c^2. If we call n the number of observed events in Δm, and $\bar{b}$ the number of events as calculated from a background fit with no resonance added in the same Δm region, then the number of expected events if there was no F is given by,

$$\bar{s} = n + 1.3\sqrt{n} - \bar{b} \ .$$

Using Fig. 6.2a these numbers are calculated to be, n = 1781 ± 43 and $\bar{b}$ = 1764 ± 42 . Thus $\bar{s}$ = 72 ± 59 events.

Due to experimental acceptance we are limited to a very small range in x_F, namely $|x_F| < 0.1$. We generated Monte Carlo events of the type $pN \rightarrow DFKX$ with

a flat x_F distribution and a p_T^2 dependence of the form $\exp(-1.1p_T^2)$. The x_F range used was between -0.01 and 0.01. We would like to calculate the differential cross section at $x_F = 0$. We generated 50,000 events of the type described above 158 of which survived through the acceptance cuts. Using the formulas from section 2.7 we calculate that,

$$\int_{-0.01}^{0.01} \frac{d\sigma}{dx_F} dx_F \cdot B = \frac{72 \pm 59}{800} \times \frac{50000 \pm 222}{158 \pm 12} \times 1.61 = 46 \pm 33 \text{ nb},$$

where B, the branching fraction of $F \to \phi\pi$ is about 4.4%[6.5]. Assuming that $\frac{d\sigma}{dx_F} = \alpha (1 - x_F)^n$ then $\left.\frac{d\sigma}{dx_F}\right|_{x_F=0} = \alpha$. Substituting all this into the above equation and solving for α we get,

$$\left.\frac{d\sigma}{dx_F}\right|_{x_F=0} = \left[\int_{-0.01}^{0.01} \frac{d\sigma}{dx_F} dx_F \cdot B \right] \times \left[\frac{n+1}{1-(0.99)^n} \right] \times \frac{1}{2B}$$

If we assume a $F^{\pm}$ cross section dependence of:

$\frac{d^2\sigma}{dx_F dp_T^2} \propto (1-|x_F|)^n e^{-1.1p_T^2}$, with n=7 as predicted by QCD counting rules [6.9], and a p_T^2 behavior as found by LEBC [6.10] and ACCMOR [6.11] then the 90% confidence level upper limit of the differential cross section for F production, $\left.\frac{d\sigma(F)}{dx_F}\right|_{x_F=0} = 55 \pm 37$ μb. corrected for acceptance and detection efficiency. This limit can be compared to the ISR data on D^0 production[6.12] where $\left.\frac{d\sigma(D^0)}{dx_F}\right|_{x_F=0} = 700 \pm 300$ μb. The upper limit then on the cross section for hadronic production of $F^{\pm}$ is $\sigma(F) < \left(\frac{2}{n+1}\right) \left.\frac{d\sigma(F)}{dx_F}\right|_{x_F=0} = 13 \pm 9$ μb per nucleon for pN interactions at 400 GeV/c using n=7 as QCD counting rules predict. In Table 2.2 the differential and total cross section upper limits are presented for various values of n. We should note that this is rather model dependent since our acceptance depends strongly on the model to generate the final state DFKX.

6.4 Summary

We have found an enhancement in the $\phi\pi^{\pm}$ final state which is consistent with the mass, spin, and width of the charm $D^{\pm}$. Its production is central, charge symmetric, with high p_T, and consistent with charm pair production. Recently, hadronic production of both the D and the F followed by decay into $\phi\pi^{\pm}$ has been reported in 200 GeV/c π^-N interactions at $x_F > 0.11$[6.13]. In that experiment the cross section times branching fraction (σ.B) is comparable for the Cabibbo-favored F and the Cabibbo-suppressed D. By comparison at $x_F = 0.$ in 400 GeV/c pN interactions we see no indication of $F^{\pm}$ decays with respect to the observed $D^{\pm}$ decays.

TABLE 6.1

Parameters for the fits used in the analysis

Functions used:

(1) $\frac{N}{\sqrt{\pi}} \left[\operatorname{erf}\left(\frac{b - \bar{x}}{\sqrt{2}\,\sigma}\right) - \operatorname{erf}\left(\frac{a - \bar{x}}{\sqrt{2}\,\sigma}\right) \right]$ with $\operatorname{erf}(y) \equiv \int_0^y e^{-u^2}\,du$,

(2) $A(x-B)^C \times e^{-D(x-B)}$,

(3) $A' + B'x + C'x^2 + D'x^3$,

(4) $\frac{N}{\sqrt{\pi}} \left[\tan^{-1}\left(\frac{2(b - \bar{x})}{W}\right) - \tan^{-1}\left(\frac{2(a - \bar{x})}{W}\right) \right]$,

(5) $\alpha \times e^{-\beta(x-\gamma)^\delta}$

Fig. 6.1	Fig. 6.2a	Fig. 6.2 b
Function: 1 + 2	Function: 1 + 3	Function: 3
$N = 2012.0 \pm 97.0$	$N = 232 \pm 43$	
$\bar{x} = 1.0199 \pm 0.0003$	$\bar{x} = 1.8654 \pm 0.0087$	
$\sigma = 0.0031 \pm 0.0003$	$\sigma = 0.0226 \pm 0.0076$	
$A = 2295.7 \pm 15.1$	$A' = 2295.7 \pm 1.3$	$A' = 2358.1 \pm 23.4$
$B = 0.7608 \pm 0.0023$	$B' = -1290.6 \pm 0.4$	$B' = -1309.9 \pm 10.3$
$C = 19.6 \pm 1.4$	$C' = 79.5 \pm 0.2$	$C' = 72.9 \pm 1.5$
$D = 0.9818 \pm 0.0004$	$D' = 72.5 \pm 0.4$	$D' = 72.4 \pm 0.5$

TABLE 6.1 (cont'd)

Fig. 6.2c		Fig. 6.3
Function: 1 + 3		Function: 1 + 3
$\phi\pi^+$	$\phi\pi^-$	
N = 118 ±16	N = 129 ±19	N = 180 ± 36
$\bar{x}$ = 1.8654	$\bar{x}$ = 1.8654	$\bar{x}$ = 1.8654
σ = 0.0226	σ = 0.0226	σ = 0.0226
A'= 798.9 ±16.0	A'=1024.6 ±60.4	A'= 851.6 ± 12.9
B'=-239.6 ±6.4	B'=-571.6 ±50.4	B'=-352.3 ± 3.6
C'=-51.2 ±0.9	C'= 6.4 ±0.5	C'=-5.1 ± 6.4
D'= 20.4 ±0.2	D'= 45.2 ±4.2	D'= 18.7 ± 0.2

Fig. 6.4

Function: 4 + 5

(a)	(b)
N = 172 ±25	
$\bar{x}$ = 0.921 ±0.029	
W = 0.088 ±0.023	
α = 712.6 ±88.0	α = 732.2 ±40.0
β = 2.51 ±0.02	β = 2.5 ±0.02
γ = 0.62 ±0.01	γ = 0.55 ±0.03
δ = 0.55 ±0.01	δ = 0.71 ±0.06

TABLE 6.2

90% confidence level upper limits on differential and total cross sections for F production.

n	$\left.\frac{d\sigma}{dx_F}\right\|_{x_F=0}$ (μb)	σ (μb)
1	104 ± 75	104 ± 75
2	78 ± 56	52 ± 37
3	70 ± 50	35 ± 25
4	66 ± 47	26 ± 19
5	61 ± 43	20 ± 14
6	58 ± 41	16 ± 11
7	55 ± 37	13 ± 9
8	53 ± 36	12 ± 9

REFERENCES

[6.1] Okubo S., Phys. Lett. 5(1963)165,
Zweig G., CERN report, TH-401 and 412 (unpublished),
Iizuka J., Suppl. Prog. Theor. Phys. 37(1966)21.

[6.2] Lipkin H. J., Experimental Meson Spectroscopy 1977,
Northeastern U. Press, Boston, 1977 p. 388.

[6.3] Close F. E., and H. J. Lipkin, Phys.Rev.Lett. 41(1978)1263.

[6.4] Quigg C., and J. L. Rosner, Phys.Rev. D17(1978)239.

[6.5] CLEO Collab., A. Chen et al., Phys.Rev.Lett. 51(1983)634.

[6.6] TASSO Collab., M. Althoff et al., Phys.Lett. 136B(1984)130.
ARGUS Collab., to be published in the proceedings of the
XIXth Rencontre de Moriond (February-March,1984).

[6.7] Wohl C. G., et al., Rev. Mod. Phys. 56(1984)S1.

[6.8] Mark III Collab., to be published in the proceedings of the APS
Division of Particles and Fields meeting in Santa-Fe NM,
(October-November,1984).

[6.9] Gunion J. F., Phys.Lett. 88B(1979)150.

[6.10] LEBC EHS Collab., M. Aguilar-Benitez et al., Phys.Lett. 123B(1983)98.

[6.11] ACCMOR Collab., R. Bailey et al., Phys.Lett. 132B(1982)230.

[6.12] DiBitonto D., Proton-Antiproton Collider Physics-1981, AIP Conference
Proceedings No. 85, p26.

[6.13] ACCMOR Collab., R. Bailey et al., Phys.Lett. 139B(1984)320.

FIGURE CAPTIONS

6.1 K^+K^- invariant mass distribution from events containing at least $2K^+$ and $2K^-$. The curve is described in the text.

6.2 $\phi\pi^\pm$ invariant mass distribution where the (a) ϕ band is chosen to be between 1.014 and 1.026 Gev/c^2 and (b) "ϕ" candidates are K^+K^- pairs chosen just outside the ϕ mass band. (c) Separately fitted $\phi\pi^+$ and $\phi\pi^-$ invariant mass spectra.

6.3 $\phi\pi^\pm$ invariant mass distribution for $p_T(\phi\pi^\pm) > 0.5$ GeV/c.

6.4 $K^\pm\pi^\mp$ invariant mass distributions from events of the type $pN \rightarrow (\phi\pi)(K\pi)KX$ where the (a) $\phi\pi^\pm$ mass is chosen to be in the D region and (b) outside the D region.

6.5 Measured angular distributions for signal compared with those expected for a spin 0 object decaying to a ϕ and a π. (a) $\cos\theta_\phi$; (b) $\cos\theta_K$. The details can be found in the text.

Fig. 6.1

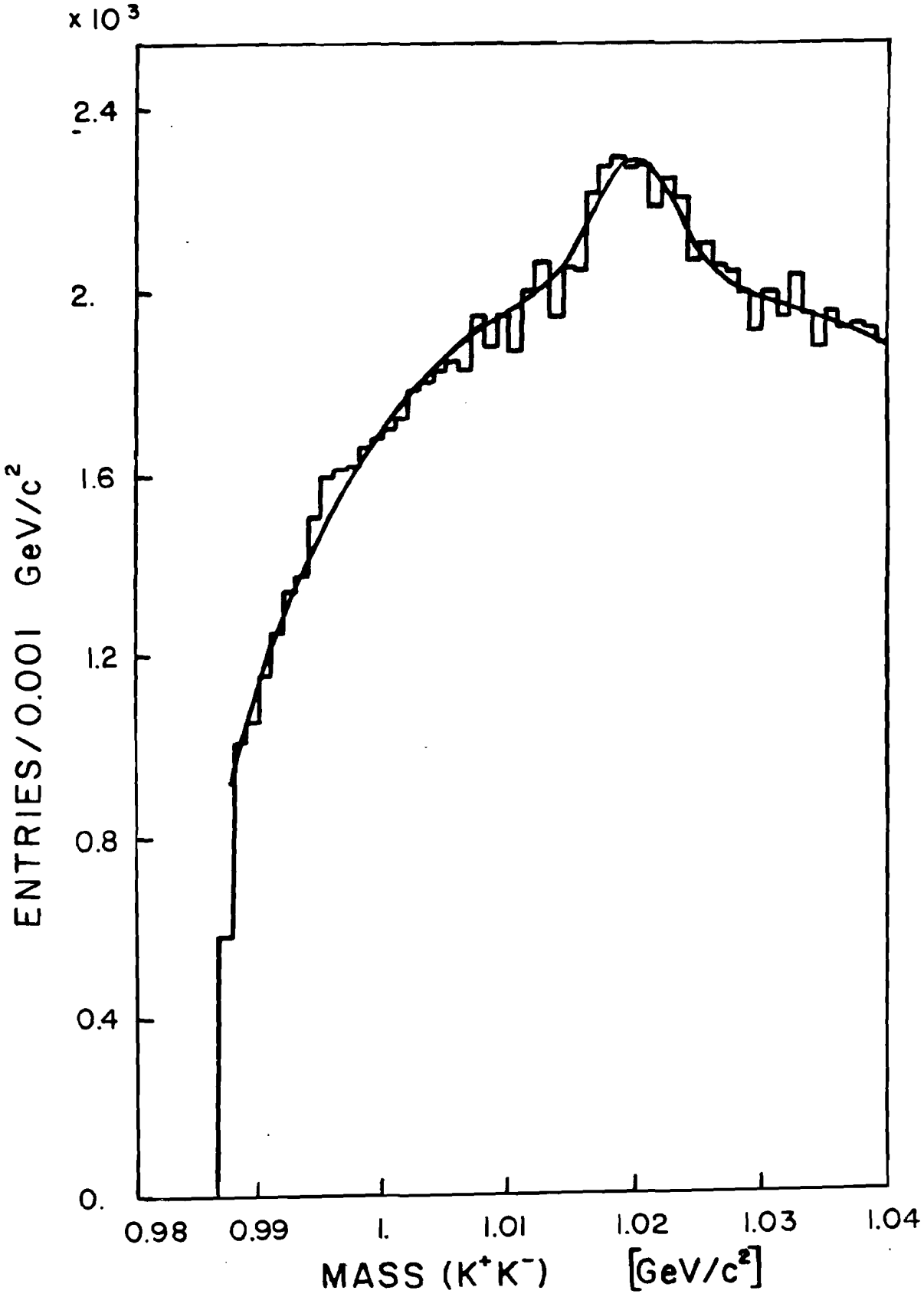
x 10³
2.4
2.
1.6
1.2
0.8
0.4
0.
ENTRIES/0.001 GeV/c²
0.98
0.99
1.
1.01
1.02
1.03
1.04
MASS (K⁺K⁻) [GeV/c²]

Fig. 6.2a

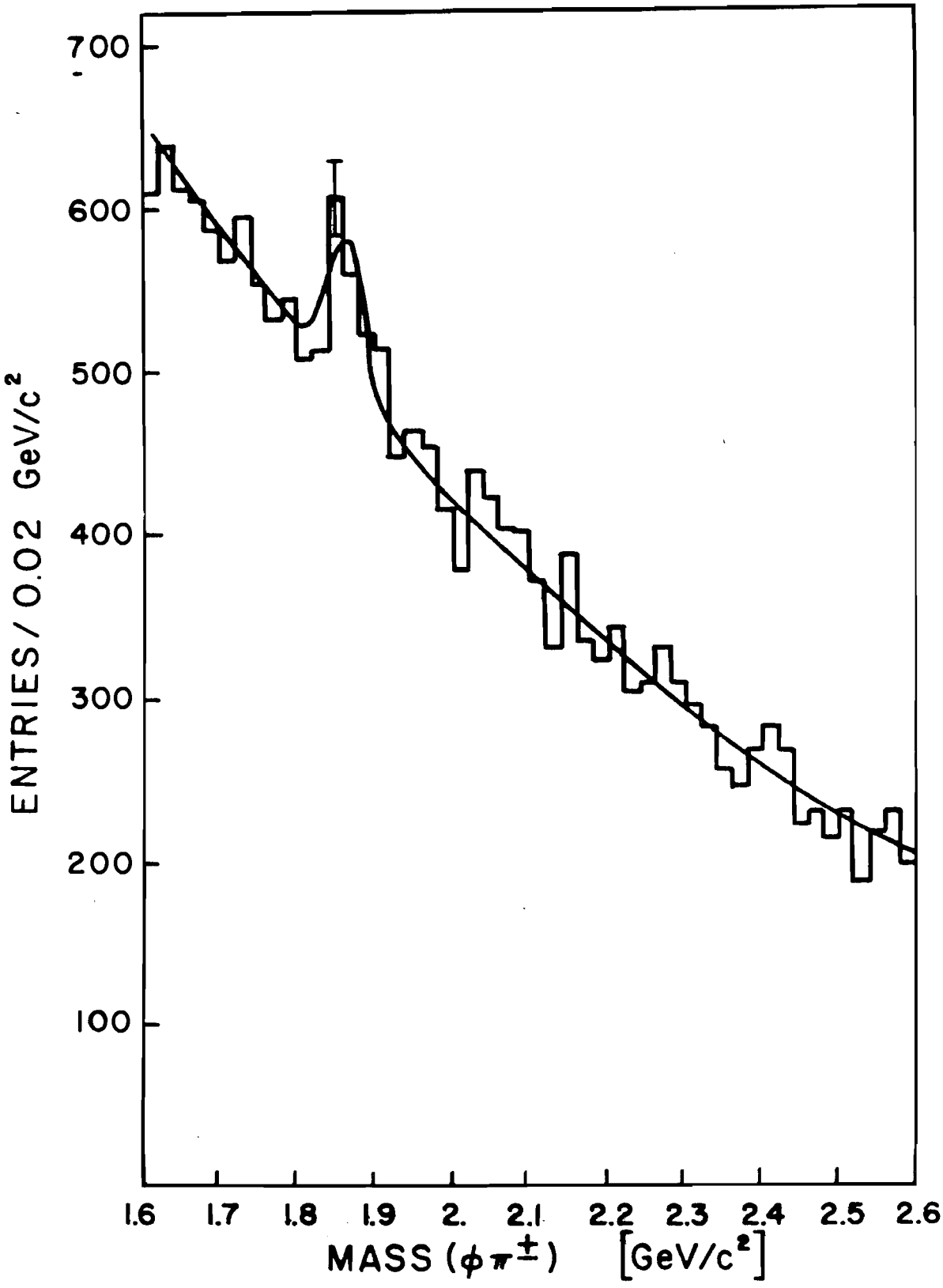
700
600
500
400
300
200
100
ENTRIES / 0.02 GeV/c²
1.6
1.7
1.8
1.9
2.
2.1
2.2
2.3
2.4
2.5
2.6
MASS (φπ±) [GeV/c²]

Fig. 6.2b

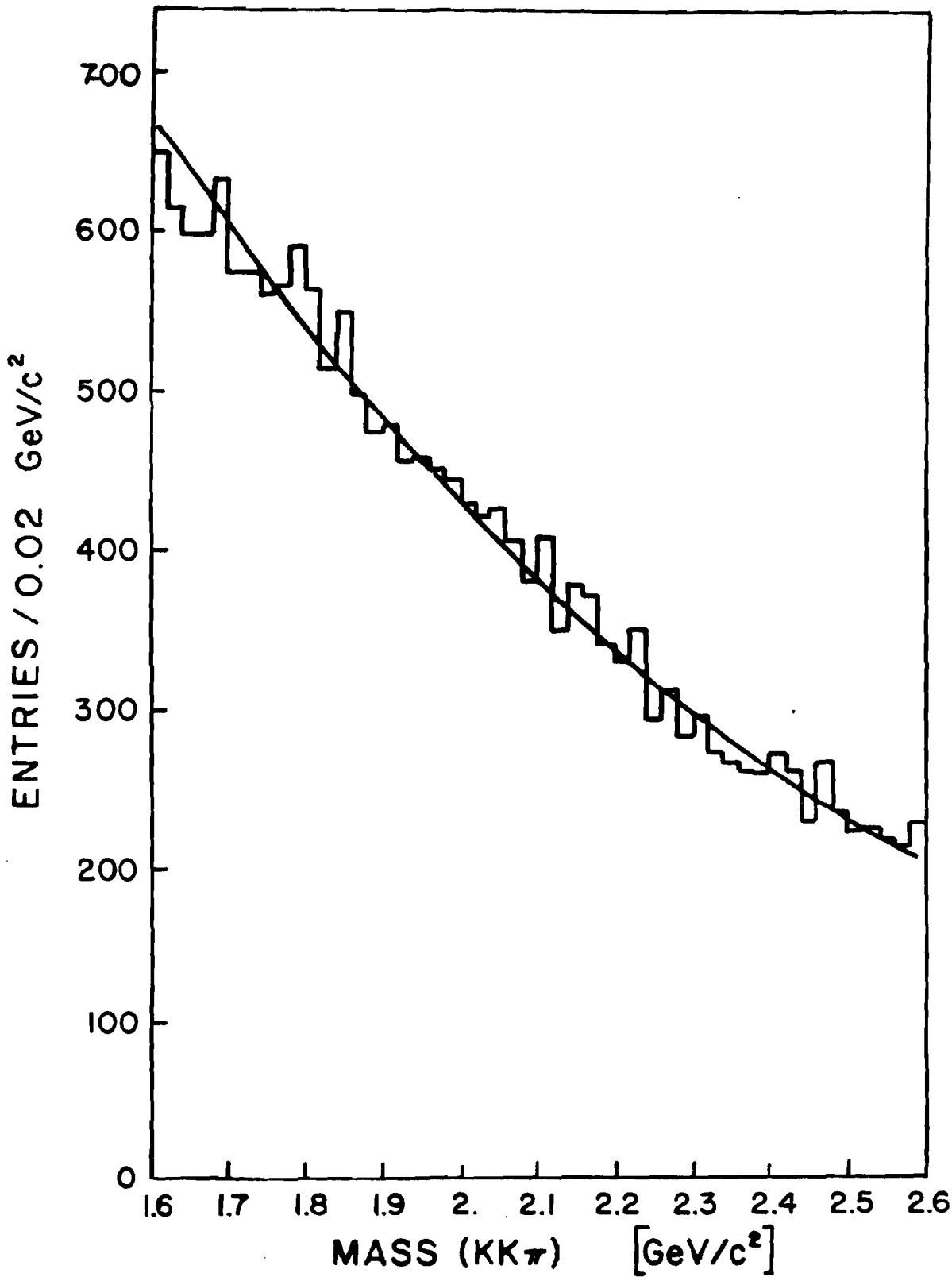
700
600
500
400
300
200
100
0
ENTRIES / 0.02 GeV/c²
1.6
1.7
1.8
1.9
2.
2.1
2.2
2.3
2.4
2.5
2.6
MASS (KKπ) [GeV/c²]

Fig. 6.2c

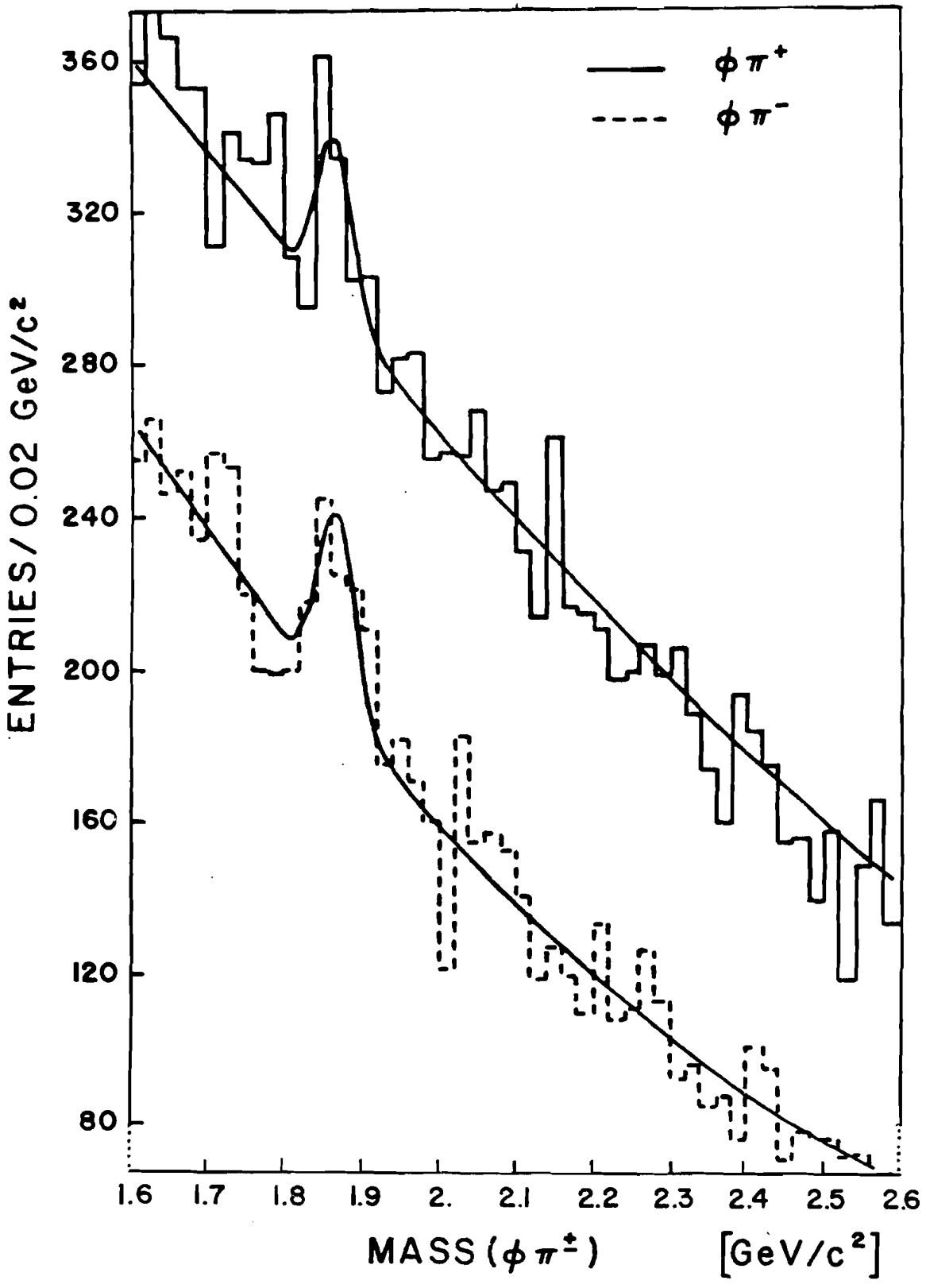
$\phi\pi^+$
$\phi\pi^-$
360
320
280
240
200
160
120
80
ENTRIES/0.02 GeV/c²
1.6
1.7
1.8
1.9
2.
2.1
2.2
2.3
2.4
2.5
2.6
MASS ($\phi\pi^\pm$) [GeV/c²]

Fig. 6.3

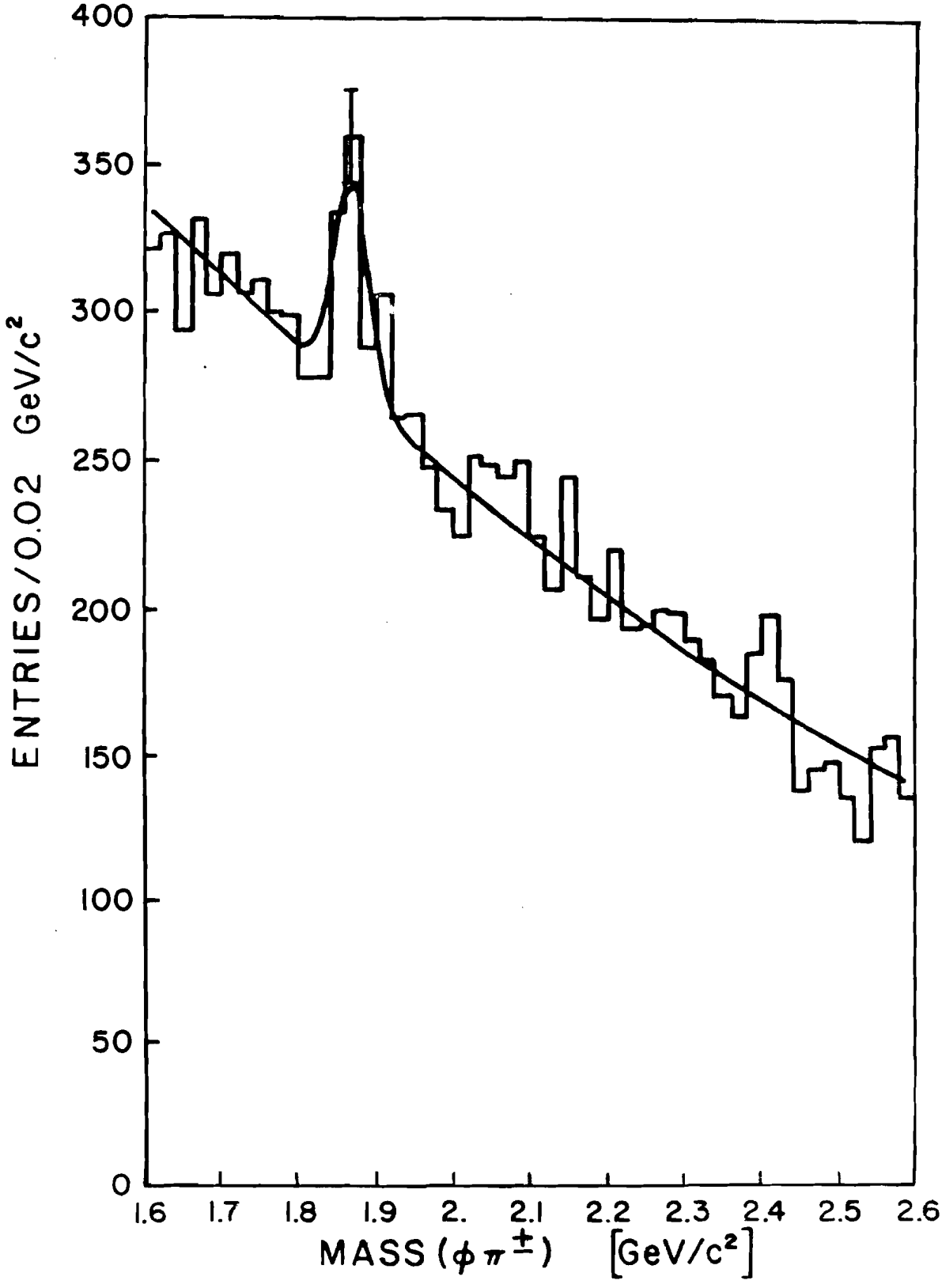
400
350
300
250
200
150
100
50
0
ENTRIES/0.02 GeV/c²
1.6
1.7
1.8
1.9
2.
2.1
2.2
2.3
2.4
2.5
2.6
MASS (φ π±) [GeV/c²]

Fig. 6.4

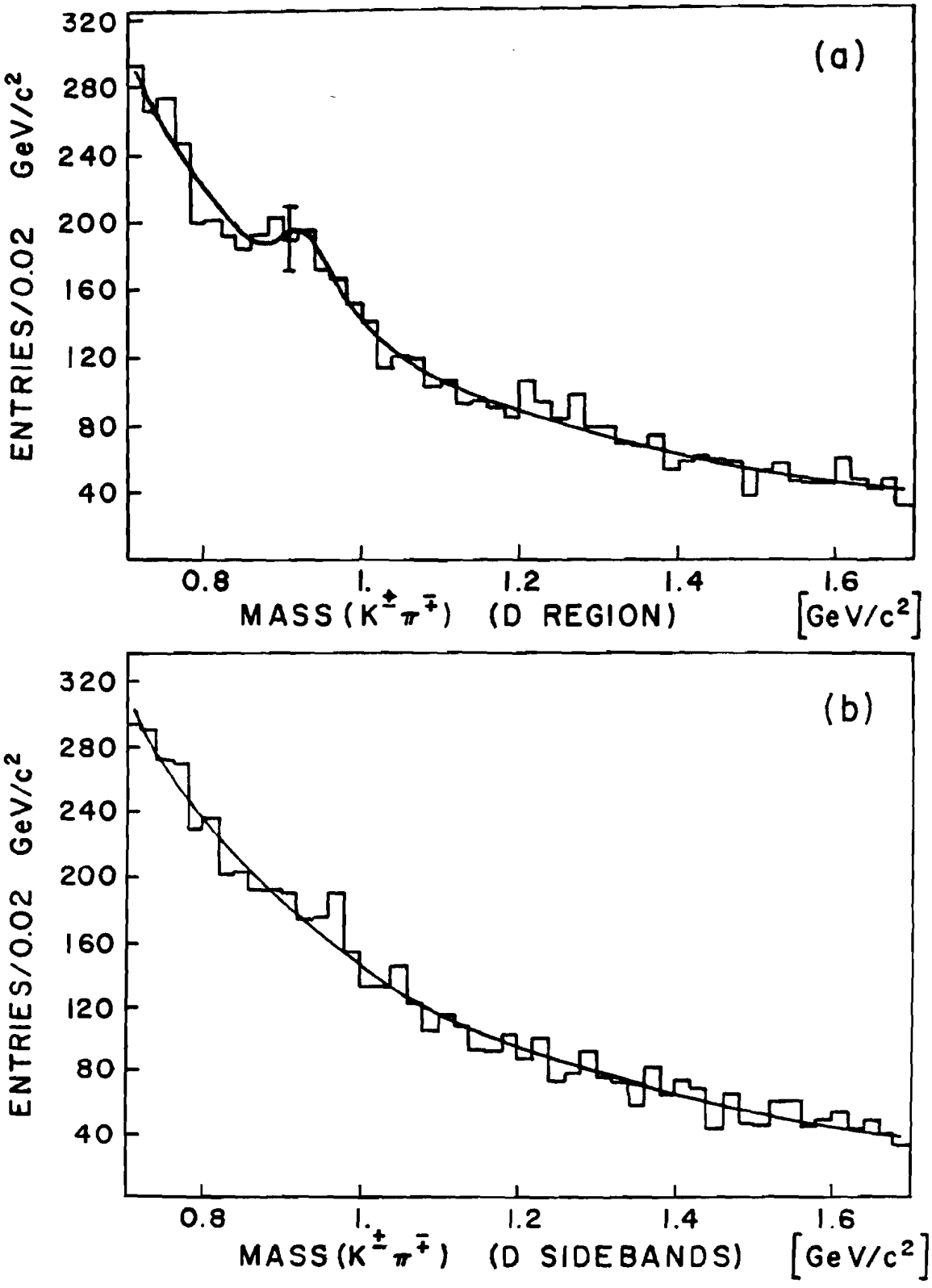
(a)
ENTRIES/0.02 GeV/c²
320
280
240
200
160
120
80
40
0.8
1.
1.2
1.4
1.6
MASS (K±π∓) (D REGION) [GeV/c²]
(b)
ENTRIES/0.02 GeV/c²
320
280
240
200
160
120
80
40
0.8
1.
1.2
1.4
1.6
MASS (K±π∓) (D SIDEBANDS) [GeV/c²]

Fig. 6.5a

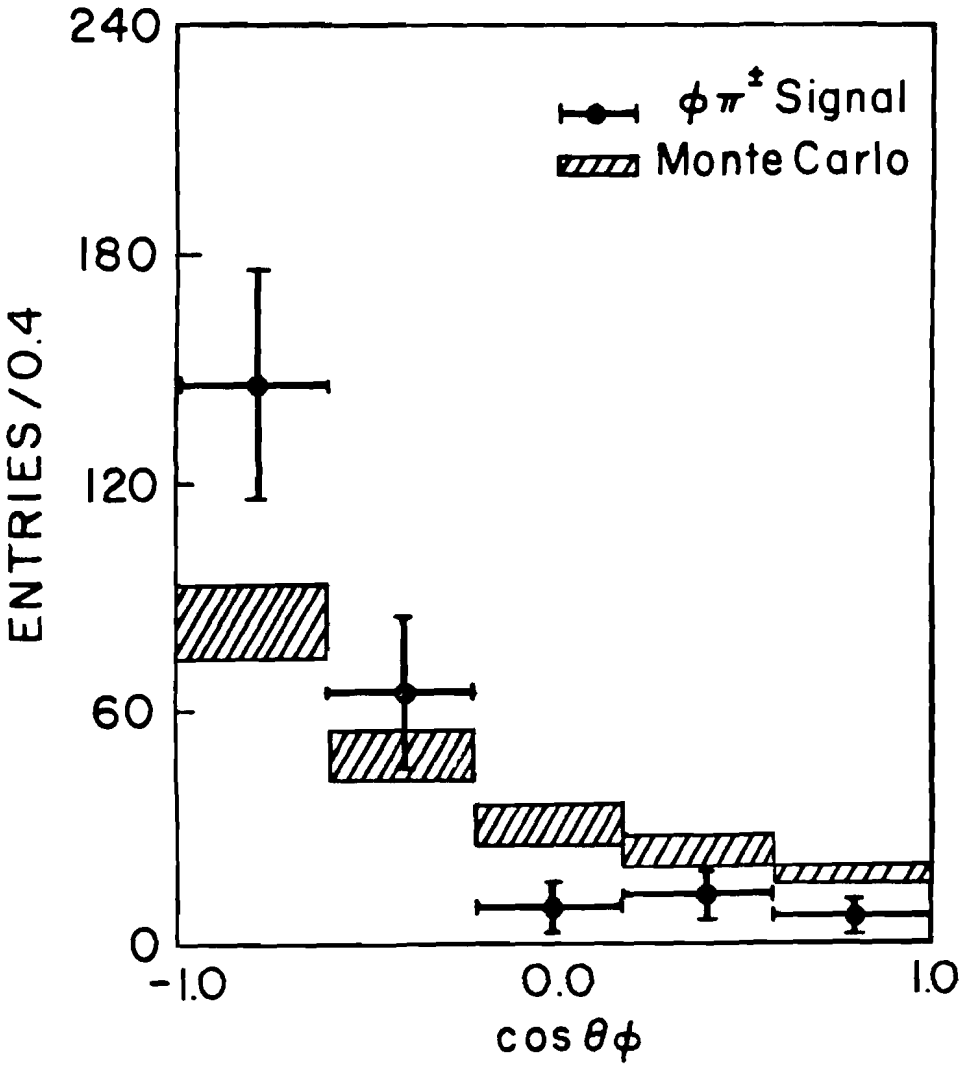
240
180
120
60
0
ENTRIES/0.4
$\phi\pi^{\pm}$ Signal
Monte Carlo
-1.0
0.0
1.0
$\cos\theta_\phi$

Fig. 6.5b

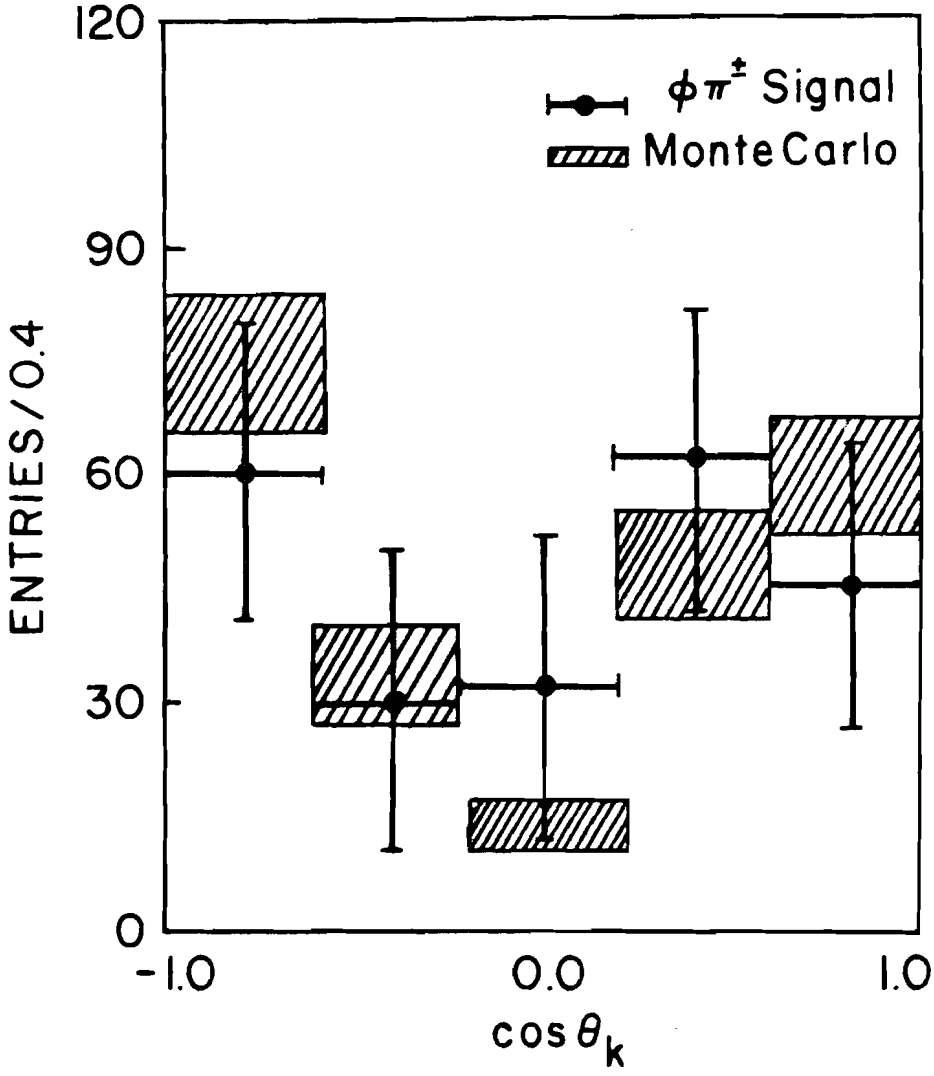
120
90
60
30
0
ENTRIES/0.4
$\phi\pi^{\pm}$ Signal
Monte Carlo
-1.0
0.0
1.0
$\cos\theta_k$

APPENDIX A

ANGULAR DISTRIBUTIONS OF BOSON RESONANCES

We present the general helicity formalism that enables one to calculate the angular distributions for boson resonances with sequential decay modes. The maximum complexity case to be considered will be the case of a boson resonance decaying to two intermediate bosons of arbitrary spin, both of which decay to three pseudoscalars. This can also be applied to resonances when the intermediate bosons decay into two pseudoscalars, or one of the intermediate bosons is a pseudoscalar meson [A.1].

Consider a reaction which produces a boson resonance B with spin J and parity η. That is consider the reaction,

$$a + b \rightarrow B(J^{\eta}) + c$$

The resonance B then decays to six pseudoscalar mesons via two intermediate bosons B_1 and B_2, with spins S_1 and S_2, and parities η_1 and η_2 respectively. That is

$$B(J^{\eta}) \rightarrow B_1(S_1^{\eta_1}) + B_2(S_2^{\eta_2})$$
$$\qquad\qquad \rightarrow a_3 + a_4 + a_5 \qquad \rightarrow a_6 + a_7 + a_8$$

where the a's are the pseudoscalar mesons. The cross section for this chain of reactions is given by,

$$d\sigma \sim \frac{1}{P_i E_T} \sum_{\substack{\text{spins}\\ a,b,c}} |A|^2 \left(\frac{P_f}{E_T} d\cos\theta_0 \right) \left(q\, dM_B\, d\Omega \right) \times$$
$$\left(\frac{dM_1}{M_1} d\Omega_1\, d\gamma_1\, dM_{34}^2\, dM_{45}^2 \right) \times \left(\frac{dM_2}{M_2} d\Omega_2\, d\gamma_2\, dM_{67}^2\, dM_{78}^2 \right)$$

where E_T is the total center of mass energy of a + b, and $P_i(P_f)$ is the center of mass momentum of a or b (B or c). θ_0 is the angle between B and a, in the center of mass system. M_B, M_1, M_2, M_{K4} are the effective masses of $B_1 + B_2$,

$a_3 + a_4 + a_5$, $a_6 + a_7 + a_8$, and $a_k + a_4$ systems respectively. q and $\Omega(\theta,\phi)$ are the magnitude and direction of the B_1 momentum in the rest frame of B, where we choose the z axis parallel to the direction of B, in the B rest frame. ϕ_1, θ_1, and γ_1 are the Euler angles for the configuration of a_3, a_4, and a_5 in the B_1 rest frame (rest frame with $\Omega(\theta_1,\phi_1)$ describing the normal to the decay plane). Again the coordinate system for angles Ω_1, (Ω_2) has the z axis parallel to the direction of B_1, (B_2) in the rest frame of B. (see Fig. A.1). The Lorentz invariant amplitude A is given by,

$$A \sim \sum_{\Lambda,\lambda_1,\lambda_2} \langle M_{34}^2, M_{45}^2, \Omega_1, \gamma_1 \mid \Pi_1 \mid S_1\ \lambda_1 \rangle \times$$

$$\langle M_{67}^2, M_{78}^2, \Omega_2, \gamma_2 \mid \Pi_2 \mid S_2\ \lambda_2 \rangle \langle S_1, \lambda_1, S_2, \lambda_2, q, \Omega \mid \Pi \mid J\ \Lambda \rangle \times$$

$$\langle c, J\ \Lambda \mid T \mid a, b \rangle\ \tilde{\delta}\ (M_1,\Gamma_1)\ \tilde{\delta}\ (M_2,\Gamma_2)\ \tilde{\delta}\ (M_B,\Gamma_B)$$

The first, second, and third factors are the decay amplitudes for B_1, B_2, and B respectively while the fourth factor is the transition amplitude for the first reaction. Λ, λ_1, λ_2 are the helicities of B, B_1, B_2. Also

$$\tilde{\delta}\ (M_B,\Gamma_B) = \frac{1}{M_B^2 - \left(M_B^0 - i\,\frac{\Gamma_B}{2} \right)^2}$$ is the Breit-Wigner form,

M_B^0, Γ_B being the mass and width of resonance B. The decay amplitudes are [A.2]

$$\langle S_1, \lambda_1, S_2, \lambda_2, q, \Omega \mid \Pi \mid J\ \Lambda \rangle = F^J_{\lambda_1,\lambda_2}(M_B,M_1,M_2)\ D^{J*}_{\Lambda,\lambda_1-\lambda_2}(\phi, \theta, 0)$$

$$\langle M_{34}^2, M_{45}^2, \Omega_1, \gamma_1 \mid \Pi_1 \mid S_1\ \lambda_1 \rangle = \sum_\mu F^1_\mu\ (M_1,M_{34}^2,M_{45}^2)\ D^{S1*}_{\lambda_1,\mu}\ (\phi_1, \theta_1, \gamma_1)$$

$$\langle M_{67}^2, M_{78}^2, \Omega_2, \gamma_2 \mid \Pi_2 \mid S_2\ \lambda_2 \rangle = \sum_\nu F^1_\nu\ (M_2,M_{67}^2,M_{78}^2)\ D^{S2*}_{\lambda_2,\nu}\ (\phi_2, \theta_2, \gamma_2)$$

where the F's are helicity amplitudes of resonances B and the D's are functions of the (2J+1) representation of the rotation group [A.3].

If B_2 decays to two pseudoscalar mesons then the decay amplitude is given by,

$$\langle q_2, \Omega_2 \mid \Pi_2 \mid S_2\ \lambda_2 \rangle = F^2 (M_2) D^{S_2 *}_{\lambda_2,0} (\phi_2, \theta_2, 0)$$

where q and Ω are the magnitude and direction of the momentum of one of the pseudoscalars in the B_2 rest frame. Parity conservation in the decay process leads to the following relations,

$$F^J_{\lambda_1 \lambda_2} = \varepsilon F^J_{-\lambda_1 -\lambda_2}$$

$$F^1_{\mu_2} = \eta_1 (-)^{\mu+1} F^1_{\mu}$$

$$F^2_{\nu} = \eta_2 (-)^{\nu+1} F^1_{\nu}$$

$$F^2 = 0 \quad \text{if} \quad \eta_2 (-)^{S_2} = -1 \qquad \text{where} \quad \varepsilon = \eta\ \eta_1 \eta_2 (-)^{J-S_1-S_2}$$

We define now the density matrix to be:

$$\rho^J_{\Lambda\Lambda'}(M_B) \sim \int d\cos\theta_0 \sum_{\substack{\text{spins}\\ a,b,c}} \langle c,J\Lambda \mid T \mid a,b\rangle \langle a,b \mid T^\dagger \mid c,J\Lambda'\rangle$$

thus being a general function of M_B. The limits on cos Θ_0 for the integration is meant to correspond to the experimental cuts used in case of peripheral production of B. If we define now $\lambda \equiv \lambda_1 - \lambda_2$, $\lambda' \equiv \lambda'_1 - \lambda'_2$ the differential cross section can be written as:

$$\frac{d\sigma}{dM_B d\Omega\ d\Omega_1 d\Omega_2} \sim \rho^J_{\Lambda\Lambda'} (M_B)\ g^{\mu\nu}_{\lambda_1\lambda_2\lambda'_1\lambda'_2} \times D^{J*}_{\Lambda\lambda} (\phi,\theta,0)\ D^J_{\Lambda'\lambda'}(\phi,\theta,0) \times$$

$$D^{S_1 *}_{\lambda_1\mu} (\phi_1,\theta_1,0)\ D^{S_1}_{\lambda'_1\mu} (\phi_1,\theta_1,0)\ D^{S_2 *}_{\lambda_2\nu} (\phi_2,\theta_2,0)\ D^{S_2}_{\lambda'_2\nu} (\phi_2,\theta_2,0)$$

Summation is implied over repeated indices, and we have integrated over $d\gamma_1 d\gamma_2$ introducing the parameter g depending on the helicity amplitudes in the following way,

$$g^{\mu\nu}_{\lambda_1\lambda_2\lambda_1'\lambda_2'}(M_B) = \int dM_1 dM_2\ K(M_B,M_1,M_2)\ F^J_{\lambda_1\lambda_2} \times F^{J*}_{\lambda_1'\lambda_2'} \int dM^2_{34} dM^2_{45} |F^1_\mu|^2 \times \int dM^2_{67} dM^2_{78} |\ F^2_\nu\ |^2$$

where $K(M_B,M_1,M_2) = \frac{1}{E_T^2}\ (\frac{P_f}{P_i})\ (\frac{q}{M_1\ M_2})\ \left|\ \tilde{\delta}(M_B,\Gamma_B)\ \tilde{\delta}(M_1,\Gamma_1)\ \tilde{\delta}(M_2,\Gamma_2)\right|^2$

The following properties for g follow,

$$g^{\mu\nu}_{\lambda_1\lambda_2\lambda_1'\lambda_2'} = \varepsilon\ g^{\mu\nu}_{-\lambda_1-\lambda_2\lambda_1'\lambda_2'} = \varepsilon\ g^{\mu\nu}_{\lambda_1\lambda_2-\lambda_1'-\lambda_2'} = g^{\mu\nu}_{-\lambda_1-\lambda_2-\lambda_1'-\lambda_2'}$$

$$g^{\mu\nu} = \eta_1 (-)^{\mu+1}\ g^{\mu\nu} = \eta_2\ (-)^{\nu+1}\ g^{\mu\nu}$$

$$g^{\mu\nu}_{\lambda_1\lambda_2\lambda_1'\lambda_2'} = g^{\mu\nu *}_{\lambda_1\lambda_2\lambda_1'\lambda_2'}$$

We define now the angular distribution for a given effective mass M_B to be

$$I(M_B,\ \Omega\ ,\ \Omega_1,\ \Omega_2)\ \sim\ \frac{d\sigma}{dM_B d\Omega\ d\Omega_1 d\Omega_2}$$ normalized to 1 as

$$\int\ dM_B d\Omega\ d\Omega_1 d\Omega_2\ I(M_B,\ \Omega,\ \Omega_1,\ \Omega_2)\ = 1$$

From the properties of the D functions (see section A.2) the normalized angular distributions can be written as,

$$I(M_B,\ \Omega\ ,\ \Omega_1,\ \Omega_2)\ = (\frac{2J+1}{4\pi})\ \frac{(2S_1+1)}{4\pi}\ \frac{(2S_2+1)}{4\pi}\ \times$$

$$\rho^J_{\Lambda\Lambda'}\ (M_B)\ g^{\mu\nu}_{\lambda_1\lambda_2\lambda_1'\lambda_2'} \times D^{J*}_{\Lambda\lambda}\ (\phi,\theta,0)\ D^J_{\Lambda'\lambda'}(\phi,\theta,0)\ \times$$

$$D^{S_1*}_{\lambda_1\mu}\ (\phi_1,\theta_1,0)\ D^{S_1}_{\lambda_1'\mu}\ (\phi_1,\theta_1,0)\ D^{S_2*}_{\lambda_2\nu}\ (\phi_2,\theta_2,0)\ D^{S_2}_{\lambda_2'\nu}\ (\phi_2,\theta_2,0)$$

where we require

$$\int dM_B\ \sum_\Lambda\ \rho^J_{\Lambda\Lambda}\ (M_B)\ \sum_{\mu\nu\lambda_1\lambda_2}\ g^{\mu\nu}_{\lambda_1\lambda_2\lambda_1\lambda_2}\ (M_B)\ = 1$$ assuming no interference

between the decay products of B_1 and B_2 .

As an example of a simpler decay mode of B consider the reaction,

$$B(J^{\eta}) \rightarrow B_1(S^{\mu 1}) + B_2(0^-)$$
$$\quad\quad\quad\quad\quad\quad \hookrightarrow a_3 + a_4 \quad \text{(two pseudoscalars)}$$

The angular distribution then simplifies to

$$I(M_B, \Omega, \Omega_1) = \frac{(2J+1)}{4\pi} \frac{(2S+1)}{4\pi} \rho^J_{\Lambda\Lambda'}(M_B)\, g_{\lambda\lambda'}(M_B) \times$$
$$D^{J*}_{\Lambda\lambda}(\phi,\theta,0)\, D^J_{\Lambda'\lambda'}(\phi,\theta,0)\, D^{S*}_{\lambda 0}(\phi_1,\theta_1,0)\, D^S_{\lambda' 0}(\phi_1,\theta_1,0)$$

For the specific reaction like $D \rightarrow \phi\pi$ where we have ,

$$0^- \rightarrow 1^- + 0^-$$
$$\quad\quad\quad \hookrightarrow 0^- + 0^-$$

$$I(M_B, \Omega, \Omega_1) = \frac{3}{(4\pi)^2} \rho^0_{00}(M_B)\, g_{00}(M_B) \times$$
$$D^{0*}_{00}(\phi,\theta,0)\, D^0_{00}(\phi,\theta,0)\, D^{1*}_{00}(\phi_1,\theta_1,0)\, D^1_{00}(\phi_1,\theta_1,0)$$

and the normalized angular distribution will be proportional to $\cos^2\theta_1$

A.2 Properties of the D and d functions.

The D functions used here are the same as the ones used in Rose [A.3] that is,

$D^J_{\mu m}(\alpha,\beta,\gamma) = e^{-i\mu\alpha}\, d^J_{\mu m}(\beta)\, e^{-im\gamma}$. The integrals involving D functions are $\int d\Omega\, D^{J_1*}_{\mu_1 m}(\Omega)\, D^{J_2}_{\mu_2 m}(\Omega) = \frac{4\pi}{2J_1+1}\, \delta_{\mu_1\mu_2}\delta_{J_1J_2}$.

The d functions have the following properties,

$$d^J_{m'm}(\beta) = (-1)^{m-m'}\, d^J_{-m',-m}(\beta)$$
$$d^J_{m'm}(\beta) = (-1)^{m-m'}\, d^J_{m\,m'}(\beta)$$

A list of the d functions up to spin 1 can be found on the next page. For a more complete list see Ref. A.2.

Spin $\frac{1}{2}$: $d_{\frac{1}{2}\frac{1}{2}} = \cos\frac{1}{2}\beta$, $d_{-\frac{1}{2}\frac{1}{2}} = \sin\frac{1}{2}\beta$

Spin 1 : $d_{11}(\beta) = \frac{1}{2}(1 + \cos\beta)$ $d_{01}(\beta) = (\sin\beta)/\sqrt{2}$

$d_{1-1}(\beta) = \frac{1}{2}(1 - \cos\beta)$ $d_{00}(\beta) = \cos\beta$

REFERENCES

[A.1] Chung S. U., Phys. Rev. 169,5(1968)1342.

[A.2] Berman S. M., and M. Jacob, Phys. Rev. 169(1965)1023.

[A.3] Rose M. E., Elementary Theory of Angular Momentum (J. Wiley & Sons Inc., New York, 1957).

FIGURE CAPTIONS

A.1 Helicity angle definition for resonances with sequential decay modes.

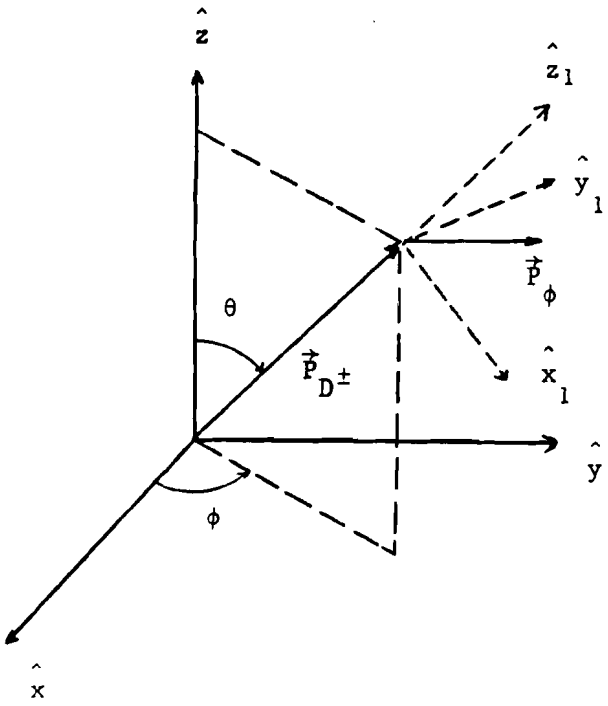

$pp \to D^\pm + X$

$\to \phi + \pi^\pm$

$\to K^+ + K^-$

$\hat{y} = \hat{z} \times \hat{x}$ (normal to the producti plane)

$\hat{z}$ is the beam direction

$\hat{x}$ is the direction of particle X

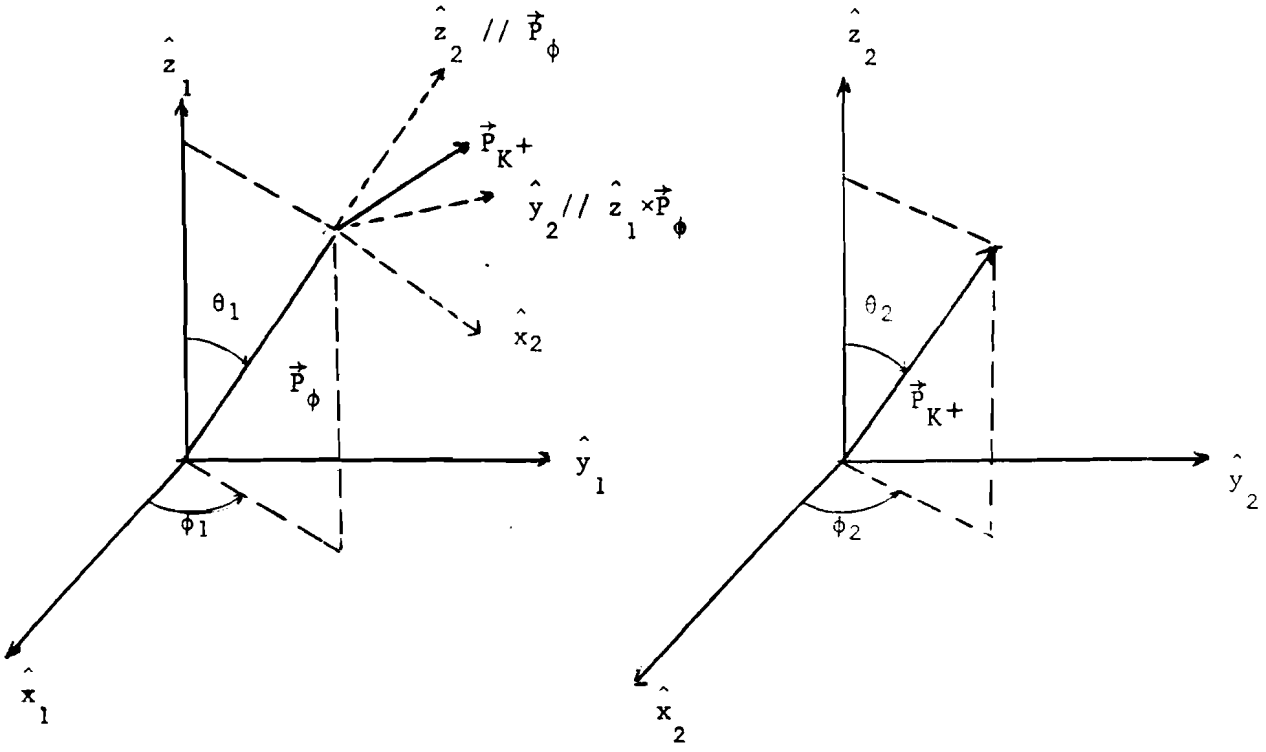

Fig. A.1

APPENDIX B

MONTE CARLO DEVELOPMENT FOR E-623

We developed a Fortran-77 program to propagate pregenerated events for the Fermilab MPS experiment E-623. The pregenerated events can come from any program that will feed in the appropriate 4-vectors. There are two versions of this program, one for a VAX-11 system and one for the CDC system at FERMILAB.

The following are intrinsic to the setup of E-623:

1) Simulation of the E-623 trigger processor.
2) Inversion of the particle identification algorithm for the two Cherenkov counters to provide realistic pulse height distributions.
3) Drift chambers are treated by inverting the 3rd order polynomial fit for the real data, using a Newton-Raphson method to calculate drift times from distances.
4) The problem of multiple Coulomb scattering due to the presence of thick material in the apparatus is treated in a realistic way.
5) The full grid map of the MPS magnet is used to propagate the particles and, although a little slower, it is much more realistic than using any polynomial approximation for the field.

A brief description of the above follows:

1) The trigger processor is simulated as closely as possible (see chapter 3).
2) For the two Cherenkov counters, a program written for the real data was modified to simulate the behavior as realistically as possible. CA and CB mirrors are treated differently. The fact that CA is inside the magnet is taken into account by approximating the shape of the illuminated area of the

mirrors by an ellipse. The response of the Cherenkov counters is simulated by smearing the average number of photoelectrons expected from a particle of a certain momentum with a Poisson distribution. Then the pulse height is calculated by multiplying this number with the one-photoelectron peak value determined from the real data and finally adding the pedestal value. A more complete description of the method can be found in Chapter 4.

3) For the distance-to-time conversion for the drift chambers, a Newton -Raphson method was employed. This choice instead of the exact solution of the cubic equation was preferred, the reason being the occasional difficulty in determining which of the real solutions was the physical one. The program can operate in both modes, that is calculate the drift times from a cubic or a linear fit according to the value of a logical variable. The convergence criterion was based on the value of the function and a convergence to accuracy less than .1 nsec is achieved in less than 6 iterations. For each wire individual t_0's are used and the physical time is between 0 and 215 nsec. If the particle passes a distance closer than 0.075 mm to the wire a t_0 value is assigned for the drift time for that wire.

4) The problem of multiple scattering was treated in the following way. The major effect comes from the glass mirrors of the two Cherenkov counters, the smart target scintillator and the scintillator wall. The gas contents of these counters play a small but significant role. To be more accurate the effect due to the windows of the PWC's and the drift chambers as well as their gas content is included. As a charged particle traverses a medium it is deflected by many small angle elastic scatterings. The bulk of the deflection is due to elastic Coulomb scattering from the nuclei within the medium. If Θ_{pl} is the angle the scattered vector makes with the original it can be approximated by a Gaussian distribution,

$$g(\Theta_{pl})\, d\Theta_{pl} = \frac{1}{\Theta_0\sqrt{\pi}} \exp\left(-\frac{\Theta^2_{pl}}{\Theta^2_0}\right) d\Theta_{pl}$$

where

$$\Theta_0 = \frac{0.02\ \text{Gev/c}}{p\ \beta} Z_{inc} \sqrt{\frac{L}{L_R}} \left[1 + \frac{1}{9} \log\left(\frac{L}{L_R}\right) \right] \quad \text{(radians)}$$

p, β, Z_{inc} being the momentum, velocity and charge number of the incident particle and L/L_R is the thickness of the scattering medium in radiation lengths. Since the scattered vector is azimuthally invariant about the original one, an angle ϕ was generated from a uniform distribution between 0 and 2π, defined on a plane perpendicular to the original momentum vector. Θ_{pl} is generated from a Gaussian where the 1σ level is chosen to be $\Theta_0 / \sqrt{2}$. If α and β are the two polar angles of the original vector and S_x, S_y are the x,y slopes respectively then

$$\alpha = \tan^{-1}\left[\frac{1}{S_y(\sin\beta)}\right], \qquad \beta = \cot^{-1}(S_x)$$

and the angles of the new vector, α' and β' are given by $\alpha' = \alpha - \varepsilon_1$ and $\beta' = \beta + \varepsilon_2$ where $\tan(\varepsilon_2) = \tan(\Theta_{pl})\cos(\phi)$ and $\tan(\varepsilon_2) = \tan(\Theta_{pl})\sin(\phi)$. Since Θ_{pl} is on the average less than one milliradian we can safely approximate $\tan(\Theta_{pl})$ with Θ_{pl}. So $\varepsilon_1 = \Theta_{pl}\cos\phi$, $\varepsilon_2 = \Theta_{pl}\sin\phi$. Thus:

$$\alpha' = \alpha - \Theta_{pl}\cos\phi \qquad \beta' = \beta - \Theta_{pl}\sin\phi$$

and

$$S'_x = \frac{1}{\tan\beta'} \qquad S'_y = \frac{1}{\tan\alpha'\ \tan\beta'}$$

will be the slopes of the new vector.